

**Novel carbon-based fibers with
exceptional thermal and mechanical
properties from polymer precursors**

DISSERTATION

zur Erlangung des akademischen Grades

Doktor der Naturwissenschaften (Dr. rer. nat.)

in der Bayreuther Graduiertenschule für Mathematik

und Naturwissenschaften (BayNAT)

der Universität Bayreuth

vorgelegt von

Jakob Benedikt Denk

geboren in Freyung

Bayreuth, 2024

This doctoral thesis was prepared at the department of Ceramic Materials Engineering at the University of Bayreuth from 02/2020 until 04/2024 and was supervised by Prof. Dr. Günter Motz.

This is a full reprint of the thesis submitted to obtain the academic degree of Doctor of Natural Sciences (Dr. rer. nat.) and approved by the Bayreuth Graduate School of Mathematical and Natural Sciences (BayNAT) of the University of Bayreuth.

Form of the dissertation: cumulative thesis

Date of submission: 15.10.2024

Admission by the executive board: 13.11.2024

Date of defence: 22.05.2025

Acting director: Prof. Dr. Jürgen Köhler

Doctoral committee:

Prof. Dr. Günter Motz (reviewer)

Prof. Dr. Andreas Greiner (reviewer)

Prof. Dr. Rhett Kempe (chair)

Prof. Dr. Christina Roth

Parts of the work have already been published as follows:

(1) X. Liao, J. Denk, T. Tran, N. Miyajima, L. Benker, S. Rosenfeldt, S. Schafföner, M. Retsch, A. Greiner, G. Motz, S. Agarwal, *Sci. Adv.* **2023**, *9*.

(2) J. Denk, X. Liao, W. Knolle, A. Kahnt, A. Greiner, S. Schafföner, S. Agarwal, G. Motz, *Sci. Rep.* **2024**, *14*, 18143.

(3) J. Denk, X. Liao, M. Dulle, S. Schafföner, S. Förster, A. Greiner, G. Motz, S. Agarwal, *Mater. Horiz.* **2024**, *11*, 5777-5785.

Wer nichts weiß, muss alles glauben.

Marie v. Ebner-Eschenbach

TABLE OF CONTENTS

TABLE OF CONTENTS	I
LIST OF SYMBOLS AND ABBREVIATIONS	1
SUMMARY	3
ZUSAMMENFASSUNG	5
1 INTRODUCTION	8
2 STATE OF THE ART	11
2.1 Polymer derived ceramics	11
2.2 Ceramic Fibers.....	13
2.2.1 Carbon Fibers	13
2.2.2 Ceramic SiC Fibers	15
2.2.3 Ceramic SiCN Fibers.....	16
2.2.4 Ceramic oxide Fibers.....	17
2.3 Processing of Ceramic Fibers	18
2.3.1 CVD Process	18
2.3.2 Melt-Spinning.....	18
2.3.3 Dry- and wet-spinning.....	19
2.3.4 Electrospinning.....	21
REFERENCES	25
3 SYNOPSIS	31
3.1 Extremely low thermal conductivity and high electrical conductivity of sustainable carbon-ceramic electrospun nonwoven materials.....	32
3.2 Novel multifibrillar carbon and oxidation-stable carbon/ceramic hybrid fibers consisting of thousands of individual nanofibers with high tensile strength.....	34
3.3 Synergistic enhancement of thermomechanical properties and oxidation resistance in aligned co-continuous carbon-ceramic hybrid fibers	36
4 CONTRIBUTION TO THE PUBLICATIONS	38
4.1 Extremely low thermal conductivity and high electrical conductivity of sustainable carbon-ceramic electrospun nonwoven materials.....	38
4.2 Novel multifibrillar carbon and oxidation stable carbon/ceramic hybrid fibers consisting of thousands of individual nanofibers with high tensile strength.....	38
4.3 Synergistic enhancement of thermomechanical properties and oxidation resistance in aligned co-continuous carbon-ceramic hybrid fibers	39

5	PUBLICATIONS	40
5.1	Extremely low thermal conductivity and high electrical conductivity of sustainable carbon/ceramic electrospun nonwoven materials	40
5.2	Novel multifibrillar carbon and oxidation-stable carbon/ceramic hybrid fibers consisting of thousands of individual nanofibers with high tensile strength.....	86
5.3	Synergistic enhancement of thermomechanical properties and oxidation resistance in aligned co-continuous carbon-ceramic hybrid fibers	112
6	ACKNOWLEDGEMENTS.....	151
7	(EIDESSTATTLICHE) VERSICHERUNGEN UND ERKLÄRUNGEN	152

LIST OF SYMBOLS AND ABBREVIATIONS

μ	Mikro
A	Ampere
°C	Degree celsius
C/SiCON	Carbon/Silicon carbide oxide nitride
CA	Cellulose acetate
CMC	Ceramic matrix composite
CVD	Chemical vapor deposition
DCP	Dicumyl peroxide
DMAc	Dimethyl acetamide
DMF	<i>N,N</i> -Dimethyl formamide
DMSO	Dimethyl sulfoxide
Fig	Figure
g	Gram
G	Giga
h	Hour
k	Kilo
K	Kelvin
M	Mega
min	minute
MMC	Metal matrix composites
n	Nano
OSZ	Oligosilazane
Pa	Pascal

PA	Polyamide
PAN	Polyacrylonitrile
PC	Polycarbonate
PDC	Polymer derived ceramics
PEO	Polyethylenoxide
PET	Polyethyleneterephthalate
PI	Polyimides
PMMA	Poly(methyl methacrylate)
PS	Polystyrene
PU	Polyurethanes
PVA	Polyvinylalcohol
PVC	Polyvinylchloride
s	Second
S	Siemens
SEM	Scanning electron microscope
SiC	Silicon carbide
SiCN	Silicon carbide nitride
T	Temperature
TBAF	Tetra- <i>n</i> -butylammonium fluoride
TEM	Transmission electron microscopy
TGA	Thermogravimetric analysis
THF	Tetrahydrofuran
V	Voltage
W	Watt
WAXS	Wide-angle X-ray scattering

SUMMARY

The outstanding properties of carbon fibers, such as high tensile strength of up to 7 GPa and a Young's modulus of up to 600 MPa, together with a low density of 1.8 to 2.0 g cm⁻³, made them indispensable in high-tech products in the aerospace, transport, military and sports sectors. However, carbon fibers have the disadvantage of oxidizing in air above 400 °C, which severely limits their applications. Although it is possible to increase the oxidation stability by coatings, this is complex and expensive, and a small defect in the coating results again in the oxidation of the fibers. Therefore, it is much more promising to increase the oxidation stability intrinsically by modifying the organic polymer. Preliminary investigations have shown that one approach could be the addition of oligosilazanes (OSZ) to the precursor polyacrylonitrile (PAN).

Another limitation of carbon fibers is their tensile strength. Although the tensile strength of commercial fibers is very high, with values of up to 7 GPa, theoretically values of up to 180 GPa would be possible. The reason for the significantly lower tensile strength are defects in the fibers. With brittle fibers, a single defect is usually sufficient to cause catastrophic failure and breakage. However, according to the Griffith principle, the tensile strength increases exponentially as the diameter decreases. The reason is that the probability of a defect per unit length decreases with the fiber diameter.

A promising spinning technique to achieve small fiber diameters is electrospinning. In an advanced electrospinning process, continuous multifibrillar fibers consisting of thousands of nanofibers have recently been processed from PAN. This technique could be suitable for processing carbon fibers with unprecedented tensile strengths.

The aim of this work was to significantly increase the oxidation stability of carbon fibers using polymer blends or copolymers with OSZ. Therefore, the corresponding polymer solutions and spinning processes had to be developed and optimized in order to obtain continuous fibers and to characterize their properties. This work resulted in three publications, which are summarized in this thesis.

In the first publication, PAN and the corresponding blends with OSZ were electrospun into polymer nonwovens. Extremely flexible and foldable C/SiCON ceramic nonwovens with high oxidation stability and unique electrothermal properties were obtained. The nonwovens exhibited a very high electrical conductivity between 4.2 and 20.1 S cm⁻¹ and a low thermal

conductivity, which decreased to $10 \text{ mW m}^{-1} \text{ K}^{-1}$ with higher OSZ composition. A comprehensive chemical and structural analysis of the material revealed the reason for these unique properties: The "sea-island" nanostructure. The carbon phase is the "sea" responsible for the high electrical conductivity, and the ceramic phases distributed as "islands" lead to the low thermal conductivities due to phonon scattering at the interfaces with the carbon phase.

In the second article, the polymer blends were electrospun into continuous multifibrillar fibers. After optimization of the stabilization and pyrolysis programs, these could be processed into continuous C/SiCON ceramic fibers with lengths of several meters. However, during the stabilization process at $250 \text{ }^\circ\text{C}$ in air, the individual nanofibers softened and stuck together, which severely limits the tensile strength. Various approaches were taken to prevent melting. The most successful treatment was electron beam irradiation. Crosslinking in the polymer state significantly reduced the sticking during the stabilization step and increased the tensile strength from 407 MPa to 707 MPa . The approach of multifibrillar fiber spinning remains very promising due to the nanometer scale, the low weight of the fibers and the possibility of continuous production. Significantly improved mechanical properties can be expected in the future through further development of this approach.

In the third publication, continuous C/SiCON hybrid fibers were produced from polymer blends of PAN and the OSZ Durazane 1800 using a wet-spinning process. Tensile strengths of 2.0 GPa were achieved with a fiber diameter of $20 \text{ }\mu\text{m}$. Considering the equipment used and the still relatively large diameters, these are excellent values, comparable with commercial ceramic fibers. However, the decisive factor is that the oxidation stability of the fibers has been significantly improved. Thermogravimetric analysis (TGA) showed a significant delay of the oxidation in air. Additionally, when fiber bundles were treated under load with a flame at $1200 \text{ }^\circ\text{C}$, they withstood the flame for over 150 s without breaking, in contrast to carbon fibers, which only last for 4 s .

ZUSAMMENFASSUNG

Eine der bedeutendsten technischen Fasern sind Kohlenstofffasern. Aufgrund ihrer herausragenden Eigenschaften, wie beispielsweise Zugfestigkeiten von bis zu 7 GPa und Elastizitätsmoduln von bis zu 600 MPa und der gleichzeitig geringen Dichte von 1,8 bis 2,0 g cm⁻³ sind Kohlenstofffasern aus Hightechprodukten der Luft- und Raumfahrt, Verkehr, Militär und Sport nicht mehr wegzudenken. Allerdings haben Kohlenstofffasern den Nachteil, dass sie ab 400 °C an Luft oxidieren, was die Einsatzmöglichkeiten stark einschränkt. Es gibt zwar die Möglichkeit die Oxidationsstabilität mittels Beschichtungen zu erhöhen, jedoch ist solch eine Modifizierung aufwendig und teuer, außerdem reicht ein kleiner Defekt in der Beschichtung aus, um die Faser wieder angreifbar für die Oxidation durch Sauerstoff zu machen. Deutlich vielversprechender wäre es deshalb, die Oxidationsstabilität intrinsisch durch eine Modifikation des Ausgangspolymers zu erhöhen. Wie Voruntersuchungen zeigten, könnte ein solcher Ansatz das Hinzufügen von Oligosilazanen (OSZ) zum Precursor Polyacrylnitril (PAN) sein.

Eine weitere Limitierung von Kohlenstofffasern sind deren Zugfestigkeiten. Zwar sind diese mit Werten von bis zu 7 GPa bei kommerziellen Fasern grundsätzlich sehr hoch, jedoch wären theoretisch bis zu 180 GPa möglich. Der Grund für die deutlich niedrigeren Zugfestigkeiten liegt im Auftreten von Defekten in den Fasern. Bei spröden Fasern, reicht in der Regel bereits ein Defekt aus um zu einem katastrophalen Versagen und dem Bruch zu führen. Nach dem Griffith Prinzip nimmt mit kleinerem Faserdurchmesser die Wahrscheinlichkeit für einen Defekt pro Längeneinheit jedoch ab, weshalb die Zugfestigkeiten mit kleinerem Durchmesser exponentiell steigen. Eine vielversprechende Möglichkeit zu deutlich kleineren Faserdurchmessern im Nanometerbereich zu kommen, liefert das Elektrospinnen. In einem weiterentwickelten Elektrospinnprozess wurden kürzlich aus PAN kontinuierliche multifibrilläre Fasern bestehend aus tausenden Nanofasern elektrogenesponnen. Diese könnten grundsätzlich für die Weiterverarbeitung zu Kohlenstofffasern geeignet sein, um bisher unerreichbare Zugfestigkeiten zu erhalten.

Ziel dieser Arbeit war es deshalb die Oxidationsstabilität von Kohlenstofffasern durch Polymerblends oder Copolymere mit OSZ signifikant zu erhöhen. Hierfür sollten die entsprechenden Polymerlösungen bzw. die Spinnprozesse entwickelt und optimiert werden, sodass kontinuierliche Fasern erhalten und deren Eigenschaften charakterisiert werden können.

Im Rahmen dieser Arbeiten entstanden dabei drei Publikationen, die in dieser Dissertation zusammengefasst sind.

In der ersten Veröffentlichung wurde PAN und die entsprechenden Blends mit den OSZ zu Polymervliesen elektrogewoben. Es wurden extrem flexible und faltbare C/SiCON Keramikvliese erhalten. Neben der auch hier deutlich zu beobachtenden Oxidationsstabilität der Hybridfasern, wurden einzigartige elektrothermische Eigenschaften des Materials ermittelt. So besaßen die Faservliese eine sehr hohe elektrische Leitfähigkeit zwischen 4.2 und 20.1 S cm⁻¹ und gleichzeitig eine niedrige thermische Leitfähigkeit, die mit Zunahme an OSZ auf bis zu 10 mW m⁻¹ K⁻¹ abnahm. Solche Eigenschaften konnten bisher von keinem anderen Werkstoff erhalten werden. Eine umfassende chemische und strukturelle Analyse des Materials offenbarte den Grund für diese einzigartigen Eigenschaften: Diese liegt in der „See-Insel“-Nanostruktur begründet. Die Kohlenstoffphase ist dabei die „See“, die für die hohe elektrische Leitfähigkeit zuständig ist und die Keramikphasen die als „Inseln“ verteilt sind, führt durch die Streuung der Phononen an den Grenzflächen mit der Kohlenstoffphase zu den niedrigen thermischen Leitfähigkeiten.

In der zweiten Arbeit wurden die Polymerblends zu kontinuierlichen multifibrillären Fasern elektrogewoben. Nach Optimierung der Stabilisierungs- und Pyrolyseprogramme konnten diese zu kontinuierlichen C/SiCON Keramikfasern mit Längen von mehreren Metern weiterverarbeitet werden. Es wurde jedoch beobachtet, dass beim Stabilisierungsprozess bei 250 °C an Luft die einzelnen Nanofasern erweichen und zusammenkleben, weshalb die Zugfestigkeiten stark limitiert sind. Um ein Aufschmelzen zu verhindern, wurden verschiedene Ansätze gewählt. Am erfolgreichsten war dabei die Behandlung der C/SiCON multifibrillären Fasern mittels Elektronenbestrahlung. Durch die Vernetzung im polymeren Zustand konnte ein Zusammenkleben während des Stabilisierungsschritts deutlich verringert werden und die Zugfestigkeiten von 407 MPa auf 707 MPa erhöht werden. Da ein Zusammenkleben der Nanofasern jedoch nicht komplett verhindert wird, es prozessbedingt zu Verschlaufungen der Nanofasern kommt und Faserbündel niedrigere Zugfestigkeiten als Einzelfasern haben, können die theoretisch möglichen Zugfestigkeiten von 180 GPa noch nicht erreicht werden. Der Ansatz der multifibrillären Fasern bleibt jedoch aufgrund Faserdurchmesser im Nanometerbereich, des geringen Eigengewichts der Fasern und der Möglichkeit zur kontinuierlichen Herstellung sehr vielversprechend, weshalb durch Weiterentwicklung dieses Ansatzes zukünftig deutlich bessere mechanische Eigenschaften zu erwarten sind.

In der dritten Publikation, wurden über einen Nassspinnprozess kontinuierliche C/SiCON Hybridfasern aus Polymerblends aus PAN und dem OSZ Durazane 1800 hergestellt. Dabei wurden Zugfestigkeiten von 2.0 GPa bei einem Faserdurchmesser von 20 μm erhalten. Berücksichtigt man das verwendete Equipment und die noch relativ großen Durchmesser, handelt es sich dabei um hervorragende Werte die auch mit kommerziellen Keramikfasern vergleichbar sind. Entscheidend ist jedoch, dass die Oxidationsstabilität der Fasern deutlich erhöht werden konnte. Messungen in der Thermogravimetrischen Analyse (TGA) zeigten eine signifikante Verzögerung der Oxidation an Luft, sodass beispielsweise ein Masseverlust von 20 % bei Fasern mit 40 wt.% Silazananteil um 260 °C auf 833 °C verschoben werden konnte. Wurden Faserbündel unter Belastung mittels einer Flamme bei 1200 °C behandelt, hielten diese im Gegensatz zu Kohlenstofffasern (4 s) über 150 s lang der Flamme stand, ohne zu reißen.

1 INTRODUCTION

For a long time, the idea of a space elevator, in which people and equipment can simply travel into space via a gondola, has existed in science fiction literature. One of the first books in which this idea was mentioned is "The Fountains of Paradise" by Arthur C. Clarke published in 1979.^[1] Another example is the novel "Limit" by Frank Schätzing, published in 2009,^[2] but also the American space agency NASA is discussing this concept on a more scientific background.^[3] The decisive advantages that such an elevator would have over conventional rockets is the immense reduction in transportation costs from several thousand euro to less than 10 € kg⁻¹ and would thus grant a much easier access to space. The main reason why such a device has not yet become a reality is that it would require extremely light, continuous fibers with enormous tensile strengths of more than 50 GPa to establish a connection between the earth and a geostationary satellite without rupturing.^[3,4]

One of the most used and interesting technical fibers are carbon fibers. The unique combination of a low density of only 1.75 to 2.00 g cm⁻³, combined with tensile strengths of up to 7 GPa and a modulus of 600 MPa have led to a widespread use of carbon fibers in a variety of fields, such as automotive sector, aerospace, wind turbines and military applications.^[5,6] The fact that this high-tech product is becoming increasingly important can also be seen in its steadily rising demand. In 2010, the usage was 33,000 tons, and has risen continuously in recent years to a predicted value of 143,500 tons for 2024.^[7] Despite their outstanding properties, commercial carbon fibers achieve only a fraction of their theoretically possible tensile strength of up to 180 GPa.^[8,9] The reason for this is that in brittle fibers usually only one defect is enough to lead to catastrophic failure and breakage. Therefore, the tensile strength decreases exponentially with larger fiber diameters, since the probability for a defect per unit length increases. This principle was already discovered by Griffith in 1921 for glass fibers^[10] and also confirmed for melt-spun SiCN fibers later.^[11] This is the reason why, commercial wet-spun carbon fibers are processed with small diameters of 5 to 7 μm.^[12] A highly interesting processing technique to produce smaller fibers is electrospinning, which is explained in detail in Chapter 2.3.4. In electrospinning, fiber diameters of 0.1 to 2 μm can be spun. After pyrolysis to carbon fibers this could result in significantly higher tensile strengths than commercial wet-spun fibers. Due to a novel developed electrospinning process, multifibrillar polymer fibers, which consist of thousands of fibers in the nanometer range aligned in one direction, can be processed.^[13,14] This technique has already been used to spin fibers from polyacrylonitrile (PAN), suitable for the

processing of carbon fibers and is therefore promising for producing novel carbon fibers with exceptionally high tensile strengths in a continuous way.

Another disadvantage of carbon fibers is the low oxidation stability, which is discussed in detail in Chapter 2.2.1. The decomposition of carbon begins already at 400 °C in air and therefore severely limits the usage of carbon fibers. If carbon fibers should be used for example in ceramic matrix composites (CMCs), the oxidation stability has to be improved. Until recently the only option was to apply glass-forming coatings to the fibers. However, this technique is not economical and as soon as a defect occurs in the coating, the fiber starts to oxidize again.^[15–21] For this reason an intrinsic approach is much more promising. Such an option was developed by Ribeiro *et al.* ^[22,23] who synthesized hybrid polymers of acrylonitrile and oligosilazanes (OSZ). After pyrolysis, homogeneously distributed Si₃N₄ nanocomposites, introduced by the OSZ, acted as an oxidative protective layer for the carbon. With this approach the oxidation resistance was significantly improved from 400 to over 1000 °C in air atmosphere. In this initial work, only short fiber pieces with thick diameters of 100 μm via dry spinning were produced. It is therefore necessary to develop and optimize the spinning processes for continuous fibers with diameters in the small micrometer or nanometer range in the future.

In order to turn the mentioned ideas from science fiction to reality and to be able to develop components and devices with previously unachievable properties, constant development and research is necessary. Therefore, the goal of this work is to develop novel continuous carbon and ceramic fibers prepared via the previously described technique for multifibrillar fiber electrospinning. As discussed before, it should be possible to achieve significantly higher tensile strengths by reducing the individual fiber diameters into the nanometer range. In addition, the use of polymer blends or copolymers of PAN and OSZ should increase the oxidation stability to enable the use of the hybrid fibers at higher temperatures, for example for applications in CMCs, or to increase the flame stability. For this challenging task, it is first necessary to optimize the electrospinning process and the thermal stabilization and pyrolysis. Afterwards, chemical and structural analysis of the obtained ceramic fibers have to be performed. Therefore, flat nonwovens have to be produced first via the standard electrospinning technique. This enables a more straightforward optimization of the electrospinning process and allows the production of larger fiber quantities for the analysis of the material properties.

Afterwards, the electrospinning of multifibrillar fibers will be carried out, and the entire process, from spinning to pyrolysis, should be optimized to achieve a continuous multifibrillar C/SiCON fiber. The main problem that might occur is a softening of the polymer and sticking

of the nanofibers, which would severely limit the tensile strength. For this reason, it may be necessary to prevent this by adding catalysts to reduce the crosslinking temperature or by precuring via electronbeam radiation.

In addition, the PAN/OSZ blends should be optimized for a more widespread spinning processes such as wet-spinning. This should lead to diameters in the lower micrometer range and comparable tensile strengths as commercial fibers but with a significantly higher oxidation stability. Since wet-spinning is already commercially used, it could be implemented on existing fiber spinning plants, which would facilitate the commercial production of these fibers.

In order to present the current state of the art, the production of carbon and ceramic fibers, their precursors and spinning techniques will be explained in more detail in the following chapters.

2 STATE OF THE ART

2.1 Polymer derived ceramics

Polymer derived ceramics (PDCs) offer a novel method for producing ceramics through the conversion of polymeric precursors by pyrolysis. The polymers usually used have an inorganic backbone based on silicon and other elements like O, C and N. Mainly polysiloxanes, polycarbosilanes, and polysilazanes, as well as hybrids of these, are used (Fig. 1).^[24,25] By the elemental composition of the polymer, the subsequent ceramic can be adjusted and modified as required. Accordingly, the obtained ceramic consists of SiOC, SiC or SiCN.

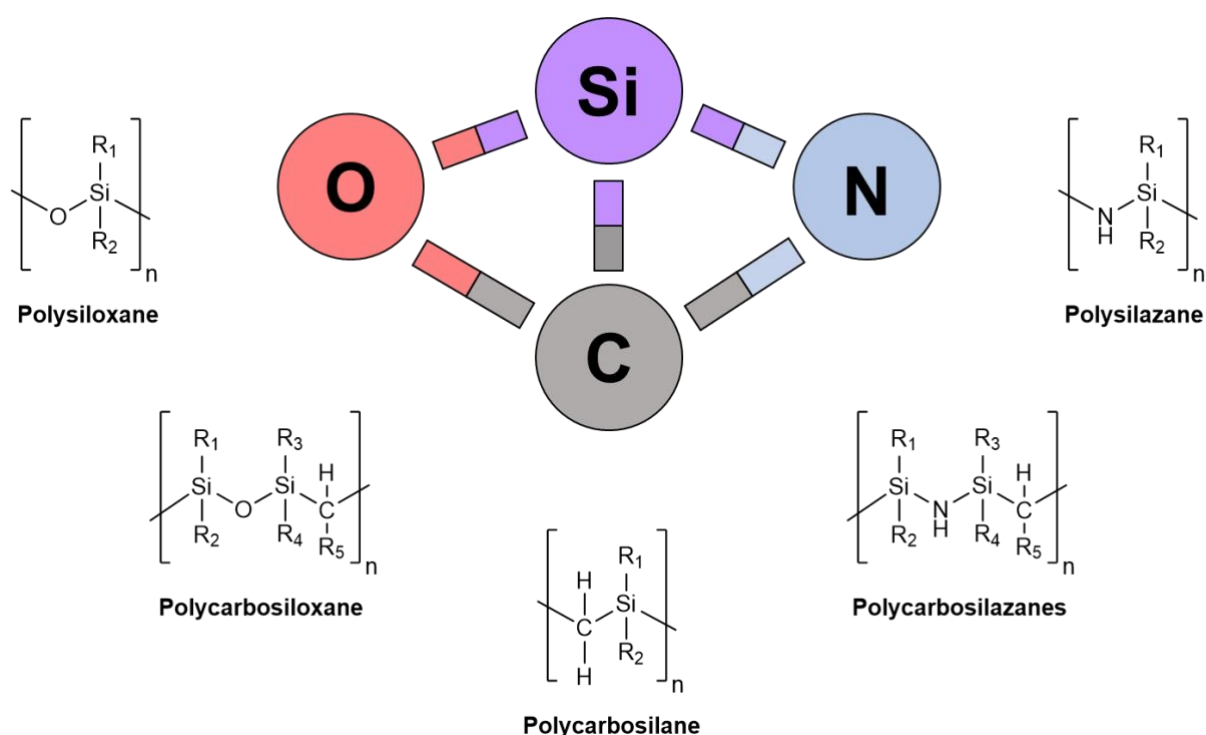


Fig. 1: Chemical structure of the most common preceramic polymers ($\text{R}_x = \text{H}$ or alkyl).^[24,26,27]

Other major advantages of PDCs are the relatively low pyrolysis temperatures of 1100 – 1300 °C and the high creep, oxidation, and crystallization temperatures of up to 1500 °C.^[24,28,29] To achieve a high ceramic yield the precursors have to be crosslinked before the pyrolysis. The easiest way to do this, is by thermal crosslinking at 100 – 400 °C.^[24,26] Depending on the side-groups, certain reactions can be used to lower the curing temperature. For example, vinyl groups can be crosslinked by radical initiated polymerization or Si-H and N-H groups can be linked by a selective catalytic reaction with tetra-*n*-butylammonium fluoride (TBAF), which delivers a meltable polymer.^[11,30,31] Other options enable crosslinking under inert gas by UV light^[32–35] or treatment with gamma respectively electron radiation.^[36–38]

In addition, blends or copolymers of PDCs with organic polymers can be made to produce organic/inorganic hybrid materials. Various examples of composites made from silicon-containing components and organic polymers can be found in the literature. One common application is fire protection as a halogen-free alternative.

For example, silanes^[39,40] or siloxanes^[41] were used as adhesion promoters to produce blends of organic polymers and inorganic fillers such as Mg(OH)₂ or organoclay to achieve halogen-free flame retardancy. However, effective flame retardancy is also possible without inorganic particles. Other approaches used blends of phosphorus-containing siloxanes and polymers such as polycarbonate.^[42,43]

In addition, UV-curable resins have been prepared from blends of phenyl silanes and an epoxy acrylate that could be applied to components as flame retardant coatings in future.^[44]

Chiang *et al.* developed epoxy nanocomposites containing silicon, nitrogen, and phosphorus with the sol-gel route.^[45] This resulted in significantly improved thermal stability and fire resistance compared to pure epoxy resin. In addition, significantly fewer toxic gases are released in the case of fire. Other approaches added polysilsesquioxanes and polycarbosilanes as flame retardants to thermoplastic polymers such as polypropylene.^[46-48] When exposed to flames, the preceramic polymers form an insulating layer on the surface that shields the organic polymer. Similar approaches can be found for copolymers of polycarbonate and methylphenyl silicones.^[49]

Besides their applications in flame retardants, the mechanical properties of organic polymers have also been improved. Delaite *et al.* prepared copolymers of silicone capsules in epoxy resin to reduce the brittle character of the polymers.^[50] Comparable results were obtained for copolymers of methyl methacrylate and butyl acrylate with various siloxanes.^[51] Depending on the size of the siloxane capsules in the polymer, the mechanical performance was improved and the water absorption was significantly reduced.

In other approaches, various copolymers and blends of siloxanes and organic polymers such as polycarbonate with different compositions were prepared and the microstructure and phase separation were characterized.^[52-55] However, potential applications of the hybrid materials were not further investigated.

Other groups developed composites of organic polymers and silazanes for the preparation of ceramics via the PDC route. Garcia *et al.* prepared block copolymers based on polysilazanes and poly(isoprene-block-ethylene oxide) and characterized them in the polymer state.^[56] In the

future, SiCN-type ceramic mesostructures can be processed from the polymer. Similar work has been done by Kamperman *et al.*^[57,58] The pyrolysis of the copolymers resulted in mesoporous ceramics with open accessible pores. This strategy of adding an organic polymer as a sacrificial filler for the pyrolysis is often done in literature to get a high surface area for catalyst carriers.^[59–61]

Hybrid polymers of polysilazanes and acrylonitrile have also been synthesized. The resulting C/SiCN ceramics showed significantly increased oxidation stability compared to pure carbon due to the homogeneously distributed ceramic phase acting as a passivation layer.^[22,23]

Polymethylmethacrylate and polysilazanes were synthesized by free radical polymerization.^[62] The resulting hybrid polymer was used for protective coatings against corrosion for steel substrates. The added polysilazane increased the thermal stability, hydrophobicity and bonding to the substrate.

Despite all the advantages PDCs show their limitation in their shrinkage of 20 – 30 % during pyrolysis, where smaller molecules such as H₂, NH₃, H₂O and CH₄ are released. This is the reason, why PDCs are less suitable for the production of compact components. However, PDCs have a great advantage compared to conventional ceramics: They can be processed like organic polymers which enables dip-coating and spraying techniques to produce coatings,^[26] or the precursors can be spun to fibers. For example, Yajima *et al.* developed SiC fibers from polycarbosilanes which are commercially available as Nicalon fibers.^[63–66] or SiCN fibers were developed by Ribeiro *et al.* from crosslinked polysilazanes.^[11,30,31] The various ceramic fibers and the precursors used are therefore discussed in detail in the following chapters.

2.2 Ceramic Fibers

2.2.1 Carbon Fibers

As mentioned before, carbon fibers are one of the most important technical fibers. They can be processed from a variety of sources. For example, carbon fibers can be obtained by pyrolysis of cellulose fibers^[67] or by mesophase pitch.^[68] However, the largest proportion of carbon fibers is obtained from PAN. The PAN fibers are spun from DMF or DMSO solutions via a wet-spinning process (Chapter 2.3.3). After washing, stretching and drying of the fibers, the most important step, the oxidative stabilization up to 300 °C in air is performed.^[69–71] In this step, complex dehydrogenation and cyclization reactions take place, which lead to a ladder-like structure (Fig. 2). This step is essential for the fiber processing, because the normal PAN structure would not be stable enough to withstand the subsequent manufacturing steps at higher temperatures. Since these reactions are very exothermic and easily lead to overheating and side

reactions, it is important to perform this step with a slow heating rate to prevent damage on the fibers. Other ways to achieve this include catalysts, that lower the crosslinking temperature,^[72–78] or crosslinking the polymer chains by plasma treatment,^[79,80] with electron^[79,81,82] or gamma^[79,83,84] irradiation. However, these methods are only used in research and not yet commercially used for carbon fibers.

After the stabilization step the carbonization is performed. During the pyrolysis volatile molecules including HCN, N₂, H₂, and H₂O are emitted. At temperatures between 1000 and 1600 °C a turbostratic carbon structure is obtained. Carbon fibers carbonized at these temperatures contain tetrahedral carbon-based crosslinks, which connect the graphite layers and the highest tensile strengths of up to 7 GPa can be achieved. If graphitization is subsequently carried out at up to 3000 °C, the carbon crystallites orient themselves along the fiber axis, whereby the highest Young's modulus of up to 600 MPa can be reached, but this also results in a decrease in tensile strength.^[5,21,69,85]

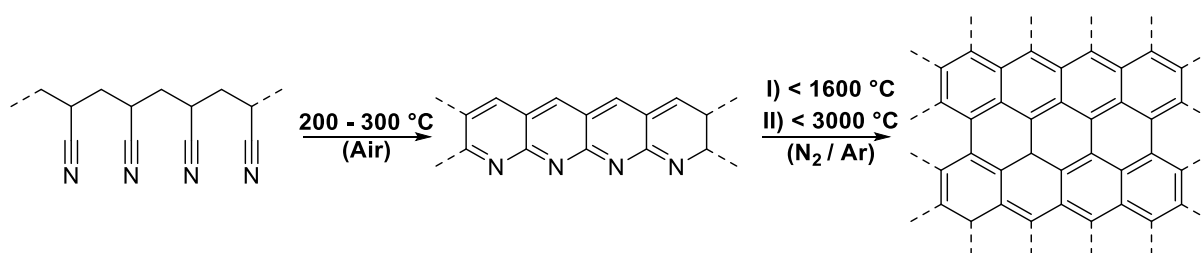


Fig. 2: Structural transformation of PAN to a cyclized ladder-type structure during the stabilization step (200 – 300 °C, air) and to a graphitic carbon structure after carbonization (< 1600 °C) and optional graphitization (< 3000 °C) in an inert atmosphere.^[5,21,69,85]

As previously mentioned, tensile strengths of up to 180 GPa could theoretically be obtained by carbon fibers.^[8,9] The reason why the actual values of commercial fibers are significantly lower is due to defects in the fibers. These defects immediately lead to a catastrophic failure in brittle fibers under tension. However, the probability of such defects occurring per length section decreases with decreasing fiber diameter, which is the reason why fibers with smaller diameters have higher tensile strengths.^[10,11] This principle is also shown by extremely defect-free multiwalled carbon nanotubes (MWCNT) with diameters of 2 – 50 nm, which could achieve tensile strengths of over 100 GPa^[86] or by MWCNT bundles with tensile strengths of 80 GPa.^[87] Unfortunately, the nanotubes can only be produced with lengths in micrometer scale or few centimeters in maximum at the moment. For future carbon fibers, the electrospinning technique (Chapter 2.3.4) could therefore be of interest, with which fiber diameters of 0.1 to 2 μm can be realized.

Despite their high processing temperature, carbon fibers have the decisive disadvantage to start

to decompose in air at temperatures higher than 400 °C.^[88] This severely limits possible applications. For example, if carbon fibers should be used as reinforcing fibers in ceramic matrix composites (CMC), they must first be protected against oxidation in a complex process. For this purpose, SiC layers combined with glass-forming elements such as Si, B, Al or Zr are often applied by chemical vapor deposition (CVD). However, this is very time-consuming and expensive, and the layers tend to form cracks when exposed to temperature changes, which leads than to further oxidation of the exposed carbon.^[15–21]

In another approach, a higher oxidation stability of carbon fibers was achieved intrinsically and without complex coatings. Ribeiro *et al.* synthesized copolymers of acrylonitrile and the commercially available OSZ Durazane 1500 (ML33) and 1800 (HTT1800) (Fig. 3).^[22,23] Depending on the proportion of OSZ in the material the oxidation stability of the resulting C/SiCN fibers significantly increased due to nanoscale and homogeneously distributed Si₃N₄ phases, which act as an oxidative protective layer for the carbon against oxygen from air. For example, with a proportion of 60 wt.% of Durazane 1500 the beginning of the oxidation was delayed to 750 °C. Additionally, the mass loss at 1000 °C significantly decreased to 10 %, compared to a mass loss of nearly 100 % without Durazane 1500 in thermogravimetric analysis (TGA). Unfortunately, only short fiber pieces with a thickness of about 200 μm and no continuous fibers were spun. Therefore, the mechanical properties of the fiber could not be analyzed.

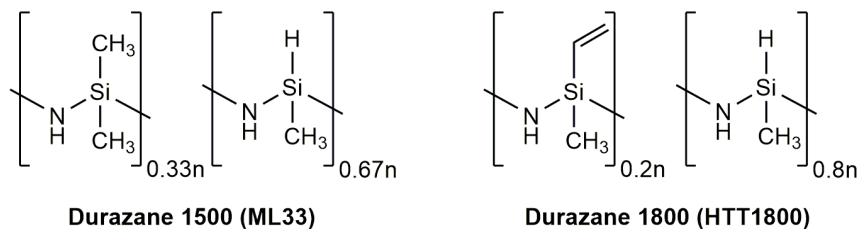


Fig. 3: Chemical structure of the oligosilazanes Durazane 1500 and 1800.^[22,23]

2.2.2 Ceramic SiC Fibers

SiC fibers, meanwhile, have a much higher oxidation stability than carbon fibers and can be used for longer periods at over 1000 °C in air. Therefore, they are mainly used in CMC components. Commercial fibers have a diameter of 7 to 15 μm and tensile strengths of 2 GPa. In industry SiC fibers are melt-spun (Chapter 2.3.2) from polycarbosilanes, stabilized and pyrolyzed at 1000 – 1300 °C.^[63–66,89] The oxygen content is the strongest limitation for the operating temperature, since oxygen is forming SiO₂ phases with silicon. In the beginning this layer acts as a passivating coating and protects the fiber from further oxidation in air, but with temperature changes it is forming cracks and after reaching a certain thickness, flakes off and

the oxidation continues.^[90] To improve the oxidation stability different developments have been made since the 1960s to reduce the oxygen content in the fibers. In the first generation the fibers were spun in a nitrogen atmosphere but the stabilization was performed in air, comparable to carbon fibers. This resulted in a significant incorporation of oxygen into the fibers and limited the mechanical properties and the oxidation stability.^[38,91] In the second generation the polymer fibers were stabilized with gamma or electron irradiation in inert gas. As a result, the oxygen content was reduced and the oxidation stability significantly increased. But because of the high amounts of free carbon the operating temperature was still limited to 1400 °C. Due to the high doses of radiation the price for these fibers starts at 3000 € kg⁻¹ for Hi-Nicalon fibers produced by Nippon carbon.^[38,91-94] To increase the operating temperature even further, crystalline, stoichiometric SiC fibers were produced in the third generation. Commercially, the fibers are marketed for example as Hi-Nicalon S. However, since prices start at 7000 € kg⁻¹, these fibers are mainly used in research.^[38,91,93,94] Unfortunately, these high prices severely limit the applications, which is why SiC fibers are not used in fiber-reinforced plastics.

2.2.3 Ceramic SiCN Fibers

SiCN fibers have the advantage, to be even more oxidation stable than SiC fibers because of the higher activation energy of Si₃N₄ with O₂. Additionally, the polysilazane precursors used for SiCN ceramics are cheaper than polycarbosilanes, which makes them a promising candidate for new ceramic fibers.^[38,95-97]

In the 1980s, Wacker Chemie AG developed a polysilazane synthesized from dichlorodiorganosilanes and dichloromethylsilanes with hexamethyldisilazane and melt-spun and pyrolyzed it to SiCN fibers.^[38,98] Nevertheless, these fibers are not produced anymore and SiCN fibers are not commercially available at the moment but were investigated in research in the last years. Kokott *et al.* developed SiCN fibers from the self-synthesized polycarbosilazane ABSE (Fig. 4).^[36] The precursor was synthesized by the hydrosilation and following ammonolysis of dichloromethylsilane and dichloromethylvinylsilane in inert gas conditions.^[37] Afterwards the polymer was melt-spun, cured by an electronbeam treatment and pyrolyzed at 1100 °C.

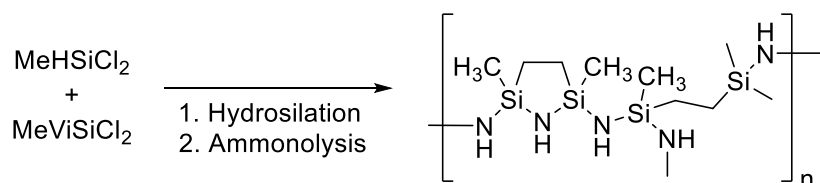


Fig. 4: Synthesis of the oligosilazane ABSE.^[37]

In another example, Flores *et al.* used the previously mentioned OSZ Durazane 1500 (ML33) and Durazane 1800 (HTT1800).^[11,30,31] Since these precursors are liquid and cannot be directly spun into solid fibers, the OSZ was converted into a solid polymer by a polymerization reaction. For this purpose, the N-H and Si-H groups of the OSZ were polymerized with the catalyst tetra-*n*-butylammonium fluoride (TBAF). Calcium borohydride was used as an inhibitor, which catches the fluoride ions to stop the reaction (Fig. 5). By controlling the amount of catalyst and reaction time, the properties of the polymer can be controlled and it can subsequently be spun into polymer fibers by melt-spinning. After a curing step by electron irradiation, the fibers can be pyrolyzed to ceramic SiCN fibers. Due to the formation of a Si₂N₂O/SiO₂ passivating layer and the discussed high activation energy with O₂ the fibers had a high oxidation stability up to 1300 °C even with a high oxygen content from 13 to 28 wt.% in the fibers.

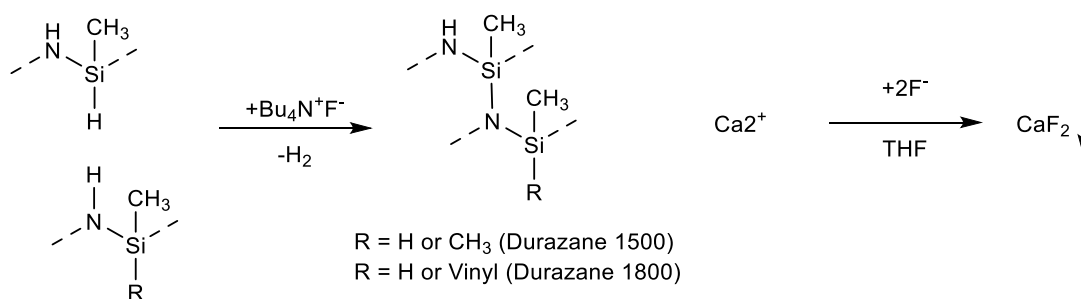


Fig. 5: Crosslinking reaction of the oligosilazanes and termination with calcium borohydride.^[30]

2.2.4 Ceramic oxide Fibers

Besides the different non-oxide fibers, the second category of ceramic fibers are oxide fibers. Most oxide fibers are made of Al₂O₃ or mullite (produced of Al₂O₃ and SiO₂). The largest suppliers for commercial fibers are 3M (Nextel) and Sumitomo (Altex). For Nextel 720 fibers, for example, the tensile strengths reach 2.1 GPa with a diameter of 10 – 12 μm. The density of 3.4 g cm⁻³ is significantly higher than for non-oxide ceramic fibers.^[38] Common applications for ceramic oxide fibers are thermal insulations of furnaces, tubes or thermal protection, as the fibers are already fully oxidized and therefore resistant to oxygen. Mainly oxide fibers are produced via the sol/gel process. The starting materials are spinning compounds of aluminum sols (e.g. aluminum isopropoxide,) or salts (e.g. aluminum nitrate) and silicon sols (e.g. tetraethylorthosilicate) with organic spinning aids such as polyvinylalcohol (PVA) or polyethyleneoxide (PEO), which allow the spinnability in a dry-spinning process. To remove the spinning aids, the fibers are pyrolyzed and sintered. Despite their resistance to oxygen, the biggest limitation for ceramic oxide fibers is creeping of the fibers due to grain growth. Therefore, the long-term operating temperature is limited to about 1000 – 1100 °C.^[94,99–103]

2.3 Processing of Ceramic Fibers

2.3.1 CVD Process

The first commercially developed process for producing ceramic SiC fibers was the chemical vapor deposition (CVD) method. In this approach, a gaseous SiC precursor, for example methyltrichlorosilane, is deposited onto a monofilament of tungsten or carbon. With CVD thick fibers with diameters larger than 75 μm are made. The advantage of the CVD process is that it can be used to produce almost defect-free ceramic fibers, which thus lead to high tensile strengths. For example, SCS-Ultra fibers (Specialty Materials) have a tensile strength of 5.9 GPa and a Young modulus of 415 GPa despite a thick diameter of 142 μm . Due to their high stiffness, these fibers are frequently used for metal matrix composites (MMC) mainly for turbines in military technology. They are commercially distributed under the trade names SCS-6, SCS-9A and SCS-Ultra and as Sigma (TISICS).^[38,90]

2.3.2 Melt-Spinning

Melt-spinning can be used to process fibers with diameters smaller than 30 μm . Since extremely high withdrawing speeds of 1000 – 6000 m min^{-1} are possible and no solvents are needed, it is the most economical spinning process. Therefore, it is the crucial technique for the production of non-oxide ceramic fibers. In melt-spinning, ceramic precursors are molten and spun at temperatures of up to several hundred degrees celsius. If oxygen should be excluded, the spinning process can be carried out under inert gas conditions. Different polymers containing silicon are suitable precursors. Depending on the precursor used, the chemical composition of the subsequent ceramic fiber can be adjusted. For example, SiC fibers can be produced via polycarbosilanes, SiCN fibers via polysilazanes and via boron-containing precursors such as polyborosilazanes BN, SiBN and SiBCN fibers can be made.^[38,94] Before the green fibers can be pyrolyzed to the respective ceramics, the polymers must be crosslinked to prevent a re-melting of the spun fibers. This can be done by oxygen from the air and is used for commercial SiC fibers of the first generation, like Nicalon 200N (Nippon-Carbon), Tyranno Lox-M and Tyranno S (UBE Industries). But this has a negative effect on the fiber properties due to the incorporation of oxygen into the ceramic structure. Alternatively, crosslinking can be done by electron beam treatment, which prevents oxygen from being introduced into the chemical structure and is done, for example, for second generation SiC fibers, like Hi-Nicalon and Hi-Nicalon S (Nippon-Carbon).^[38,91,93,94]

Kokott *et al.* processed ceramic SiCN fibers via melt-spinning of the polycarbosilazane ABSE as discussed in Chapter 2.2.3 ^[36] and additionally later modified them by introducing

MWCNT.^[37]

Ribeiro *et al.* also prepared melt-spun ceramic SiCN fibers from the crosslinked precursors ML33S and HTTS from Durazane 1500 and 1800.^[11,30,31] These fibers were spun after synthesis in a self-made laboratory setup (Fig. 6). The polymer is molten at 80 – 120 °C by a heating sleeve and extruded through a spinneret with nitrogen gas pressure. The green fiber is then wound up and, after a further stabilization step by oxygen from the air or electron irradiation, pyrolyzed to a ceramic SiCN fiber.

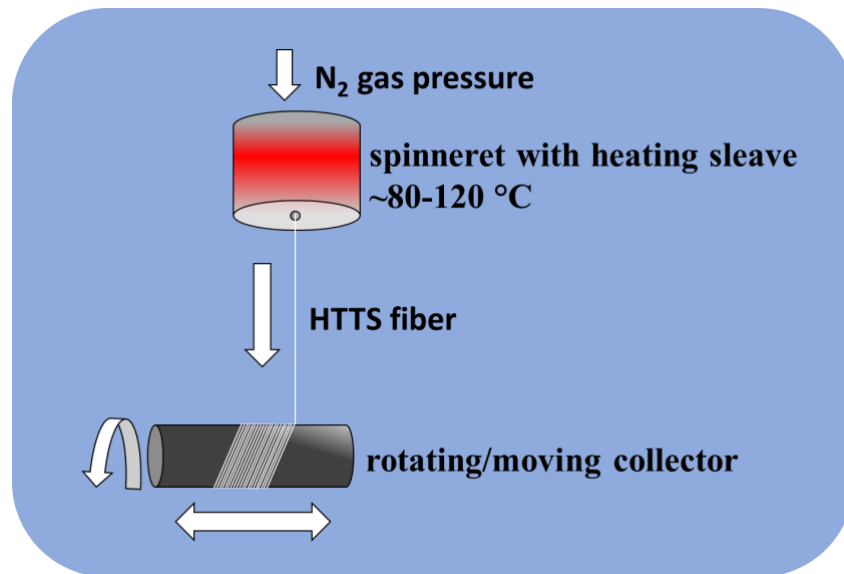


Fig. 6: Principle of the melt-spinning device of Ribeiro *et al.*^[30]

2.3.3 Dry- and wet-spinning

Dry-spinning is usually used for polymers that cannot be melt-spun for example because the material is too temperature sensitive. In dry spinning, a sol or a polymer solution is extruded through a spinneret and dried with a hot gas stream to remove the solvent. Afterwards the precipitated fiber can be stretched and wound up. With this technique small diameters of < 15 μm and high spinning speeds of 300 – 500 m min⁻¹ can be achieved. For ceramic fibers dry-spinning is used for oxide fibers with the sol/gel process. To adjust the right viscosity organic polymers like PVA or PEO can be added as spinning aids. The sol is extruded and after evaporation of the solvent, the gel can be converted into a ceramic fiber by pyrolysis and sintering. Commercially this is done for example by 3M for Nextel fibers.^[104,105] Another option is dry-spinning for polymer fibers for example for PAN dissolved in DMF or polyvinylchloride (PVC) in acetone. For textiles PAN fibers are often made with dry-spinning, but for the production of carbon fibers, the process is less favorable because too many defects are introduced into the fibers which makes wet-spinning more suitable for this purpose.^[5,106]

The second reason why wet-spinning is used for the production of carbon fibers from PAN is because melt-spinning is not possible. The reason is that the melting temperature of PAN is higher than the decomposition temperature of the polymer.^[107]

For wet-spinning, solutions with 15 – 25 wt.% PAN in *N,N*-dimethyl formamide (DMF), dimethyl sulfoxide (DMSO), dimethyl acetamide (DMAc) are spun into a precipitation bath. In principle the bath consists of a liquid, mostly water, which is miscible with the solvent but does not dissolve the polymer. This causes the polymer fiber to precipitate in the bath. Precipitation is a diffusion-controlled process. If the diffusion rate is too high, the fiber will solidify too quickly on the outside, but is still liquid on the inside. Greater shrinkage of the fiber occurs during drying and leads in turn to a bean- or sickle shape. This can be prevented by a soft fiber surface via a slow diffusion process. The speed of the diffusion process can be adjusted with the solvent gradient and the temperature. In principle, a larger solvent content in the bath or a lower bath temperature leads to a lower diffusion rate and therefore to a circular shape.

In the basic set-up the polymer solution is extruded through multiple holes into the precipitation bath. After the spinning process, the fiber is washed and drawn under hot water or water steam to remove excess solvent and increase the orientation of the polymer chains for a higher tensile strength (Fig. 7). Afterwards, the green fiber can be converted to the carbon fiber by the previously discussed temperature treatment.^[69,106,108,109]

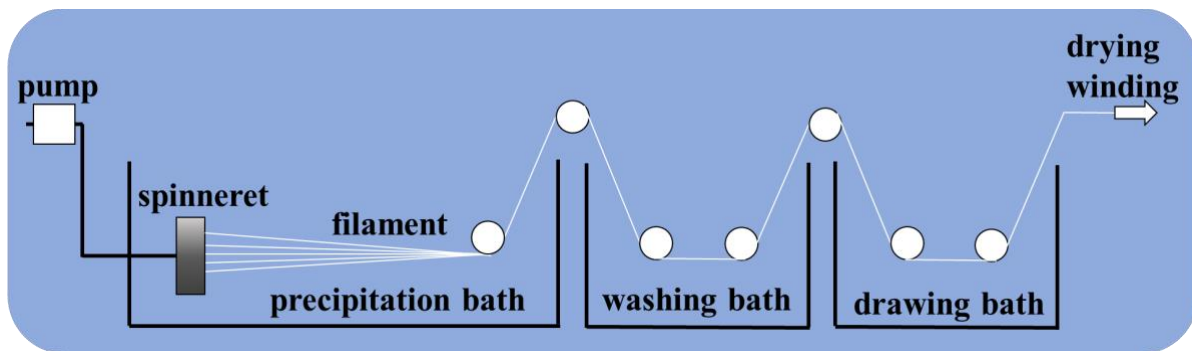


Fig. 7: Principle of a wet-spinning setup for PAN fibers.^[106]

2.3.4 Electrospinning

In principle, electrospinning is a process for producing 2D nonwovens from polymer nanofibers.^[110,111] In electrospinning, a polymer solution is continuously pumped through a syringe. During pumping, the droplets are electrostatically charged by friction. When a high voltage up to 50 kV is applied between the cannula and the collector, the solution is accelerated towards the collector. On its way, the solvent evaporates and deposits solid polymer fibers. Due to the surface tension, the droplets would normally form a sphere at the tip, but because of the electric field the droplets are stretched to a cylindrical shape. Since the solution is pumped continuously, a jet is created. A suitable voltage and a sufficient polymer concentration prevent the jet from partially collapsing back into droplets and forming beads on the fibers. Owing to the high voltage, the polymer fiber is strongly accelerated and stretched to diameters in the nanometer or low micrometer regime.

In principle, electrospinning is a very complex process and many variables have to be optimized to obtain a stable spinning process.^[110,112] As already mentioned, the applied voltage is crucial, as it causes the formation of the so-called Taylor cone at the tip of the needle (Fig. 8). This characteristic shape of the droplet is important to achieve a stable jet and a continuous fiber formation. If the voltage is too high, the result is a reduction of the Taylor cone size, as the jet is too strongly accelerated, and therefore causes beads on the fibers. Furthermore, the applied voltage cannot be treated independently, as a balance has to be found between the voltage and the flow rate. The transport of the solution to the collector and the flow rate have to be in equilibrium to prevent the formation of drops or beads. Another important parameter is the distance between the tip and collector. The larger it is, the smaller the fiber diameter will be, since the fibers get more stretched. As mentioned before, the polymer concentration in the spinning solution is decisive as well, since a too low concentration causes a breakdown of the jet into a droplet shape and the fibers contain beads.

After optimizing the parameters, different collectors can be used to change the morphology of the nonwovens. The simplest collector is a flat plate to produce planar nonwovens. Alternatively, a rotating wheel or roller can be used. With a slow rotational speed, the fibers are deposited randomly, comparable to plate collector, but with a higher speed, the fibers become more parallel and are spun in a preferential direction. By using parallel electrodes as collectors, stronger aligned fibers can be obtained, but only fiber lengths of a few centimeters are possible with only very thin fiber layers. The schematic structure of an electrospinning device with different collectors can be seen in Fig. 8.^[110,113]

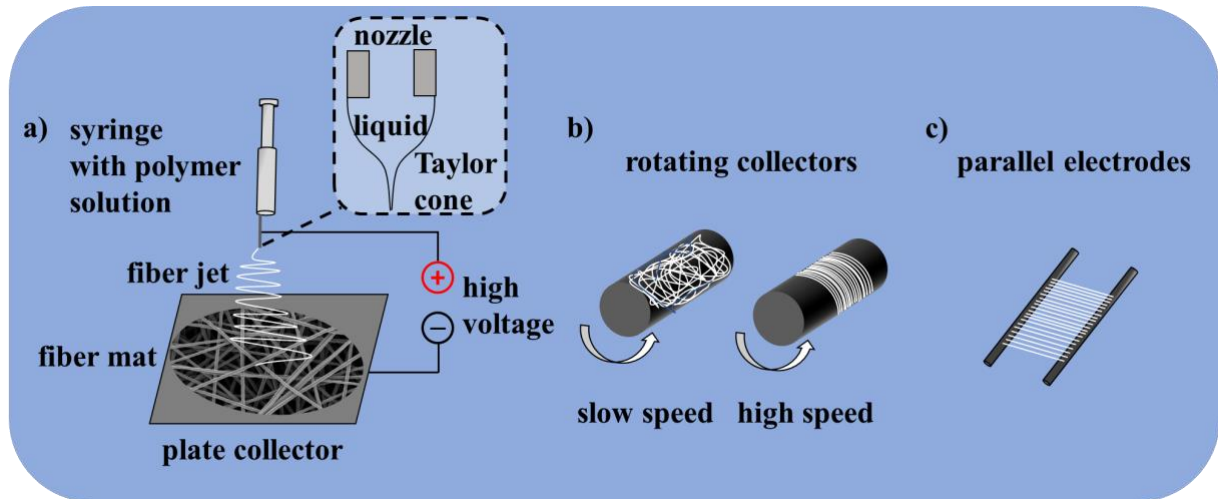


Fig. 8: Schematic structure of an electrospinning process with a) a plate collector, b) rotating collectors and c) parallel electrodes. The magnified area shows the characteristic Taylor cone forming at the tip of the cannula.

In a special electrospinning approach, continuous multifibrillar nanofibers can be spun (Fig. 9 a).^[13] For this purpose, two syringes are used which are fixed opposite to each other and charged positively and negatively, respectively. As a result, the spun fibers attract each other and get caught by a fast-rotating cylinder between the two syringes and wound continuously. Immediately after spinning, the fibers are largely disordered, but by drawing them through a tube furnace using two rollers running at different speeds, the nanofibers can be almost aligned perfectly (Fig. 9 b).

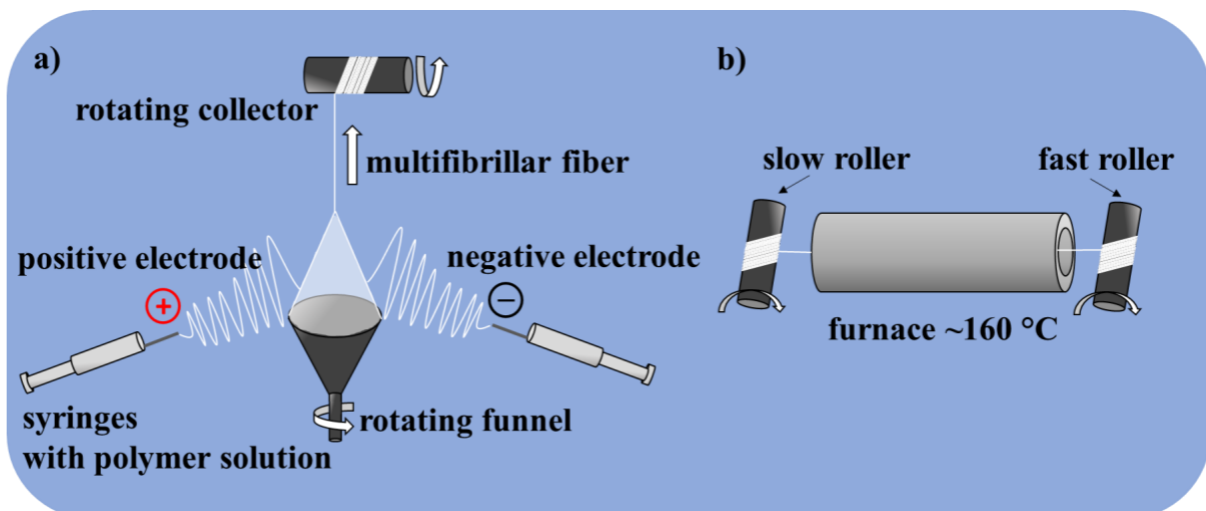


Fig. 9: Schematic structure of a) a multifibrillar fiber spinning setup and b) a tube furnace with two rollers rotating a different speed stretching and alignment of the fibers.

In principle, almost all soluble polymers with sufficiently high molecular weight can be processed by electrospinning.^[110] In the literature, this has been done with a variety of polymers, including polystyrene (PS),^[114] polycarbonate (PC),^[115] aliphatic and aromatic polyamides

(PA),^[116] polyimides (PI),^[117] polyethyleneterephthalate (PET),^[118] polyurethanes (PU),^[119] polyvinylchloride (PVC),^[120,121] poly(methyl methacrylate) (PMMA),^[122] cellulose acetate (CA),^[123] polysiloxanes^[124] and many more.^[110,111] Furthermore, a big variety of synthesized polymers can be used or modified.^[110,125,126] For the processing of carbon fibers, electrospinning of PAN from DMF solutions is very interesting. Vansco *et al.* systematically investigated the electrospinning process of PAN and the dependence of the fiber diameter on the polymer concentration and the voltage. Subsequently, the PAN fibers are converted into carbon fibers by pyrolysis.^[127] In the vast majority of publications, simple carbon fiber nonwovens, often with further modification with metals or ions such as Li, Sn, Ru and Pd were produced. These nonwovens are interesting as electrode material for batteries, fuel cells or because of the large surface area of the fibers for catalysis and filtration applications.^[128–130]

Due to the small fiber diameters in the nanometer range obtained by electrospinning this technology is also highly interesting for processing carbon or ceramic fibers with extremely high tensile strengths. Since for brittle fibers usually only one defect is enough to lead to a catastrophic failure, the average tensile strength increases exponentially with smaller fiber diameters, because the probability for a defect per unit length decreases. As mentioned before, this principle was already discovered by Griffith in 1921 for glass fibers^[10] and also confirmed for melt-spun ceramic SiCN fibers.^[11] Therefore, Zhou *et al.* used a rotating collector to electrospin aligned PAN nanofiber bundles. The obtained fiber bundles were wrapped around a glass rod to apply a force on the fibers for the subsequent stabilization and pyrolysis programs. With this technique tensile strengths of 300 – 600 MPa and Young's moduli of 40 – 60 GPa were obtained. A very similar approach was also pursued by Moon *et al.* where a maximum tensile strength of 1 GPa was achieved.^[131] Both approaches have the disadvantage that the length of the fiber bundles were limited by the diameter of the wheel and thus only fibers with a few centimeters in length can be produced. In addition, the tensile strengths are well below commercial carbon fibers and far from the theoretical maximum of 180 GPa,^[8,9] the reason for this are often entangled or poorly aligned fibers.

Another option is the previously discussed technique of electrospinning of continuous multifibrillar fibers. Liao *et al.* additionally crosslinked the PAN nanofibers via PEG groups using a click reaction. This resulted in polymer fibers with a high toughness of 140 J g⁻¹ and high tensile strengths of 1.2 GPa, which even surpassed the properties of spider silk.^[13] Xie *et al.* developed a similar approach and investigated different stretching ratios of the multifibrillar fibers.^[14] The polymer fibers had a tensile strength of up to 362 MPa. Additionally, small fiber pieces were pyrolyzed to carbon fibers at 800 °C and tensile strengths up to 1.1 GPa were

obtained. In this study no stabilization of the fibers or optimization to a continuous process was done, and it remained open whether higher tensile strengths could be achieved.

In literature, not only PAN, but also PDCs were used for the production of electrospun ceramic fibers. Xiao *et al.* fabricated flat SiCN nonwovens from Durazane 1800.^[132] Similar experiments were made by Ramlow *et al.*^[133] and Ribeiro *et al.*^[134] using crosslinked HTTS. In these publications, the focus of possible applications was the shielding of electromagnetic waves, new filter systems or catalytic supports. But the processing of aligned ceramic nanofibers via electrospinning with high tensile strengths is not known in the literature yet and was therefore investigated in this dissertation.

REFERENCES

- [1] A. C. Clarke, *The Fountains of Paradise*, Harcourt, New York, **1979**.
- [2] F. Schätzing, *Limit*, Kiepenheuer & Witsch, Cologne, **2009**.
- [3] Jr. D.V. Smitherman, *NASA Conference Publication CP-2000–210429* **2000**, 46.
- [4] B. C. Edwards, *Acta Astronaut* **2000**, 47, 735–744.
- [5] E. Frank, L. M. Steudle, D. Ingildeev, J. M. Spörl, M. R. Buchmeiser, *Angew. Chem. Int. Ed.* **2014**, 53, 5262–5298.
- [6] S. Chand, *J. Mater. Sci.* **2000**, 35, 1303–1313.
- [7] M. Sauer, D. Schüppel, *Market Report 2022 The Global Market for Carbon Fibers and Carbon Composites* **2023**.
- [8] Fitzer E., *Carbon Fibers and Their Composites*, Springer-Verlag, Berlin, Heidelberg, **1985**.
- [9] J.-B. Donnet, R. Chaned Bansal, *Carbon Fibers, Third Edition*, CRC Press, **1998**.
- [10] A. A. Griffith, *Philos. Trans. R. Soc. Lond.* **1921**, 221, 163–198.
- [11] O. Flores, R. K. Bordia, S. Bernard, T. Uhlemann, W. Krenkel, G. Motz, *RSC Adv.* **2015**, 5, 107001–107011.
- [12] “<https://www.toraycma.com/products/carbon-fiber/>”, (opened: 03.02.2024)
- [13] X. Liao, M. Dulle, J. M. De Souza E Silva, R. B. Wehrspohn, S. Agarwal, S. Förster, H. Hou, P. Smith, A. Greiner, *Science* **2019**, 366, 1376–1379.
- [14] Z. Xie, H. Niu, T. Lin, *RSC Adv.* **2015**, 5, 15147–15153.
- [15] J. E. Sheehan, *Carbon* **1989**, 27, 709–715.
- [16] F. Lamouroux, S. Bertrand, R. Pailler, R. Naslain, M. Cataldi, *Compos. Sci. Technol.* **1999**, 59, 1073–1085.
- [17] R. Weiss, in *High Temperature Ceramic Matrix Composites*, Wiley-VCH Verlag GmbH & Co. KGaA, Weinheim, FRG, **2006**, 440–456.
- [18] L. A. Tkachenko, A. Yu. Shaulov, A. A. Berlin, *Inorg. Mater.* **2012**, 48, 213–221.
- [19] C. Hu, S. Pang, S. Tang, Z. Yang, S. Wang, H.-M. Cheng, *Corros. Sci.* **2015**, 94, 452–458.
- [20] X. Yang, C. Zhao-hui, C. Feng, *J. Asian Ceram. Soc.* **2014**, 2, 305–309.
- [21] P. Morgan, *Carbon Fibers and Their Composites*, CRC Press, **2005**.
- [22] L. Ribeiro, A. Bezerra, C. Gervais, S. Bernard, R. Machado, G. Motz, *J. Eur. Ceram. Soc.* **2021**, 41, 3285–3291.

- [23] L. F. B. Ribeiro, O. Flores, P. Furtat, C. Gervais, R. Kempe, R. A. F. Machado, G. Motz, *J. Mater. Chem. A* **2017**, *5*, 720–729.
- [24] P. Colombo, G. Mera, R. Riedel, G. D. Sorarù, *J. Am. Ceram. Soc.* **2010**, *93*, 1805–1837.
- [25] R. Riedel, G. Mera, R. Hauser, A. Kloneczynski, *J. Ceram. Soc. Jpn.* **2006**, *114*, 425–444.
- [26] G. Barroso, Q. Li, R. K. Bordia, G. Motz, *J. Mater. Chem. A* **2019**, *7*, 1936–1963.
- [27] G. Barroso, Q. Li, G. Motz, R. K. Bordia, *Am. Ceram. Soc. Bull.* **2017**, *96*, 42–49.
- [28] S. Traßl, D. Suttor, G. Motz, E. Rössler, G. Ziegler, *J. Eur. Ceram. Soc.* **2000**, *20*, 215–225.
- [29] Y. Iwamoto, W. Völger, E. Kroke, R. Riedel, T. Saitou, K. Matsunaga, *J. Am. Ceram. Soc.* **2004**, *84*, 2170–2178.
- [30] O. Flores, T. Schmalz, W. Krenkel, L. Heymann, G. Motz, *J. Mater. Chem. A* **2013**, *1*, 15406–15415.
- [31] O. Flores, L. Heymann, G. Motz, *Rheol. Acta* **2015**, *54*, 517–528.
- [32] G. Mikl, R. Obmann, S. Schörpf, R. Liska, T. Konegger, *Adv. Eng. Mater.* **2019**, *21*, 1900052.
- [33] M. Hoffmann, M. Zahedtalaban, J. Denk, A. Horcher, H. Ruckdäschel, S. Schafföner, G. Motz, *Open Ceramics* **2023**, *15*, 100384.
- [34] A. Qazzazie-Hauser, K. Honnef, T. Hanemann, *Polymers* **2021**, *13*, 2424.
- [35] S. K. Reddy, N. B. Cramer, T. Cross, R. Raj, C. N. Bowman, *Chem. Mater.* **2003**, *15*, 4257–4261.
- [36] S. Kokott, G. Motz, *Soft. Mater.* **2007**, *4*, 165–174.
- [37] S. Kokott, G. Motz, *Materwiss. Werksttech.* **2007**, *38*, 894–900.
- [38] O. Flores, R. K. Bordia, D. Nestler, W. Krenkel, G. Motz, *Adv. Eng. Mater.* **2014**, *16*, 621–636.
- [39] C. M. Liauw, G. C. Lees, S. J. Hurst, R. N. Rethon, S. Ali, *Compos. - A: Appl. Sci. Manuf.* **1998**, *29*, 1313–1318.
- [40] B. Wang, X. Wang, G. Tang, Y. Shi, W. Hu, H. Lu, L. Song, Y. Hu, *Compos. Sci. Technol.* **2012**, *72*, 1042–1048.
- [41] M. L. Q. A. Kaneko, R. B. Romero, R. E. F. De Paiva, M. I. Felisberti, M. C. Gonçalves, I. V. P. Yoshida, *Polym. Compos.* **2013**, *34*, 194–203.
- [42] Z. Hu, L. Chen, B. Zhao, Y. Luo, D. Y. Wang, Y. Z. Wang, *Polym. Degrad. Stab.* **2011**, *96*, 320–327.
- [43] Z. Tang, Y. Li, Y. J. Zhang, P. Jiang, *Polym. Degrad. Stab.* **2012**, *97*, 638–644.
- [44] X. E. Cheng, W. Shi, *Prog. Org. Coat.* **2010**, *69*, 252–259.

- [45] C. L. Chiang, R. C. Chang, *Compos. Sci. Technol.* **2008**, *68*, 2849–2857.
- [46] F. Laoutid, L. Bonnaud, M. Alexandre, J. M. Lopez-Cuesta, P. Dubois, *Mater. Sci. Eng. R Rep.* **2009**, *63*, 100–125.
- [47] J. Gilman, T. Kashiwagi, R. Harris, S. Lomakin, *Chemistry and technology of polymer additives.* **1999**, 135–50.
- [48] J. Lichtenhan, J. Gilman, *US Patent* **2002**, *US6362279B2*.
- [49] W. Zhou, H. Yang, *Thermochim. Acta* **2007**, *452*, 43–48.
- [50] C. Delaite, S. Bistac, D. Rusu, *Molecules* **2023**, *28*, 6300.
- [51] M. Zou, F. Huang, J. Nie, Z. Zhang, X. Ge, *Polym. Int.* **2005**, *54*, 861–869.
- [52] Y. Li, K. Hu, X. Han, Q. Yang, Y. Xiong, Y. Bai, X. Guo, Y. Cui, C. Yuan, H. Ge, Y. Chen, *Langmuir* **2016**, *32*, 3670–3678.
- [53] A. Abdilla, C. A. D’Ambra, Z. Geng, J. J. Shin, M. Czuczola, D. J. Goldfeld, S. Biswas, J. M. Mecca, S. Swier, T. D. Bekemeier, D. S. Laitar, M. W. Bates, C. M. Bates, C. J. Hawker, *J. Polym. Sci.* **2021**, *59*, 2114–2128.
- [54] Q. Zaman, K. M. Zia, M. Zuber, Y. N. Mabkhot, F. Almalki, T. Ben Hadda, *Int. J. Plast. Technol.* **2019**, *23*, 261–282.
- [55] Y. Cai, D. Gardner, G. T. Caneba, *J. Adhes. Sci. Technol.* **1999**, *13*, 1017–1027.
- [56] C. B. W. Garcia, C. Lovell, C. Curry, M. Faught, Y. Zhang, U. Wiesner, *J. Polym. Sci. B Polym. Phys.* **2003**, *41*, 3346–3350.
- [57] M. Kamperman, M. A. Fierke, C. B. W. Garcia, U. Wiesner, *Macromol.* **2008**, *41*, 8745–8752.
- [58] M. Kamperman, C. B. W. Garcia, P. Du, H. Ow, U. Wiesner, *J. Am. Chem. Soc.* **2004**, *126*, 14708–14709.
- [59] T. Schmalz, J. M. Hausherr, W. Muller, T. Kraus, W. Krenkel, R. Kempe, G. Motz, *J. Ceram. Soc. Jpn.* **2011**, *119*, 477–482.
- [60] T. Schmalz, T. Kraus, M. Günthner, C. Liebscher, U. Glatzel, R. Kempe, G. Motz, *Carbon* **2011**, *49*, 3065–3072.
- [61] A. K. Boehm, E. Ionescu, M. Koch, M. Gallei, *Molecules* **2019**, *24*, 3553.
- [62] T. Coan, G. S. Barroso, R. A. F. MacHado, F. S. De Souza, A. Spinelli, G. Motz, *Prog. Org. Coat.* **2015**, *89*, 220–230.
- [63] S. Yajima, K. Okamura, J. Hayashi, *Chem. Lett.* **1975**, *4*, 1209–1212.
- [64] S. Yajima, J. Hayashi, M. Omori, *Chem. Lett.* **1975**, *4*, 931–934.
- [65] S. Yajima, K. Okamura, J. Hayashi, M. Omori, *J. Am. Ceram. Soc.* **1976**, *59*, 324–327.

- [66] T. O. Branch, T. Uni-, S. Yajima, Y. Hasegawa, J. Hayashi, M. Iimura, *J. Mater. Sci.* **1978**, *13*, 2569–2576.
- [67] A. G. Dumanlı, A. H. Windle, *J. Mater. Sci.* **2012**, *47*, 4236–4250.
- [68] R. Naslain, in *Advanced Inorganic Fibers*, **2000**, 233–264.
- [69] E. Frank, F. Hermanutz, M. R. Buchmeiser, *Macromol. Mater. Eng.* **2012**, *297*, 493–501.
- [70] S. Dalton, F. Heatley, P. M. Budd, *Polymer* **1999**, *40*, 5531–5543.
- [71] Q. Wen, Z. Yu, R. Riedel, *Prog. Mater. Sci.* **2020**, *109*.
- [72] W. X. Zhang, Y. Z. Wang, *J. Appl. Polym. Sci.* **2002**, *85*, 153–158.
- [73] A. Shiedlin, G. Marom, A. Zilkha, *Polymer* **1985**, *26*, 447–451.
- [74] J. Mittal, R. B. Mathur, *Science* **1997**, *35*.
- [75] R. B. Mathur, D. Gupta, O. P. Bahl, T. L. Dhami, *J. Fiber Sci.* **1984**, *20*, 227–234.
- [76] T. H. Ko, L. C. Huang, *J. Appl. Polym. Sci.* **1998**, *70*, 2409–2415.
- [77] R. Chen, Y. Hu, Z. Shen, P. Pan, X. He, K. Wu, X. Zhang, Z. Cheng, *J. Mater. Chem. A* **2017**, *5*, 12914–12921.
- [78] N. Yusof, A. F. Ismail, *J. Anal. Appl. Pyrolysis.* **2012**, *93*, 1–13.
- [79] H. K. Shin, M. Park, H. Y. Kim, S. J. Park, *Carbon Lett.* **2015**, *16*, 11–18.
- [80] S. Y. Kim, S. Lee, S. Park, S. M. Jo, H. S. Lee, H. I. Joh, *Carbon* **2015**, *94*, 412–416.
- [81] H. K. Shin, M. Park, P. H. Kang, H. S. Choi, S. J. Park, *J. Ind. Eng. Chem.* **2014**, *20*, 3789–3792.
- [82] S. Park, S. H. Yoo, H. R. Kang, S. M. Jo, H. I. Joh, S. Lee, *Sci. Rep.* **2016**, *6*, 1–9.
- [83] W. Zhao, Y. Lu, J. Wang, Q. Chen, L. Zhou, J. Jiang, L. Chen, *Polym. Degrad. Stab.* **2016**, *133*, 16–26.
- [84] W. Liu, M. Wang, Z. Xing, Y. Qi, G. Wu, *Radiat. Phys. Chem.* **2012**, *81*, 622–627.
- [85] Z. Wangxi, L. Jie, W. Gang, *Carbon* **2003**, *41*, 2805–2812.
- [86] B. Peng, M. Locascio, P. Zapol, S. Li, S. L. Mielke, G. C. Schatz, H. D. Espinosa, *Nat. Nanotechnol.* **2008**, *3*, 626–631.
- [87] Y. Bai, R. Zhang, X. Ye, Z. Zhu, H. Xie, B. Shen, D. Cai, B. Liu, C. Zhang, Z. Jia, S. Zhang, X. Li, F. Wei, *Nat. Nanotechnol.* **2018**, *13*, 589–595.
- [88] N. I. Baklanova, T. M. Zima, A. I. Boronin, S. V. Kosheev, A. T. Titov, N. V. Isaeva, D. V. Graschenkov, S. S. Solntsev, *Surf. Coat. Technol.* **2006**, *201*, 2313–2319.
- [89] G. Fritz, J. Grobe, D. Kummer, *Adv. Inorg. Chem. Radiochem.* **1965**, 349–418.
- [90] A. R. Bunsell, M.-H. Berger, *Fine Ceramic Fibers*, Marcel Dekker, Inc., New York, **1999**.

- [91] A. R. Bunsell, A. Piant, *J. Mater. Sci.* **2006**, *41*, 823–839.
- [92] H. Ichikawa, *J. Ceram. Soc. Jpn.* **2006**, *114*, 455–460.
- [93] T. Ishikawa, *Adv. Polym. Sci.* **2005**, *178*, 109–144.
- [94] D. Schawaller, B. Clauß, M. R. Buchmeiser, *Macromol. Mater. Eng.* **2012**, *297*, 502–522.
- [95] D. Mocaer, G. Chollon, R. Pailler, L. Filipuzzi, R. Naslain, *J. Mater. Sci.* **1993**, *28*, 3059–3068.
- [96] G. Chollon, *J. Eur. Ceram. Soc.* **2000**, *20*, 1959–1974.
- [97] L. U. J. T. Ogbuji, E. J. Opila, *J. Electrochem. Soc.* **1995**, *142*, 925–930.
- [98] A. Rengstl, *EU Patent*, **1988**, 0 255 132 A2.
- [99] D. S. Tucker, J. S. Sparks, D. C. Esker, *Ceram. Bull.* **1990**, *69*, 1971–1974.
- [100] T. Maki, S. Sakka, *J. Non-Cryst. Solids* **1988**, *100*, 303–308.
- [101] C. Li, Y. Zhang, H. Gong, J. Zhang, L. Nie, *Mater. Chem. and Phys.* **2009**, *113*, 31–35.
- [102] B. Clauss, *Angew. Makromol. Chem.* **1994**, *217*, 139–158.
- [103] K. C. Song, *Mater. Lett.* **1998**, *35*, 290–296.
- [104] G. Motz, R. K. Bordia, in *Handbook of Textile Fibre Structure*, Elsevier, **2009**, 378–424.
- [105] H. Scholz, J. Vetter, R. Herborn, A. Ruedinger, *Int. J. Appl. Ceram. Technol.* **2020**, *17*, 1636–1645.
- [106] J. Kaur, K. Millington, S. Smith, *J. Appl. Polym. Sci.* **2016**, *133*, 1–14.
- [107] A. R. Bunsell, *Handbook of Properties of Textile and Technical Fibres*, Woodhead Publishing, **2018**.
- [108] Y.-X. Wang, C.-G. Wang, M.-J. Yu, *J. Appl. Polym. Sci.* **2007**, *104*, 3723–3729.
- [109] J. Chen, C. G. Wang, X. G. Dong, H. Z. Liu, *J. Polym. Res.* **2006**, *13*, 515–519.
- [110] J. H. Wendorff, S. Agarwal, A. Greiner, *Electrospinning Materials, Processing and Applications*, Wiley, Weinheim, Germany, **2008**.
- [111] S. Agarwal, A. Greiner, J. H. Wendorff, *Chem. Ing. Tech.* **2008**, *80*, 1671–1676.
- [112] A. Haider, S. Haider, I.-K. Kang, *Arab. J. Chem.* **2018**, *11*, 1165–1188.
- [113] S. T. M., A. Bin Arshad, P. T. Lin, J. Widakdo, M. H. K., H. F. M. Austria, C.-C. Hu, J.-Y. Lai, W.-S. Hung, *RSC Adv.* **2021**, *11*, 9638–9663.
- [114] C. L. Casper, J. S. Stephens, N. G. Tassi, D. B. Chase, J. F. Rabolt, *Macromol.* **2004**, *37*, 573–578.
- [115] J. Shawon, C. Sung, *J. Mater. Sci.* **2004**, *39*, 4605–4613.
- [116] M. Afshari, R. Kotek, A. E. Tonelli, D.-W. Jung, in *Nanofibers and Nanotechnology in Textiles*, Elsevier, **2007**, 71–89.

- [117] Y. Ding, H. Hou, Y. Zhao, Z. Zhu, H. Fong, *Prog. Polym. Sci.* **2016**, *61*, 67–103.
- [118] J. A. Abbas, I. A. Said, M. A. Mohamed, S. A. Yasin, Z. A. Ali, I. H. Ahmed, *IOP Conf. Ser. Mater. Sci. Eng.* **2018**, *454*, 012130.
- [119] A. Pedicini, R. J. Farris, *Polymer* **2003**, *44*, 6857–6862.
- [120] M. J. Jafari, E. Akhlaghi Pirposhteh, M. Farhangian, S. Khodakarim Ardakani, E. Tavakol, S. F. Dehghan, A. Khalilinejad, *Res. J. Text. Appar.* **2024**, *28*, 84–99.
- [121] L. Quoc Pham, M. V. Uspenskaya, R. O. Olekhovich, R. A. Olvera Bernal, *Fibers* **2021**, *9*, 12.
- [122] P. Gupta, C. Elkins, T. E. Long, G. L. Wilkes, *Polymer* **2005**, *46*, 4799–4810.
- [123] M. W. Frey, *Polym. Rev.* **2008**, *48*, 378–391.
- [124] Z. Ren, C. Gervais, G. Singh, *RSC Adv.* **2020**, *10*, 38446–38455.
- [125] Z.-M. Huang, Y.-Z. Zhang, M. Kotaki, S. Ramakrishna, *Compos. Sci. Technol.* **2003**, *63*, 2223–2253.
- [126] S. Ramakrishna, K. Fujihara, W.-E. Teo, T.-C. Lim, Z. Ma, *An Introduction to Electrospinning and Nanofibers*, World Scientific, **2005**.
- [127] S. Y. Gu, J. Ren, G. J. Vancso, *Eur. Polym. J.* **2005**, *41*, 2559–2568.
- [128] S. K. Nataraj, K. S. Yang, T. M. Aminabhavi, *Prog. Polym. Sci.* **2012**, *37*, 487–513.
- [129] M. Inagaki, Y. Yang, F. Kang, *Adv. Mat.* **2012**, *24*, 2547–2566.
- [130] H. Esfahani, R. Jose, S. Ramakrishna, *Mater.* **2017**, *10*, 1238.
- [131] S. C. Moon, R. J. Farris, *Carbon* **2009**, *47*, 2829–2839.
- [132] F. Xiao, H. Sun, J. Li, X. Guo, H. Zhang, J. Lu, Z. Pan, J. Xu, *Ceram. Int.* **2020**, *46*, 12773–12781.
- [133] H. Ramlow, C. Marangoni, G. Motz, R. A. F. Machado, *Chem. Eng. J. Adv.* **2022**, *9*, 100220.
- [134] L. F. B. Ribeiro, R. S. Cunha, A. de Noni, R. A. F. Machado, G. Motz, S. Y. G. González, *Adv. Eng. Mater.* **2022**, *24*, 2100321.

3 SYNOPSIS

As explained in the introduction, the main objective of this work was to process fibers from polymer blends of PAN and OSZ with different spinning techniques, like wet- and electrospinning. Afterwards the polymer fibers were converted to C or C/SiCON hybrid fibers and the chemical, structural and mechanical properties were characterized. The results were published in three different papers, which are summarized here and printed completely in Chapter 5.

Chapter 5.1 deals with the electrospinning of the polymer blends into nonwovens and in particular, the characterization of the exceptional thermoelectric properties of the C/SiCON hybrid fibers. The results were published in 2023 in the journal *Science Advances*.

In Chapter 5.2, the results from 5.1 were refined and the PAN/OSZ blends were electrospun into continuous multifibrillar fibers, to achieve high tensile strengths. After optimized stabilization and pyrolysis steps were performed, continuous multifibrillar C/SiCON fibers consisting of thousands of individual nanofibers were obtained. Since the stabilization and pyrolysis steps were also performed continuously, light weight multifibrillar nanofibers with lengths of several meters, and after additional treatment by electron irradiation, with high mechanical properties were obtained. The results have been published in the journal *Scientific Reports*.

In the publication in Chapter 5.3, a wet-spinning process for polymer blends with 0, 20 and 40 wt.% of OSZ was developed and the temperature steps were performed continuously as well. The resulting C/SiCON hybrid fibers had a significantly higher oxidation- stability compared to pure carbon fibers. Additionally, high tensile strengths of 2.0 GPa for relatively large diameters of 20 μm were obtained. The results have been published in the journal *Materials Horizons*.

3.1 Extremely low thermal conductivity and high electrical conductivity of sustainable carbon-ceramic electrospun nonwoven materials

In this part of the work ceramic nanofiber nonwovens were processed by electrospinning. The fibers were spun from blends from PAN and up to 50 wt.% OSZ. After the stabilization (250 °C, air) and pyrolysis steps (1000 °C, N₂) highly flexible and foldable C/SiCON nonwovens were obtained. The properties and structure of the obtained nonwovens were subsequently investigated in the publication. Raman measurements showed an amorphous carbon structure for all different compositions. This amorphous carbon structure was also confirmed by WAXS measurements. Elemental analysis and ²⁹Si solid state NMR revealed a high oxygen content in the fibers, which is incorporated by the oxidative stabilization step and the electrospinning process in air. In addition, various SiC_xO_y, SiN_xO_y, or SiC_xN_y species could be detected. In contrast the material showed a high electrical conductivity of 20.1 S cm⁻¹, which was only slightly reduced to 4.2 S cm⁻¹ even by adding 50 wt.% OSZ. This is based on the high electrical conductivity of carbon, which is not interrupted by the ceramic phases and thus retains its conductivity over the entire length of the nonwovens. The thermal conductivities, in contrast, decreased with increasing OSZ content to a very low value of 19.2 mW m⁻¹ K⁻¹ (C/SiCON-50). The structure of the material, responsible for this special combination of high electrical and low thermal conductivities, was determined by STEM-EDS analysis. The fibers consist of a "sea-island" nanostructure. The "carbon-sea" acts as the electron transporting medium and conducts the electric current, while the interfaces between the carbon and the "ceramic-islands" lead to phonon scattering, in addition to boundary scattering between the individual fibers, which strongly reduces the thermal conductivity (Fig. 10 a). Thus, a unique material was developed, which has an optimal thermal insulation with a high electrical conductivity at the limit of the extrapolated Wiedemann-Franz law (Fig. 10 b). In addition, the C/SiCON nonwovens showed an extremely high oxidation stability. While pure carbon nonwovens burned down completely, within a few seconds after ignition, in LOI experiments at 80 % oxygen atmosphere, it was impossible to ignite the C/SiCON hybrid nonwovens even at 100 % oxygen (Fig. 10 c).

In summary, ceramic nonwovens were processed via electrospinning of blends of PAN and OSZ, which were converted into C and C/SiCON hybrid materials, via an optimized thermal stabilization and pyrolysis process. These nonwovens are highly flexible, foldable, and have unique properties in terms of their electrical, and thermal conductivity as well as oxidation stability. This material could thus be highly interesting for applications as an insulation material for example in high temperature furnaces or applications in smart textiles.

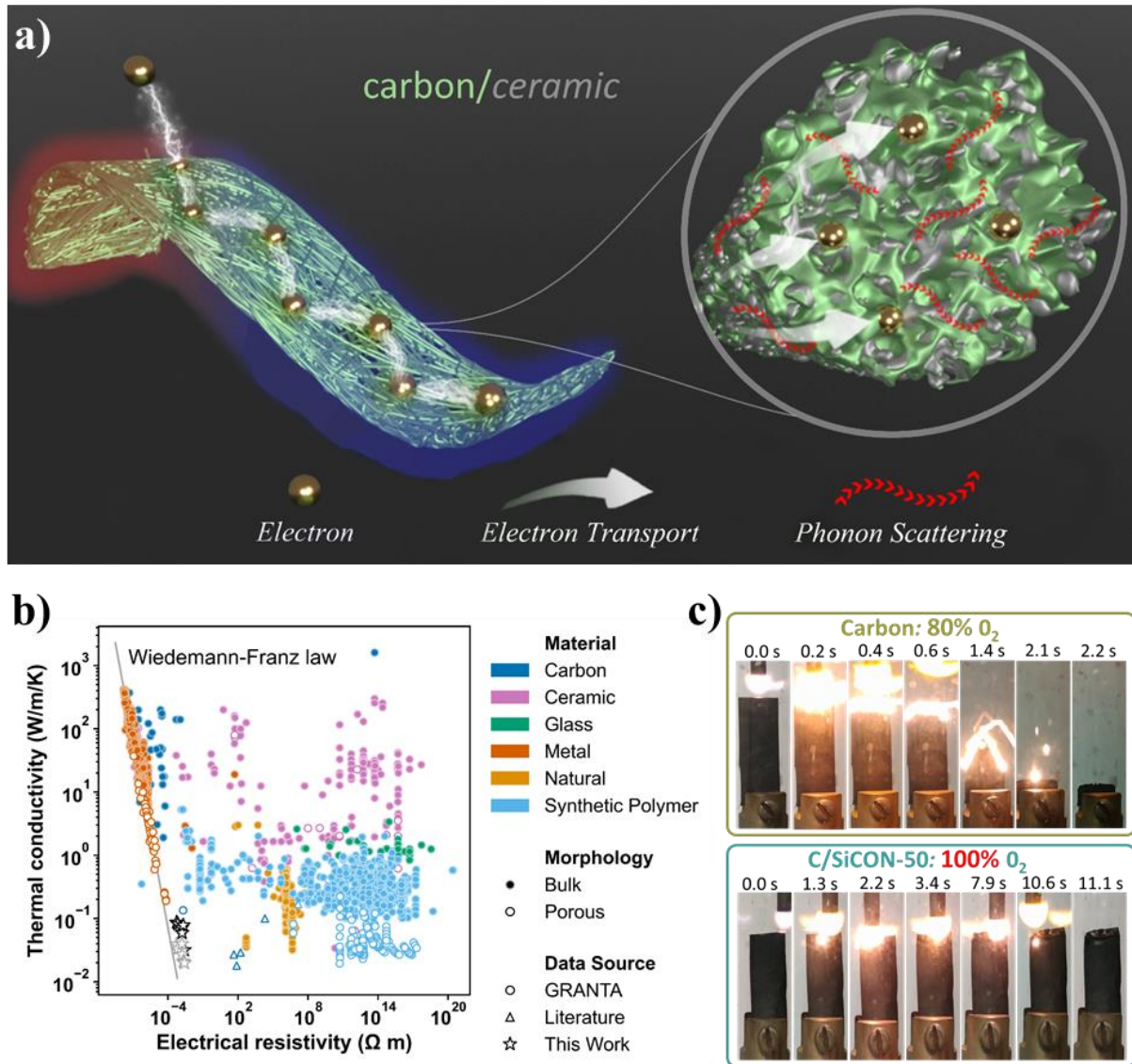


Fig. 10: a) Schematic drawing of the structure of the C/SiCON fiber web with the "sea-island" structure, which leads to high electrical conductivities due to good electron transport, but to low thermal conductivities due to phonon scattering. b) Comparison of the thermal conductivity and electrical resistivity of more than 3900 materials with the developed C/SiCON hybrid nonwovens. The grey arrow indicates the decreasing trend with increasing OSZ content. c) LOI burning experiments of pure carbon and C/SiCON-50 hybrid fibers in 80 and 100 % O₂ atmosphere.

3.2 Novel multifibrillar carbon and oxidation-stable carbon/ceramic hybrid fibers consisting of thousands of individual nanofibers with high tensile strength

In the first publication two-dimensional nonwovens were spun, which are very flexible but have no special tensile properties. Therefore, in the second part of this thesis, continuous nanofibers with high tensile strengths should be developed. The corresponding study reports on novel, continuously electrospun multifibrillar C and C/SiCON fibers consisting of thousands of single fibers in the nanometer scale. The concept behind this idea is based on Griffith's principle introduced in chapter 1. It explains the observation that brittle fibers with smaller diameters achieve higher tensile strengths. The reason is, that with smaller diameters the probability of a catastrophic failure per fiber length is reduced. In addition, the concept of the multifibrillar structure has the advantage that such a defect in one of the nanofibers only leads to a failure of an individual fiber. However, this can be easily tolerated since a bundle consists of thousands of nanofibers and the breaking of one single fiber does not represent a significant loss.

Such fibers were fabricated by a special electrospinning setup that allows spinning of continuous fibers rather than nonwovens (chapter 2.3.4). The as-spun fibers were stretched to obtain highly parallel polymer nanofiber bundles (Fig. 11 a), afterwards stabilized and pyrolyzed to multifibrillar C or C/SiCON fibers in a continuous process (Fig. 11 b). Since the tensile strengths were significantly limited by the nanofibers which were fusing together during the stabilization process, different options to reduce this effect were tested. By pre-curing the hybrid fibers with electron irradiation, the tensile strengths of the multifibrillar C/SiCON fibers were significantly improved from 400 MPa to over 700 MPa.

Since sticking could not be completely prevented and the nanofibers were partly entangled due to the spinning process, the fiber bundles had lower tensile strengths than one could expect for individual fibers. But the properties of the multifibrillar fibers are already remarkable when the low inherent weight of the multifibrillar fibers is considered. The corresponding linear density was as low as 0.33 tex (g km^{-1}) for C and 1.0 tex for C/SiCON fibers. For comparison, fiber bundles of conventional C or SiC bundles, with 3000 fibers, have linear densities of about 200 tex. In summary, this development enables the production of novel, oxidation stable C/SiCON ceramic multifibrillar nanofibers with a continuous length of several meters, suitable for upscaling to an industrial setup. The combination of high tensile strength, low weight, high oxidation stability, as well as a scalable continuous process makes these fibers a highly attractive candidate for a wide range of future applications for example as reinforcing fibers for plastics.

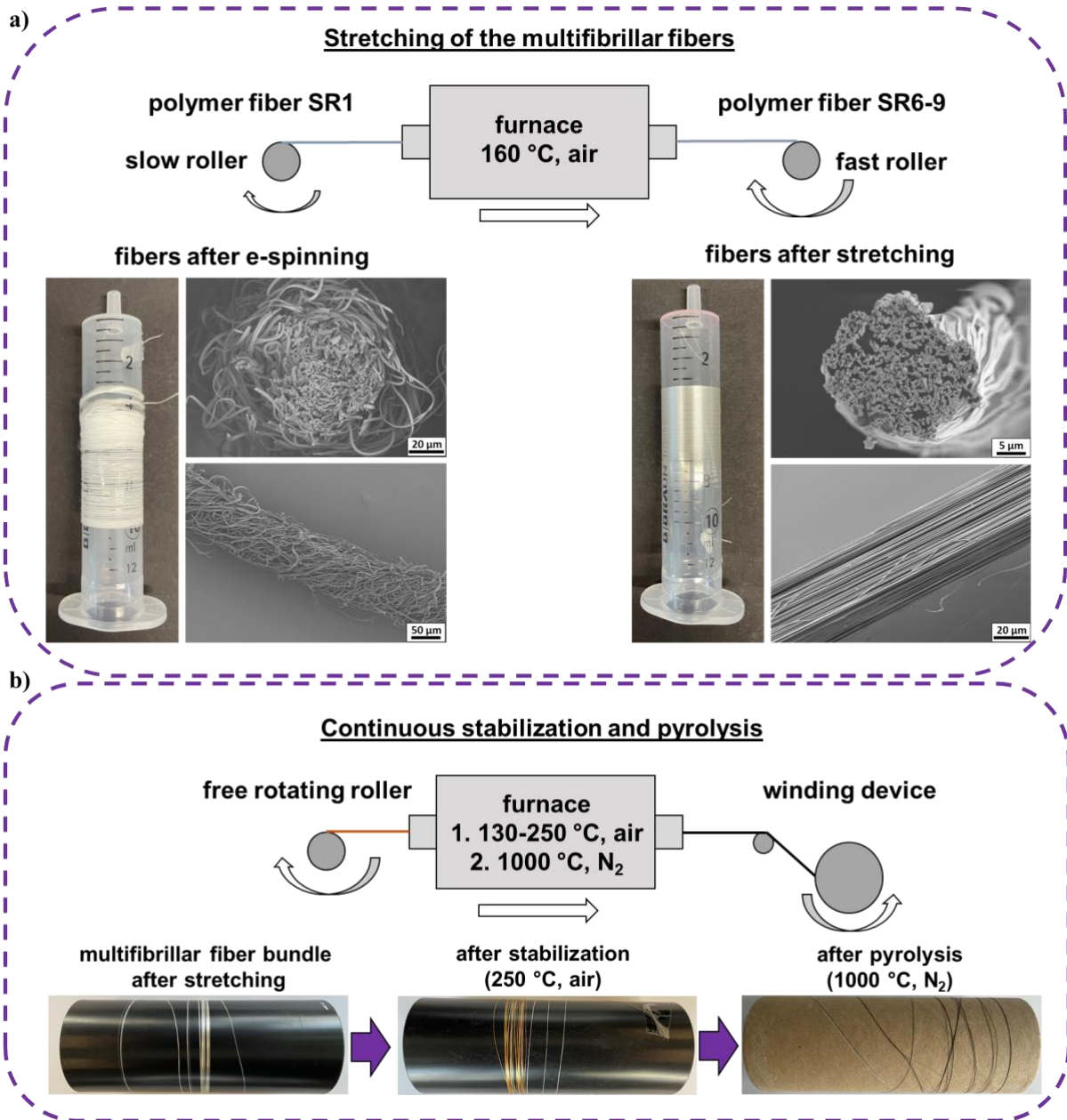


Fig. 11: a) Optical images and SEM micrographs of the stretching process of multifibrillar fibers from a disordered structure (SR1) to a highly aligned multifibrillar fiber (SR6-9). b) Continuous oxidative stabilization at 250°C in air and pyrolysis of the multifibrillar fibers at 1000 °C under N₂ atmosphere.

3.3 Synergistic enhancement of thermomechanical properties and oxidation resistance in aligned co-continuous carbon-ceramic hybrid fibers

In the third part of this thesis, thicker fibers with diameters in the small micrometer regime were developed from PAN/OSZ blends by a wet-spinning approach as discussed in Chapter 2.3.3. Since PAN cannot be melt-spun, this principle is widely used for the production of commercial carbon fibers. Therefore, it is also interesting for the material developed in this work, as this principle would be easier to transfer to a commercial set-up. Usually the precipitation medium is water, in which PAN is not soluble. However, DMF or DMSO is also added, as this slows down the solidification of the fiber surface, which leads to a rounder fiber shape and thus to better tensile properties. For the PAN/OSZ blends, the water was replaced by toluene to prevent the hydrolysis of the OSZ, which would lead to defects in the fiber. The self-made spinning set-up consisted of a syringe pump with the polymer solution of PAN, OSZ and DMF (Fig. 12 a). After the fiber was precipitated, it was drawn through a tube furnace at 150 °C by two rollers. Due to the heating, the solvents evaporate faster and the stretching of the fibers is improved, as it is heated above the glass transition temperature of PAN (~105 °C). A subsequent second stretching step allowed the fibers to be stretched at 5 – 9 times their original length. Afterwards, fiber bundles with lengths of several centimeters were stabilized at 250 °C in air and pyrolyzed at 1000 – 1500 °C in nitrogen atmosphere (Fig. 12 b-d). Since the best tensile properties were obtained at a pyrolysis temperature of 1200 °C, this temperature was used in the continuous process to pyrolyze fibers with lengths of several meters. The fibers with a diameter of 20 µm had high tensile strengths of 2.0 GPa on average and a Young's modulus of 175 GPa. Considering the simple process setup in the lab, these are excellent mechanical properties, in the same order of magnitude as commercial ceramic fibers.

The oxidation stability of the C/SiCON hybrid fibers was far superior to the pure carbon fibers is, as confirmed by TGA measurements (Fig. 12 e). For example, a 20 % mass loss was delayed by 260 °C from 573 °C to 833 °C for C/SiCON-40. In burning tests with 1200 °C gas flame, the carbon fibers already broke after 4 seconds, whereas the newly developed C/SiCON-40 fibers withstood the flame for almost 2.5 minutes (Fig. 12 f and g). Such fibers are of great interest for technical applications, since their oxidation stability is in between pure C and oxidation-stable but very expensive SiC fibers, and therefore extent the limitations in the applications of carbon fibers. Hence, the combination of these properties and the possibility to process these fibers in a continuous industrial set-up, makes this development highly relevant for real-world applications.

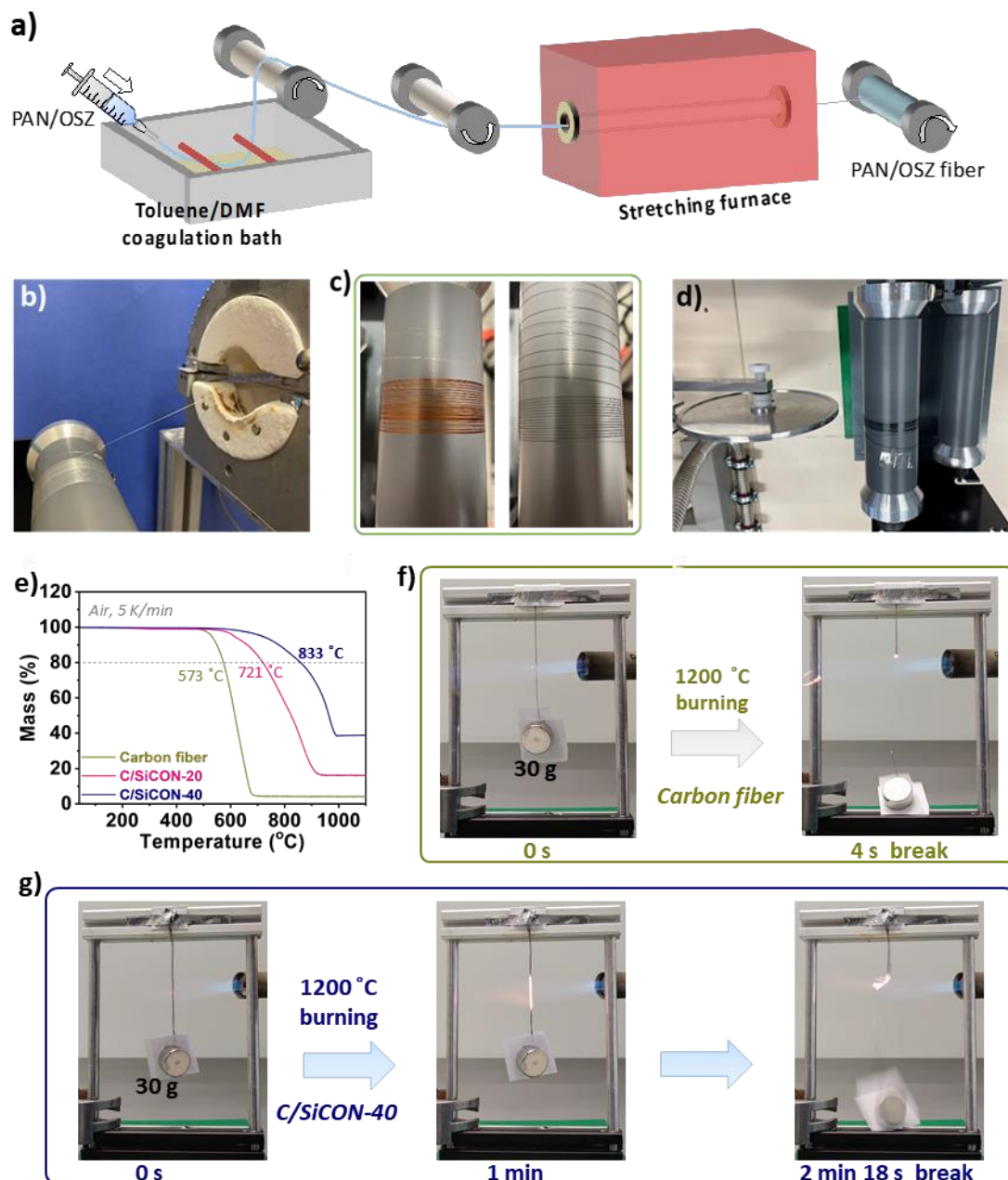


Fig. 12: a) Schematic illustration of wet-spinning a continuous PAN/OSZ hybrid fiber with a continuous stretching process. b) 8-filament PAN/OSZ hybrid fibers during the continuous stabilization process. c) Oxidized 8-filament PAN/OSZ hybrid fibers after being stabilized at 170 °C (right) and 250 °C (left). d) Collection of the 8-filament C/SiCON hybrid fibers on the reel after the continuous pyrolysis process. e) Thermogravimetric analysis of carbon and C/SiCON fibers with different content of OSZ in the polymer solution. f and g) A set of real-time images showing a 40-filament carbon fiber bundle f) and a 40-filament C/SiCON-40 fiber bundle g) exposed to a 1200 °C gas flame under tension with 30 g weight in air, respectively.

4 CONTRIBUTION TO THE PUBLICATIONS

This dissertation contains three publications, which were developed in cooperation with other scientists. In the following, the contributions of all cooperation partners to the respective publications are presented in detail.

4.1 **Extremely low thermal conductivity and high electrical conductivity of sustainable carbon-ceramic electrospun nonwoven materials**

This paper was published in the journal *Science Advances* (*Sci. Adv.* **2023**, *9*, 13).

Authors: Xiaojian Liao, Jakob Denk, Thomas Tran, Nobuyoshi Miyajima, Lothar Benker, Sabine Rosenfeldt, Stefan Schafföner, Markus Retsch, Andreas Greiner, Günter Motz, Seema Agarwal

The work on the publication was planned by Xiaojian Liao, Günter Motz, Seema Agarwal and myself. Xiaojian Liao and I fabricated the nonwovens and we both performed most of the characterizations and analyses methods such as SEM, FTIR, electrical conductivity, limited oxygen index, and burning tests. The thermal conductivity measurements were performed by Thomas Tran in the chair of Markus Retsch. Nobuyoshi Miyajima was responsible for the STEM-EDS measurements. Sabine Rosenfeldt performed the XPS measurements. The publication was written with input from all authors led by Xiaojian Liao, Seema Agarwal and Andreas Greiner.

4.2 **Novel multifibrillar carbon and oxidation stable carbon/ceramic hybrid fibers consisting of thousands of individual nanofibers with high tensile strength**

This paper was published in the journal *Scientific Reports* (*Sci. Rep.* **2024**, *14*, 18143).

Authors: Jakob Denk, Xiaojian Liao, Wolfgang Knolle, Axel Kahnt, Andreas Greiner, Stefan Schafföner, Seema Agarwal, Günter Motz

The main part of the work was conducted by myself, including the temperature treatments (stabilization and pyrolysis) and the different characterization and analysis techniques (TGA, DSC, SEM, FTIR, mechanical tests, gel tests). The RAMAN and TEM were planned by myself and performed with the help of the responsible scientific staff. Xiaojian Liao did the

electrospinning of the polymer fibers. Wolfgang Knolle and Axel Kahnt performed the electron beam treatment under my experimental planning. I wrote the first draft of the manuscript, all the authors revised it carefully and provided helpful input.

4.3 Synergistic enhancement of thermomechanical properties and oxidation resistance in aligned co-continuous carbon-ceramic hybrid fibers

This paper was published in the journal *Materials Horizons* (*Mater. Horiz.* **2024**, *11*, 5777-5785).

Authors: Jakob Denk, Xiaojian Liao, Martin Dulle, Stefan Schafföner, Stephan Förster, Andreas Greiner, Günter Motz, Seema Agarwal

The fiber preparation was conducted by Xiaojian Liao and myself together. I did most of the characterization and analysis like FTIR, SEM, fiber diameter, tensile test, TGA and DSC. The burning experiments were done by Xiaojian Liao and myself as well. TEM, RAMAN and solid state NMR measurements were planned by myself and performed with the help of the responsible scientific staff. Martin Dulle and Stephan Förster were responsible for the SAXS measurements. The writing of the manuscript was done by Xiaojian Liao and myself, all other authors revised it carefully and provided helpful input.

5 PUBLICATIONS

5.1 Extremely low thermal conductivity and high electrical conductivity of sustainable carbon-ceramic electrospun nonwoven materials

SCIENCE ADVANCES | RESEARCH ARTICLE



MATERIALS SCIENCE

Extremely low thermal conductivity and high electrical conductivity of sustainable carbon-ceramic electrospun nonwoven materials

Xiaojian Liao¹, Jakob Denk², Thomas Tran³, Nobuyoshi Miyajima⁴, Lothar Benker¹, Sabine Rosenfeldt³, Stefan Schafföner², Markus Retsch^{3*}, Andreas Greiner¹, Günter Motz^{2*}, Seema Agarwal^{5*}

Materials with an extremely low thermal and high electrical conductivity that are easy to process, foldable, and nonflammable are required for sustainable applications, notably in energy converters, miniaturized electronics, and high-temperature fuel cells. Given the inherent correlation between high thermal and high electrical conductivity, innovative design concepts that decouple phonon and electron transport are necessary. We achieved this unique combination of thermal conductivity 19.8 ± 7.8 mW/m/K (cross-plane) and 31.8 ± 11.8 mW/m/K (in-plane); electrical conductivity 4.2 S/cm in-plane in electrospun nonwovens comprising carbon as the matrix and silicon-based ceramics as nano-sized inclusions with a sea-island nanostructure. The carbon phase modulates electronic transport for high electrical conductivity, and the ceramic phase induces phonon scattering for low thermal conductivity by excessive boundary scattering. Our strategy can be used to fabricate the unique nonwoven materials for real-world applications and will inspire the design of materials made from carbon and ceramic.

INTRODUCTION

Flexible, thermally stable, and flame-resistant nonwovens with tailored low thermal conductivity and high electrical conductivity are desirable materials (1, 2). Because high thermal conductivity is proportional to high electrical conductivity, special strategies are required to invert the proportionality (3). Multiple strategies, like introducing strong anharmonicity (4), crystal complexity (5), heavy elements (6), clusters (7), entropy engineering (8), boundaries (9), size, and interface effects (10) are known for the achievement of a combination of low thermal conductivity (about 50–1000 mW/m/K) and high electrical conductivity in the materials, like dense inorganic materials, conjugated polymers, and alloys. Some low-density porous carbon materials are known to exhibit low thermal conductivity and high electrical conductivity, for example, carbon-graphene composite aerogels (11) show electrical conductivity of 2.25 S/cm and thermal conductivity of 27 mW/m/K. Otherwise, the high density and conductive graphene films/fibers (12–14), carbon nanofiber nonwovens (15, 16), and amorphous carbon (17) show high thermal conductivity (more than 10^4 mW/m/K). Meanwhile, thermal stability is another practical challenge. While carbons have excellent stability in inert environments, they degrade at around 400°C in air (18). Recently, extremely low thermal conductivity (lower than air) could be achieved in flexible

ceramic porous materials, like silica aerogels (15.9 mW/m/K) (19), hexagonal boron nitride aerogels (20 mW/m/K) (20), SiC@SiO₂ nanowire aerogel (14 mW/m/K) (21), and Si₃N₄ nanofelts (11 mW/m/K) (Ar atmosphere) (22). Because of the inherent thermal stability and extremely low thermal conductivity, these ceramic materials show excellent flame resistance and high working temperature up to 1000°C. However, because of the correlation of low thermal conductivity and low electrical conductivity, such excellent thermal insulating materials are electrically isolating, which limits their applications in high technology, like electronics, energy, etc. Thus, achieving extremely low thermal conductivity in combination with high electrical conductivity is still a major challenge for flexible materials.

We found a facile concept for the combination of extremely low thermal conductivity and high electrical conductivity together with foldability and excellent fire resistance, as shown by the schematic

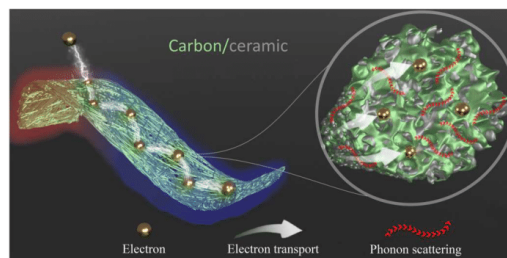


Fig. 1. A schematic of the geometry of flexible carbon-ceramic composite fibrous nonwovens with the sea-island-type structure. The carbon phase modulates electronic transport, and the ceramic phase induces phonon scattering by excessive boundary scattering.

¹Macromolecular Chemistry 2 and Bavarian Polymer Institute, University of Bayreuth, Bayreuth 95440, Germany. ²Chair of Ceramic Materials Engineering, University of Bayreuth, Bayreuth 95440, Germany. ³Physical Chemistry 1 Department of Chemistry, Bavarian Polymer Institute, Bayreuth Center for Colloids and Interfaces, Bavarian Center for Battery Technology (BayBatt), University of Bayreuth, Bayreuth 95440, Germany. ⁴Bayerisches Geoinstitut, University of Bayreuth, Bayreuth 95440, Germany. ⁵Macromolecular Chemistry 2, Bavarian Polymer Institute, Bavarian Center for Battery Technology (BayBatt), University of Bayreuth, Bayreuth 95440, Germany.

*Corresponding author. Email: agarwal@uni-bayreuth.de (S.A.); guenter.motz@uni-bayreuth.de (G.M.); markus.retsch@uni-bayreuth.de (M.R.)

illustration of electrospun carbon/silicon-based ceramic nanocomposite nonwoven materials (Fig. 1). The key for the discovery of the concept was the combination of carbon with nano-sized silicon-based ceramic inclusions in the form of a sea-island-type nanostructure (designated as C/SiCON) in the individual fibers (Fig. 1), derived from hybrid polymer materials: commercial polyacrylonitrile copolymer (PAN) and oligosilazane (OSZ) precursor (fig. S1) and the appropriate processing conditions. While PAN is used as a standard precursor for the carbon phase, the OSZ contributes to the formation of the nano-sized ceramic phase that is homogeneously distributed alongside the carbon phase in every single fiber in the form of a sea-island structure. We postulate that the increased density of interfaces between dissimilar materials (carbon and silicon-based ceramic), small pore size, and randomly laid solid fiber network structure result in the combination of extremely low thermal conductivity and high electrical conductivity.

RESULTS

The nonwovens were produced in three steps. At first, PAN/OSZ composite nonwovens were obtained by electrospinning of PAN and different amounts of OSZ. The nonwovens obtained by electrospinning were then stabilized by a step-wise temperature program or directly heating (fig. S2, A and B), from 20° to 250°C under the air atmosphere. Last, the stabilized nonwovens were carbonized and ceramized in an inert nitrogen atmosphere at 1000°C for 1 hour (fig. S2C), yielding the foldable C/SiCON composite nonwovens comparable to the printing paper (Fig. 2A). The polymer nonwovens are designated as PAN/OSZ-X, and the resulting carbonized and ceramized nonwovens are designated as C/SiCON-X, where X stands for the weight % (wt %) of OSZ relative to PAN in the electrospinning solution. Amounts ranging from 0 to 50 wt % of OSZ were investigated.

We found that the PAN fibers without OSZ had a near-circular shape with no beads and an average diameter of 900 ± 70 nm after electrospinning (fig. S3, A to C). The fiber shape and the diameter were retained after stabilization (figs. S3, A to F, and S4, A to C). The stabilization of PAN fibers by direct heating from 20° to 250°C at a heating rate of 2 K/min (fig. S2B), followed by carbonization resulted in brittle fibers. Insufficient hardening of the fibers caused melting and sticking of the fibers during carbonization, which led to a molten and brittle fibrous microstructure (fig. S5). We found that the stabilization with a step-wise temperature program from 20° to 250°C used to stabilize PAN fibers in this work was essential to avoid the melting of PAN and the fracturing of the fibers. Thus, after the carbonization of the stabilized nonwovens at 1000°C (N_2 ; fig. S2C), flexible carbon nonwovens were obtained. The carbonization of fibers caused a reduction of the fiber diameter down to 470 ± 50 nm (fig. S6) because of an increase in density and mass loss. Raman spectra show typical carbon material peaks such as the G-line (a primary in-plane vibrational mode) and the disorder-induced D-line (fig. S7). Meanwhile, XRD (x-ray diffraction) was used to investigate the crystalline reflection of the carbon fibers. Typically, a broad peak at 2θ of approximately 25° is assigned to the disordered graphitic (0002) plane, and a weak peak at 2θ of about 43° belongs to the overlapping of the (10 $\bar{1}$ 0) plane, and (10 $\bar{1}$ 1) plane diffraction (fig. S7) (23). These broad peaks were the reflexes of ill-defined or small (nano-) crystallites.

The findings on PAN were transferred to the preparation of PAN/OSZ-X nonwovens. The fibers with an average diameter in the range of 500 to 600 nm were obtained using 10 to 30 wt % of OSZ in the electrospinning solution (fig. S6). The average fiber diameter increased to 1 to 1.6 μ m when using higher amounts of OSZ (40 and 50 wt %) (figs. S6, S8, and S9). OSZs were reported to form advanced Si-based ceramics through a polymer-to-ceramic transformation at high temperatures (\sim 1000°C) in an inert gas atmosphere (24). The carbonization and ceramization of the step-wise stabilized PAN/OSZ provided foldable and resilient C/SiCON nonwovens (see reversible foldability in Fig. 2A and movie S1) with an average fiber diameter ranging from 0.34 to 1.5 μ m (fig. S6) and a porosity with a few micrometers in size (fig. S10). Compared to the obvious crease in the normal printing paper, we did not find the bold crease line in the C/SiCON nonwovens (Fig. 2A). In general, electrospinning has the advantage of modulating the mechanical properties based on the fiber diameter, which improves the foldability of the structure and can contribute to confining ceramic fillers (25, 26). This versatility makes it a useful tool for the production of flexible hybrid materials with tailored properties. Furthermore, to test the materials' fatigue resistance property, a 5000-cycle folding-unfolding test with compression strain from 10 to 99.0% was conducted (Fig. 2, B and C, and movie S2). A slight variation in work per cycle was found during this 5000-cycle folding-unfolding process, indicating that these C/SiCON-50 nonwovens have good fatigue tolerance, sufficient mechanical resilience, and foldability (Fig. 2B). The main changes in the work loss coefficient were very low and occurred in the first 10 cycles (from 1.6 down to 0.4%) (Fig. 2C). Meanwhile, after the 5000-cycle folding-unfolding test, the scanning electron microscopy (SEM) images in three perspectives (top, front, and side) revealed negligible damage to the fibers in the crease portion and bendable fibers (Fig. 2, D to I) compared to the pristine nonwovens (fig. S8, G to I).

To determine the effect of the ceramic phase on the thermal and electrical properties of the nonwovens, the thermal conductivity and electrical conductivity of the C/SiCON nonwovens with varying SiCON contents were investigated. The increase of the SiCON ceramic phase decreased the electrical conductivity gradually from 20.1 to 4.2 S/cm at room temperature (RT) measured in the in-plane direction (Fig. 3A) but did not turn it into a complete insulator, indicating that the SiCON ceramic phase did not block electron transport through the conductive carbon phase in the fibers. A light-emitting diode (LED) lamp could be lighted using our flexible C/SiCON-50 nonwoven as an electric conductor. The brightness of the LED lamp visually did not change during bending, twisting, and folding operations (fig. S11 and movie S3). Meanwhile, the electrical resistance variation was recorded during the 5000-cycle fold-unfolding testing (movie S2). The C/SiCON-50 nonwovens revealed a negligible change in the electric conductivity after folding-unfolding 5000 times, represented by the electrical resistance variation (R/R_0) of 1.01 (fig. S12). Moreover, we found that the electric conductivity increased slightly with increasing temperature from -50° to 300° C, which is known for semiconducting graphitic materials derived from pyrolyzed PAN and suggests our materials have a broad range of working temperatures (Fig. 3A). The thermal conductivity of the nonwoven was investigated along two distinct orientations: along (in-plane) and perpendicular (cross-plane) to the fiber orientation. We used lock-in thermography (LIT) for the in-plane transport, and light flash analysis (LFA)

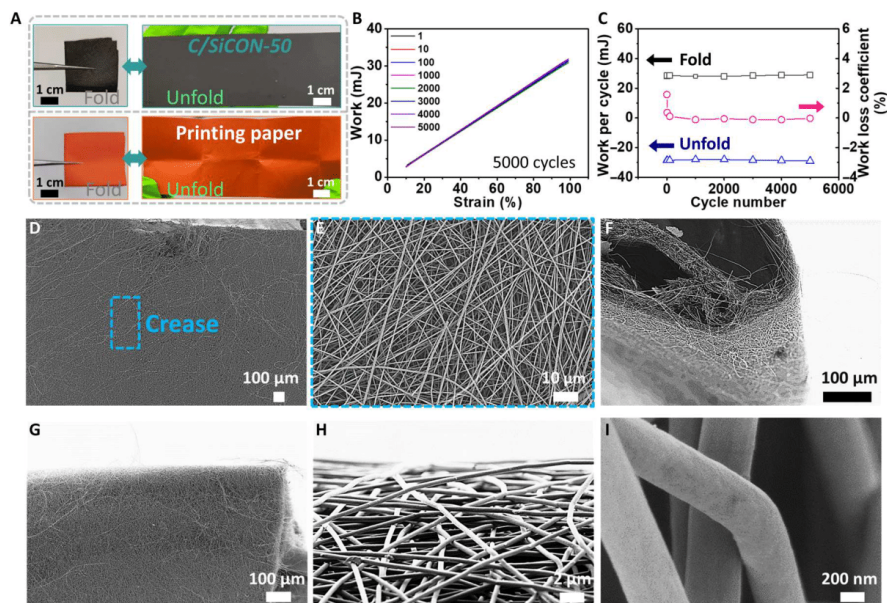


Fig. 2. Robust and foldable C/SiCON-50 nonwovens. (A) Digital images of C/SiCON-50 nonwoven showing the foldability of the material. The nonwoven can maintain its structure after being folded. The normal printing paper was used as a contrast test. (B) Work versus fold strain during a 5000-cycle folding-unfolding test with folding strain from 10 to 99%. (C) Changes of work and work loss coefficient per cycle with different cycle numbers during the 5000-cycle fold-unfolding test. (D to I) SEM images at three different angles of C/SiCON-50 nonwovens after the 5000-cycle fold-unfolding test in different magnifications. Top view of the surface images of unfolded nonwovens (D and E). It shows that a negligible amount of fibers in the membrane is broken. Side view (F) and front view (G) of flexible C/SiCON-50 nonwovens in a folded state. Images of deformed surfaces in high magnification (H and I).

and transient plane source (TPS) characterization for the cross-plane transport (Fig. 3, B to E, and figs. S13 and S14). LIT and LFA determine the thermal diffusivity, from which the thermal conductivity is calculated by $\kappa = \alpha \cdot \rho \cdot c_p$, with κ being the thermal conductivity, α being the thermal diffusivity, ρ being the effective density, and c_p being the specific heat capacity. Increasing SiCON marginally raised the heat capacity, while the effective density of the nonwovens remained constant (about 100 mg/cm^3) (figs. S13 and S14, A and B). The thermal diffusivity showed a clear falling trend with increasing SiCON content, particularly for the cross-plane thermal diffusivity (fig. S14, C and D). As a result, also the in-plane thermal conductivity decreased with increasing SiCON. We obtained the lowest in-plane thermal conductivity for C/SiCON-50 nonwovens ($32 \pm 12 \text{ mW/m/K}$), being well in the range of state-of-the-art polymer foams. The in-plane thermal transport measurements were performed in vacuum ($<10^{-2}$ mbar). A similar decreasing trend of thermal conductivity was also observed in the cross-plane direction, which was all conducted under ambient conditions. First, the cross-plane thermal conductivity of C/SiCON-X nonwovens was measured via TPS. The minimum value was obtained for the C/SiCON-50 nonwovens with $10 \pm 0.1 \text{ mW/m/K}$ (in air, RT). Furthermore, LFA was used to confirm the cross-plane thermal conductivity. Although higher thermal conductivity values were recorded, like $19.8 \pm 7.8 \text{ mW/m/K}$

in the C/SiCON-50 nonwovens (in air, RT), it clearly showed the same trend as TPS: The higher content of SiCON, the lower cross-plane thermal conductivity. The lower thermal conductivity in the case of the TPS measurement can be attributed to an additional interfacial resistance between the measurement sensor and the nonwoven sample surface. Regardless, both cross-plane thermal conductivity values of C/SiCON-50 nonwovens are extremely low (thermal conductivity of air = 26 mW/m/K). Although the nonwovens constitute an open porous structure, heat transport via the gas phase apparently does not substantially add to the heat transport of these fibrous skeletons.

We highlight the unique combination of extremely low thermal conductivity and high electrical conductivity of our C/SiCON nonwovens by an Ashby plot (Fig. 3F) compared to more than 3900 materials of all types, including carbons, ceramics, natural materials, synthetic polymers, metals, glasses, and their composites in the formation of bulk or porous. Our C/SiCON nonwovens populate an empty space in quadrant b, where strong thermal insulation is combined with a low electric resistivity. This behavior could seemingly be expected when extrapolating the thermal conductivity and electrical conductivity of metals (orange) and carbonaceous (blue) materials; however, for ceramic materials, this property combination is quite remarkable. Moreover, our robust and foldable C/SiCON

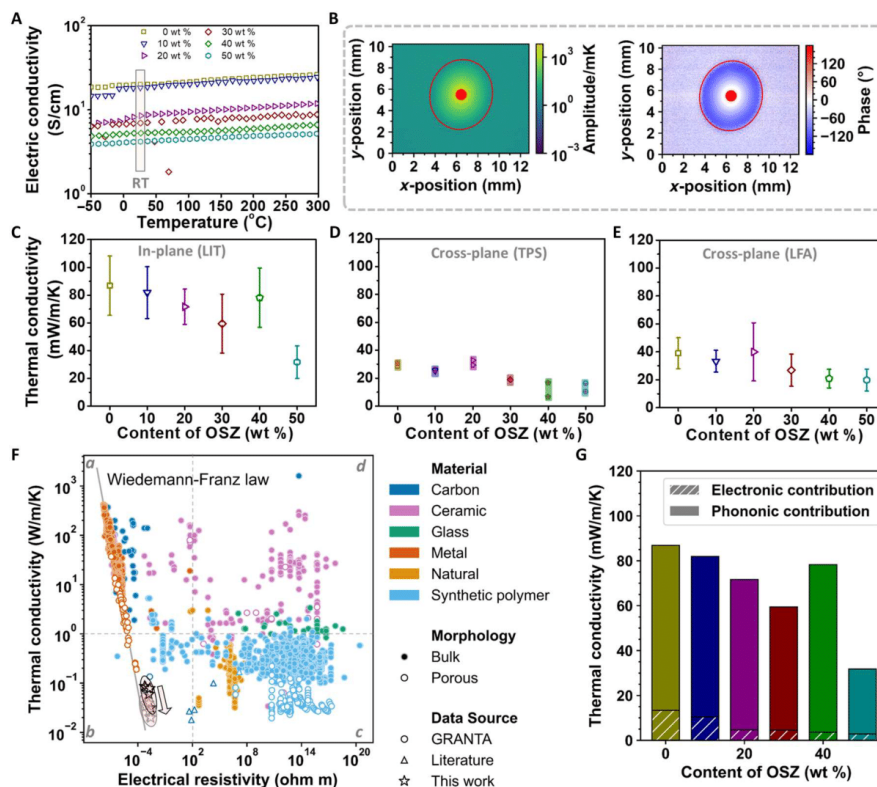


Fig. 3. Thermal and electrical properties of the C/SiCON nonwovens. (A) Temperature-dependent electrical conductivity of the C/SiCON-X nonwovens derived from PAN with different contents of OSZ. The measurements were conducted with the van der Pauw method. The marked area shows the RT electrical conductivity of the C/SiCON-X nonwovens versus the OSZ content. (B) LIT data for a C/SiCON-50 nonwoven. The excitation frequency is 0.5 Hz. After 40-s equilibration time, the sample was measured for 100 s. The resulting amplitude and phase were calculated using direct Fourier transformation. For the diffusivity evaluation, data along the two principal axes of the ellipse are taken into account. (C) In-plane thermal conductivity of the C/SiCON-X nonwovens derived from PAN with different contents of OSZ. Samples were measured with LIT. (D and E) Cross-plane thermal conductivity of the C/SiCON-X nonwovens derived from PAN with different contents of OSZ. (D) is measured via TPS, and (E) is measured via LFA. (F) Comparison of the thermal conductivity and electrical resistivity for C/SiCON-X nonwovens (in-plane thermal conductivity marked by black stars and cross-plane thermal conductivity marked by gray stars) and more than 3900 materials of all types in the Ansys Granta Selector database (www.grantadesign.com, date: 30 September 2021) and additional literature. The data of additional literature in this Ashby plot are shown in table S2. The arrow beside our work shows the decreasing trend of thermal conductivity as SiCON content increases. (G) Electronic and phononic contributions to the overall in-plane thermal conductivity of the C/SiCON-X nonwovens derived from PAN with different contents of OSZ. Samples were measured with LIT.

nonwovens are scalable as electrospinning is a continuous and industrialized production method for nonwovens.

Analyzing the electronic and phononic contributions to the overall thermal conductivity, we find that the electronic contribution is low and decreases with increasing OSZ content (Fig. 3G). Note that the exact electronic contribution strongly depends on the Lorenz number used for the calculation of the Wiedemann-Franz law. The Lorenz number has been reported to range between 2.45×10^{-8} and $4.60 \times 10^{-8} \text{ W}\Omega\text{K}^{-2}$ for graphitic materials (27). The calculation of the electronic contribution in Fig. 3G indicates the minimum electronic contribution.

On the basis of our findings, we hypothesize that the sea-island-type structure, consisting of electrically conductive carbon as the matrix and a large number of phase boundaries owing to the dispersed thermally insulating SiCON inclusions (Fig. 1), resulted in nonwovens with the combination of extremely low thermal conductivity and high electrical conductivity. A pure carbon nonwoven alone is not suitable to reach an extremely low thermal conductivity rivaling the thermal insulation of air. ATR-FTIR (attenuated total reflectance-Fourier transform infrared spectroscopy) demonstrated overlapping signals of the Si-O-Si, Si-N, and Si-C (987 cm^{-1}) belonging to the SiCON phase and the typical C=C (1500 cm^{-1}) carbon phase (Fig. 4A and fig. S15). Evidently, during the solid

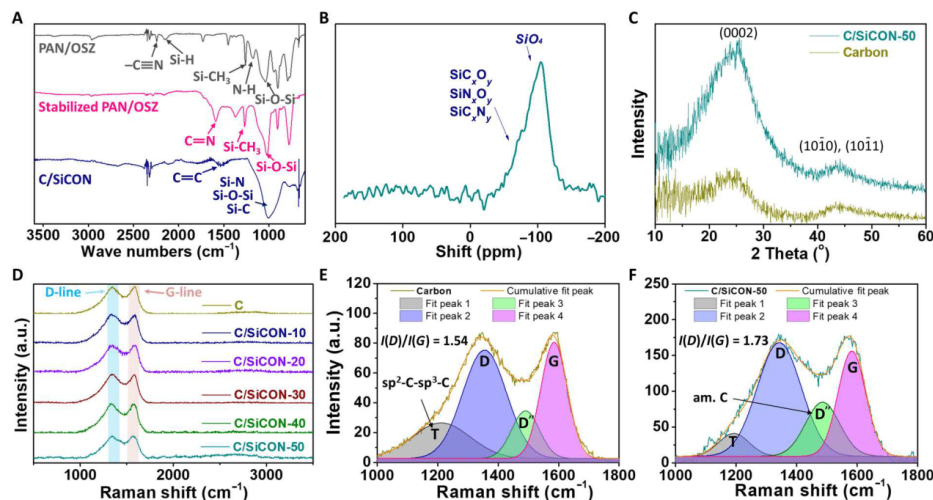


Fig. 4. Analysis of the carbon and C/SiCON fibers. (A) ATR-FTIR spectra of the polymer, stabilized, and carbonized/ceramized nonwovens from PAN with 40 wt % OSZ. (B) Solid ^{29}Si -NMR spectra of C/SiCON-50 nonwovens. (C) XRD analysis of the pure carbon and C/SiCON-50 nonwovens. The (10 $\bar{1}$ 0) plane, and (10 $\bar{1}$ 1) plane reflexes overlap at 2θ near 43° . Table S3 shows the information on the nanocrystallites based on the XRD analysis. (D) Raman spectra of the pure carbon and C/SiCON nonwovens. (E and F) Curves fitted in Raman spectra of carbon fiber (E) and C/SiCON-50 (F) with a Gaussian function. The area values of (D) and (G) peaks were used to calculate the ratio of $I(\text{D})/I(\text{G})$. a.u., arbitrary units.

^{29}Si -NMR [Si-29 nuclear magnetic resonance (NMR)] spectroscopy, a distinct SiO_4 signal at -104 ppm (parts per million) was found. A broad peak in the -50 to -90 ppm region was characteristic for complex, mixed SiC_xO_y , SiN_xO_y , and SiC_xN_y environments (Fig. 4B). It indicated that the SiCON phase had been incorporated into the carbon phase. However, the addition of the SiCON phase did not result in substantial changes in XRD and Raman spectra, which we explain by overlapping broad peaks of the nano-crystalline reflexes of the carbon phase (Fig. 4, C to F). Compared to the pure carbon fibers, C/SiCON-50 fibers had a higher intensity ratio of the D band and G band [$I(\text{D})/I(\text{G})$] in the Raman spectra (Fig. 4, E and F), which indicates a higher disordering of the carbon phase and lower graphite content in the C/SiCON-50 fibers. The higher disordering carbon phase can complicate and extend the electron transport path and arouse additional scattering, which results in a decrease in the electrical conductivity and thermal conductivity. In addition, both $d(0002)$ interplanar spacing and the size of nanocrystallites in L_a (crystallite lateral size) and L_c (crystallite thickness) of graphitic carbon in C/SiCON-50 fiber were smaller than that of pure carbon fibers (table S3). Further investigation from the selected area electron diffraction pattern with three Debye-Scherrer rings in the cross-sectional TEM (transmission electron microscope) image of C/SiCON-50 fiber (Fig. 5, A to C) confirmed the graphitic (0002), (10 $\bar{1}$ 1) planes observed in the XRD spectra, and additional (11 $\bar{2}$) and/or (11 $\bar{2}$ 0) planes (d -spacing is about 0.12 nm, corresponding to the 2θ of approximately 78° in XRD spectra), while it also indicated a nano-crystalline structure in the C/SiCON-50 nonwovens. Furthermore, elemental analysis and XPS (x-ray photoelectron spectroscopy) investigated the elemental composition (table S4 and fig. S16). We observed that following stabilization and carbonization/

ceramization of PAN/OSZ-50 nonwovens, the concentration of O and Si increased, whereas the quantity of N decreased, and the one of C remained constant (table S4). XPS surface survey of C/SiCON-50 fiber revealed an atomic ratio of Si species of 17.6 (equal to 29.4 wt %) (fig. S16), which is accompanied by a lower ratio of C species compared to the elemental analysis (table S4). Hence, a slight decrease of C at the surface of the fiber can be assumed for the C/SiCON-50 sample. Together, our analyses strongly indicate that carbon and SiCON were incorporated into the C/SiCON fibers by electrospinning, stabilization, and carbonization/ceramization. Furthermore, STEM-EDS (scanning transmission electron microscopy-energy-dispersive x-ray spectroscopy) spectroscopy was used to profoundly investigate the distribution and combination of elements inside the fibers (Fig. 5, D to H, and figs. S17 and S18). A high-resolution HAADF (high-angle annular dark-field) cross section of a C/SiCON-50 fiber depicted bright blocks (heavy element, here Si) emerging from the dark or a gray area (light element, here C), similar to numerous islands distributed homogeneously in the sea (Fig. 5I) without the agglomeration of big blocks. The EDS mapping images show two dominant components: C-bearing matrix (C-C or C-N) and Si-bearing inclusions (Si-O, Si-C, and Si-N) (Fig. 5, D to H), consistent with the above results. We can see that the SiCON phase is distributed homogeneously within the carbon phase. This is also supported by the C/SiCON fibers with different contents of SiCON ceramic (C/SiCON-10 and C/SiCON-30; figs. S17 and S18), with a decrease in the sizes of the dispersed domains. All these results show that both carbon and SiCON phases are distributed homogeneously in the fiber with the formation of a sea-island nanostructure (26). On the basis of the two-dimensional slice through the fiber, we cannot

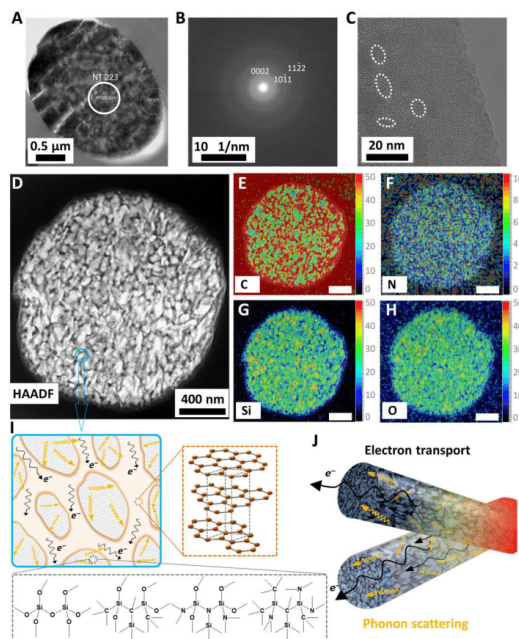


Fig. 5. Nanostructure and elemental distribution of the C/SiCON fiber and the proposed model of thermal and electrical properties analysis. (A) TEM cross-sectional image of C/SiCON-50 fiber. (B) Selected area electron diffraction pattern (the position indicated the NT223 circle in the insert TEM cross-sectional image of C/SiCON-50 fiber) with three Debye rings originated from three strong (0002), (10 $\bar{1}$ 1), and (11 $\bar{2}$ 2) planes in the graphite-like structure (with sp² and sp³ bonds). (C) High-resolution TEM micrographs of the cross section of the fiber. The marked areas show the basic structure of the nanocrystallites in the free carbon nanodomains. (D to H) High-resolution HAADF-STEM cross-sectional image (D) and EDS mapping (weight %) images (E to H) showing the cross section of a single C/SiCON-50 fiber. Note that the dominant components are C-bearing matrix (C-C or C-N) and Si-bearing inclusions (Si-O, Si-C, and Si-N) (dark and bright on HAADF-STEM image, respectively). Scale bars, 400 nm. (I) Schematic illustration of the sea-island nanostructure. (J) Schematic illustration of the electrical and thermal transport of C/SiCON fibers.

discriminate between nanoparticulate inclusions inside the carbon matrix or the formation of a sponge-like co-continuous structure. In both cases, however, a high amount of interfaces can be expected inside the C/SiCON nanocomposite fibers. These interfaces, in combination with constriction resistances at the fiber-fiber contact points (fig. S9), lead to the unique combination of electric conductivity and thermal insulation.

The major achievement of this nanocomposite is that the increasing ceramic phase is not strongly increasing the electrical resistance and that the ceramic inclusions do not increase the phononic heat transport (Fig. 5). The uniformly dispersed SiCON phase introduces phonon boundary scattering within the carbon matrix (Fig. 5, I and J), resulting in a reduction in phononic thermal conductivity. This mechanism is also supported by the fact that a higher content of SiCON phase lowers the thermal conductivity (Fig. 3, C

to F). Consequently, the C/SiCON nonwovens demonstrate optimum thermal insulation combined with an electrical conductivity close to the highest possible value as indicated by the extrapolated Wiedemann-Franz law (Fig. 3G). We attribute this unique combination to the intricate nanostructuring inside the C/SiCON fibers, where the presence of interfaces attenuates the phononic thermal transport of the ceramic parts, without impeding the electronic transport that is confined to the graphitic phase.

Besides achieving the combination of extremely low thermal conductivity and high electrical conductivity, we also found that the C/SiCON nonwovens are nonflammable and thermally very stable (Fig. 6). The initial results showed that the pure carbon nonwoven could be easily ignited and burned out as the oxygen content is up to 80%, while the C/SiCON-50 nonwovens withstand and maintain the fiber form even at 100% O₂ atmosphere in LOI (limiting oxygen index) tests (Fig. 6, A to C, and movie S4). As shown in the SEM images of both materials after LOI testing, the pure carbon fibers were burned into carbon dust with a block formation (fig. S19, A to D), while the C/SiCON-50 can remain in the fiber form with a melted state (fig. S19, E to H). Furthermore, the SEM-EDS surveys of both specimens were performed to investigate the element's content (fig. S20). The carbon dust consists of carbon and oxygen with a weight ratio of 1:1. A clear increase of Si and O content (up to 43 and 46.5 wt %, respectively) and a decrease in C content (decrease to 10.4 wt %) were observed in the C/SiCON-50 nonwovens. On the basis of the above finding, we postulate that the homogeneously distributed SiCON ceramic phase can remain and form a passivating silica layer on the surface after the surface carbon burn out, which can protect the fibers very effectively against further oxidation during the LOI testing. Our materials with outstanding fire resistance (LOI values of 100) are better than most polymers and carbon materials and are comparable to commercial ceramic materials, such as SiC, Al₂O₃, and SiO₂ (fig. S21). In addition, a methane burner burning experiment in air (~800°C, 5 min) was conducted (Fig. 6, D to F, and movie S5). The carbon nonwovens were oxidized entirely, leaving no fiber residue (Fig. 6D). Whereas C/SiCON-10 and C/SiCON-50 nonwovens neither burnt nor showed any dripping and shape deformation (Fig. 6, E and F). Because the materials maintained their structural integrity, it makes them safer during fire hazards than pure carbon materials. After burning at 800°C for 5 min, the thermal conductivity and electrical conductivity of C/SiCON-50 nonwovens were also tested. The thermal conductivity remains at the extremely low value of about 16.6 mW/m/K (cross-plane), while the electrical conductivity drops to 0.02 S/cm due to a 36 wt % loss of carbon phase (fig. S22). This low electrical conductivity is still in the range of semiconductors. In the future, other concepts are required to maintain structural integrity during burning at higher temperatures and longer time while maintaining high electrical conductivity. This might require replacing carbon with other appropriate materials and making innovative phase-separated structures.

DISCUSSION

A combination of extremely low thermal conductivity and high electrical conductivity was achieved by combining the SiCON ceramic phase and the carbon phase in electrospun fibers with a sea-island-type nanostructure. This enabled the simultaneous optimization of electron and phonon transport in the fibers. Thus, the

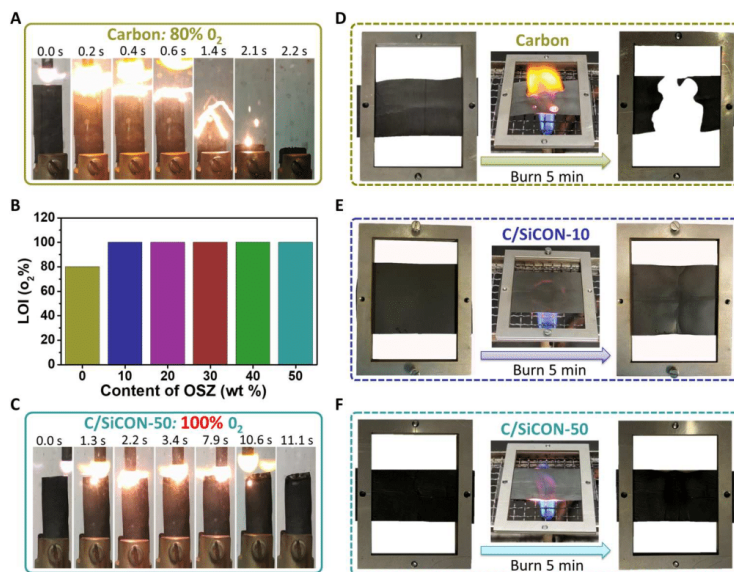


Fig. 6. Flame resistant and thermal stability of C/SiCON nonwovens. (A) A set of real-time images showing the process of the LOI test on pure carbon nonwovens under 80% O₂ atmosphere. (B) LOI values of the carbon nonwovens and C/SiCON nonwovens derived from PAN with different contents of OSZ. (C) A set of real-time images showing the process of the LOI test on C/SiCON-50 nonwovens under 100% O₂ atmosphere. (D to F) Digital photos of carbon nonwovens (D), C/SiCON-10 nonwovens (E), and C/SiCON-50 nonwovens (F) before and after burning with a methane burner at about 800°C for 5 min in air.

electronic transport inside the carbon matrix phase could be retained without adding to thermal transport by phonon scattering at the SiCON ceramic interfaces. We are convinced that our underlying principle to combine dissimilar phases in the fibers to optimize phonon and electron transport is not just limited to the present system. The unique multifunctional properties of this textile-like material combine the best properties of various material classes, such as polymer-foam rivaling thermal insulation, ceramic-like fire retardance and nonflammability, and high electric conductivity. We are convinced that such materials with multifunctional properties would open up several application areas and tackle present bottlenecks for applications in the field of energy management, smart textiles, electromobility, or aerospace.

MATERIALS AND METHODS

Materials

PAN was obtained from Dolan GmbH (Germany) and used as received [copolymer with maximum 8% methyl acrylate and methylsulfonate according to the datasheet from Dolan GmbH; number average molar mass (M_n) = 95,000 g/mol; registration no. 26658-88-8]. OSZ Durazane 1800 was obtained from Merck (Germany) and used as received. Dicumylperoxide (DCP) was obtained from Sigma-Aldrich (Germany) and used as received. *N,N'*-dimethylformamide (DMF; 99.99%) and 99.9% acetone were obtained from Thermo Fisher Scientific GmbH (Germany) and used as received. The normal printing paper was Orange Label print paper from

Canon, A4, 80 g/m² (<https://staples.de/orange-label-performance-papier-a4-80-g-m2-weiss/364513/>).

Electrospinning

The solution (~15 wt %) for electrospinning was prepared by dissolving PAN powder and Durazane 1800 (with 3 wt % of DCP) in DMF. After dissolving for 12 hours with a stirring speed of 500 rpm, acetone was added to the solution and stirred for another 2 hours at a speed of 500 rpm. The compositions of the solutions can be seen below in table S1.

The electrospun nonwovens were fabricated using a homemade setup with a syringe pump, a high-voltage direct-current power supply, and a rotary collector covered with aluminum foil. The solution was loaded into a syringe capped with a metal needle (diameter of 0.8 mm) connected with the high voltage. The polymer solution was pumped at a feed rate of about 0.8 ml/hour. The distance between the metal needle and collector was set at about 25 cm. After high voltage (+17 kV) was applied, polymer fibers were collected at the collector with a speed of 100 rpm and a diameter of about 10 cm for about 1.5 hours. The whole electrospinning process was conducted at RT and humidity of about 20%. Last, the polymer nonwovens were obtained after drying in a vacuum oven at 50°C for 48 hours.

Stabilization process

The stabilization process was performed under air in a high-temperature clean room oven chamber furnace (Carbolite Gero, Germany). The polymer nonwovens were covered with graphite

foil. A step-wise temperature program from 20° to 250°C with a heating rate of 2 K/min was used (fig. S2A). At 130°, 150°, 170°, 190°, 210°, 230°, and 250°C, the temperature was held for 1 hour each. The airflow rate was 4 liters/min. After cooling to RT by passive cooling within 1 day, the oxidized samples were obtained.

The control experiments were conducted by preparing carbon nonwovens. The PAN nonwovens were stabilized by heating from 20° to 250°C with a heating rate of 2 K/min and held at 250°C for 1 hour in the air (fig. S2B), and the airflow rate was 4 liters/min. After cooling down to RT by passive cooling within 1 day, the oxidized samples were obtained.

Carbonization and ceramization process

The stabilized nonwovens were cut into strips with a length of 200 mm and a width of 50 mm. Each strip was covered with graphite foil and stacked layer by layer on the quartz glass board. The carbonization and ceramization process was performed in a FA100-500/13 tube oven furnace (Carbolite Gero, Germany) under a nitrogen atmosphere. The quartz glass board with samples was pushed into the heat zone position of tube oven from one side of the tube oven under the nitrogen atmosphere with N₂ flow rate of 2 liters/min. After loading the samples and sealing the tube, the N₂ flow rate was set to 150 ml/min. Then, samples were heated with different heating rates from 20° to 1000°C (fig. S2C): A slow heating rate of 1.25 K/min was used during RT to 100°C segment to flush out the oxygen contamination; a faster heating range with 2 K/min was used during 100° to 300°C segment and 700° to 1000°C segment; and during 300° to 700°C segment, a slower heating range of 1 K/min was set to ensure that the material has enough time for the carbonization and ceramization reactions to carbon and SiCNO ceramics. The holding time of 1 hour at 1000°C was used to complete the transformation of the material. Afterward, the furnace was cooled down to RT by passive cooling (without heating and natural cooling) within 1 day, the final materials in the quartz glass board were removed from the tube oven.

Scanning electron microscopy

The SEM images of the nonwovens were acquired by the Zeiss LEO 1530 (Gemini, Germany) scanning electron microscope equipped with a field emission cathode and a secondary electron (SE2) and an InLens detector. An acceleration voltage of 3 kV and a working distance between 5 and 6 mm were used. Before the measurement, the nonwoven samples were cut into small pieces and attached to a sample holder with conductive double-sided tape. The samples were subsequently sputter-coated with a 2.0-nm platinum layer by a Cressington 208HR high-resolution sputter coater, equipped with a quartz crystal microbalance thickness controller (MTM-20). From 50-diameter measurements with the software ImageJ, an average value and the standard deviation of the fiber diameter were calculated.

Folding-unfolding test

The 5000-cycle folding tests with compression strain from 10 to 99.0% were conducted to test materials' fatigue resistance property. The sequential fold cycles were performed by the tensile tester (zwickiLine Z0.5, BT1-FR0.5TN.D14, Zwick/Roell, Germany) with a clamping length of 10 mm and a 20 N load cell (Zwick/Roell KAF TC). The samples were loaded between the two clamp stages with the top clamp stage applying uniaxial tension on the

samples along the vertical direction. Meanwhile, a multimeter was connected to materials via copper conductors to record the electrical resistance during the folding test (movie S2). All curves were obtained at the strain ramp rate of 200 mm/min. The test time, cycle number, stress, stain, and the work per cycle were recorded. The work loss coefficient is calculated as the ratio of the work difference between the folding and unfolding of the each cycle to the folding work. After the 5000-cycle test, the samples were cut out from the specimen after suffering the 5000-cycle test with a scissor and used for SEM measurement. For the nonwoven sample's side view of SEM, the nonwoven sample was maintained in a folded and vertical state in an SEM cross section using the accompanied screw. For the nonwoven sample's front view of SEM, an unfolded nonwoven sample was attached to a conductive double-sided tape. All of the SEM measurements were carried out in the same way as the previous SEM measurements.

ATR-FTIR spectroscopy

The ATR-FTIR studies were performed on a Tensor 27 system (Bruker, Germany) equipped with an ATR unit with a diamond crystal. After a background measurement, the nonwovens were cut into small pieces (about 5 mm by 5 mm) and pressed against the measuring diamond to receive a good signal. The measurements took place in a wave number range of 4000 to 400 cm⁻¹ at a resolution of 5 cm⁻¹. Thirty two measurements were averaged per sample to obtain higher signal-to-noise ratios. After the measurement, a baseline correction by the ATR-FTIR software (OPUS) was performed, and the measured data were saved as a .CSV file and plotted graphically using the Origin software.

X-ray diffraction

XRD characterization was carried out using an anode x-ray generator (Bruker D8 ADVANCE, Karlsruhe, Germany) operating at 40 kV and 40 mA with Cu-K_α radiation (wavelength $\lambda = 0.154$ nm). Before the measurement, the nonwovens were fixed in a metal frame, and then the whole frame was installed in the instrument stage. XRD profiles were recorded in the 2 θ angle range from 5° to 60° at a scanning speed of 0.05°/min at 25°C in transmission mode. The background was recorded by measuring an empty metal frame. The acquired XRD curves were analyzed by DIFFRA-C.EVA V4.0 software, while the final spectra were obtained by background subtraction.

Raman

A combined Raman Imaging/Scanning Force Microscope System (WITec alpha 300 RA+, Germany) with WiTec Control FIVE 5.3 software was used for RAMAN measurements. Laser is equipped with a UHTS 300 spectrometer combined with a back-illuminated Andor Newton 970 electron multiplying charge-coupled device camera [resolution: ca. 300 to 400 nm (lateral) and 900 nm (z) with 100 \times objective].

The measurements were carried out at an excitation wavelength of $\lambda = 532$ nm and a laser power of 1 mW with 50 accumulations with an integration time of 0.5 s pixel⁻¹. The samples were stacked on a glass slide. After adjusting the focus on the nonwovens at $\times 100$ magnification, the Raman spectrum was recorded. A cosmic ray removal and a baseline correction were performed on all spectra. The peaks were then fitted with a Gaussian function using the built in routine of Origin 2016.

Downloaded from https://www.science.org at Universitaet Bayreuth on April 03, 2023

Thermal conductivity

Thermal conductivity was measured with three different methods: LIT, LFA, and TPS. Conductivity values during the LIT and LFA were calculated by $\kappa = \alpha \cdot \rho \cdot c_p$, with α being the thermal diffusivity, ρ being the effective density, and c_p being the specific heat capacity. The details are described in the following parts.

Thermal conductivity by TPS method

The thermal conductivity measurements were performed by the TPS method on a Hot Disk Thermal Constants Analyser (TPS 2500 S, thermal conductivity range: 0.005 to 1800 W/m/K, reproducibility: thermal conductivity $\pm 3\%$, Hot Disk, Sweden) with a Kapton 7854 sensor operating with the thin-film module (thickness range: 20 to 600 μm) method at a constant temperature of 22°C controlled by air condition. The "Hot Disk Thermal Constants Analyser 7.4.15" software was used for the evaluation.

Before the measurement, two 30 mm by 30 mm squares were cut out of the sample. Each square's thickness was measured with a digital micrometer at five points, corresponding to five cube eyes, and the average thickness was determined from the numerical mean value as the measurement parameter. The Kapton sensor (design 7854, radius = 10.5 mm) was placed centrally between the two square samples and placed in the measurement apparatus "slab sample holder" (Hot Disk Thermal Constants Analyser, Instruction Manual, Revision date 8 2019 October). The sensor in the sample sandwich was weighted with the upper parts of the slab sampler holder (a total mass of 304 g) and the additional stainless steel weights of 630 g (according to the stainless steel verification samples of the TPS 2500 S). The measuring thermometer with PT100 resistance was placed directly next to the measuring module, and the measuring arrangement was closed with the protective cover.

Before each series of measurements, the background thermal conductivity was measured once a day as a reference measurement. This reference measurement was carried out with a heating power of 750 mW and a measuring time of 20 s resulting in a thermal conductivity of 28.8 mW/m/K of the Kapton sensor and 14.9 W/m/K of the slab sample holder stack, respectively. After 1 hour, sample measurement was conducted five times with interval time at 1 hour. On the basis of the same background thermal conductivity, the sample measurements were carried out with heating power at 450 mW and measuring time at 20 s, so that all sample measurement results, including background thermal conductivity, background thermal diffusivity, background specific heat, probing depth, temperature increase, total to characteristic time, total temperature increase, and mean deviation, were within the parameter limits of the evaluation software.

Thermal diffusivity

Cross-plane thermal diffusivity was measured via LFA (Netzsch LFA 467 HT HyperFlash). Samples were cut in cylinders with 10 mm in diameter. Height was determined via laser microscopy as described below (see the "Effective density" section). Measurements were done under ambient conditions. The pulse width was set to 100 μs , lamp voltage to 230 V, and acquisition time to 50 ms. The data were fitted by a penetration model with Netzsch' Proteus software. For each OSZ content, three samples were measured.

In-plane thermal diffusivity was measured via LIT using an improved version of our custom setup (28). Samples were cut in rectangles with a size of approximately 25 mm by 25 mm. They were put into a vacuum chamber ($P < 10^{-2}$ mbar). A laser (Genesis MX 532-

1000 SLM OPS, Coherent, $\lambda=532$ nm) periodically heated the samples at their center. The excitation frequency was varied between 0.1 and 1 Hz. After 20 drop periods, an IR camera (Image IR 9430, InfraTec GmbH) detected the temperature change for 100 s. With a frame rate of 20 fps, this resulted in 2000 images and a noise level of $\frac{30 \text{ mK}}{\sqrt{2000}} < 1$ mK. The amplitude and phase were calculated in real time using Infracore's IRBIS active online software. The resulting data were evaluated with a custom Python package. It detects the excitation center and fits an ellipse to the amplitude. Afterward, all points on top of the two main axes of the ellipse are evaluated using the slope method (29). For each OSZ content, three samples were measured. The resulting diffusivity values for each sample at each frequency and the two different axes were averaged for the final in-plane diffusivity.

Effective density

The samples' height for cross-plane thermal diffusivity characterization was measured via laser microscopy (LEXT OLS5000, Olympus IMS). Cylinders of 10 mm in diameter were cut from the nonwovens. Individual samples were put on the microscope stage. To ensure a flat contact, a glass slide was put on either side of the sample, leaving an unobstructed strip of about 5 mm in the center of the sample. A height image was acquired, and the average height of the sample was determined.

The mass of the samples was determined with a microscale (Cubis Micro Balance, Sartorius Lab Instruments GmbH). The volume was calculated from the known area ($A = \pi r^2 \approx 78.5 \text{ mm}^2$) and the measured height. The measurement was repeated for nine samples for each OSZ content. The given density is the average of all samples with the standard deviation being the error.

Heat capacity

Heat capacity was measured via differential scanning calorimetry (DSC; Discovery DSC 2500, TA instruments) of one sample for each OSZ content according to the American Society for Testing and Materials E1269-11 standard. All samples were ground to a powder before the measurement to ensure good contact with the DSC pans. Two heating cycles between -40° and 200°C were performed with a 20 K/min heating rate. Only the second heating cycle was evaluated. The measurement was repeated four times. The final value is the average of all measurement runs at 23°C .

Temperature-dependent electric resistivity

Samples of about 25 mm by 25 mm size were measured via the van der Pauw method (30). Four spring-loaded probes were placed at the edges of the sample. A current of 0.1 mA was applied with a Keithley 6221 current source, while the voltage was simultaneously measured with a Keithley 6517 electrometer. The temperature of the sample was controlled with an Instec mK2000 controller. The resistance was measured from -50° to 300°C with a 2 K/min heating rate. Specific resistivity was calculated by measuring the thickness of the samples with a Mitutoyo Litematic VL-50.

Nuclear magnetic resonance

NMR experiments were performed with a Bruker Avance II 300 (magnetic field of 7.05 T) spectrometer in a 4-mm triple resonance sample head (also from Bruker) at a rotation speed of 10 kHz. The ^{29}Si MAS NMR measurements were performed using a single-pulse quantitative experiment with a 90° pulse length of 3.5 μs , a recycle delay of 60 s, and no proton decoupling during acquisition. The

SCIENCE ADVANCES | RESEARCH ARTICLE

spectra are indirectly referenced with $N(\text{SiMe}_3)_3/\sigma(\text{iso}) = 2.4$ ppm, with respect to tetramethylsilanes [$\sigma(\text{iso}) = 0.0$ ppm].

Pore size tests

Pore size measurements were carried out on a capillary flow porometer PSM 165/H (Dresden, Germany). The standard test liquid Topor (surface tension = 16.0 mN/m) was used. The specimens were cut into squares (length about 2 cm) and covered the sample holder hole. The sample holder diameter is 11 mm, and N_2 flow rate was up to 70 liters/min.

Elemental analysis

The measurements were carried out at Mikroanalytisches Labor Pascher (www.mikrolabor.com, Germany). According to the company, the following methods were used: carbon in the polymer, oxidized, and ceramic state.

The samples were burned with a combustion additive at about 1200°C in a stream of oxygen; the contained carbon burned to CO_2 . The CO_2 was dissolved in sodium hydroxide solution, and the carbon content in the sample was calculated from the change in electrical conductivity (conductometry).

Hydrogen in the polymer, oxidized, and ceramic state

The samples were burned at 1050°C in an oxygen stream. The combustion water formed was determined by IR spectroscopy.

Nitrogen in the polymer and oxidized state

The sample was melted at a temperature of 900°C in the oxygen stream with a catalyst. Ammonia, N_2 , or NO_x formed were passed over copper oxide and reduced to N_2 after switching the carrier gas to CO_2 , excess oxygen was bound. The nitrogen formed was purged into an azotometer. Acidic reaction gasses and the carrier gas CO_2 were bound by potassium hydroxide solution. The nitrogen gas was measured volumetrically.

Nitrogen in the ceramic state

The sample was degassed in a heated graphite crucible. The released nitrogen was measured with helium as carrier gas with thermal conductivity detection.

Oxygen in the polymer and oxidized state

Samples were pyrolyzed at 1500°C in a glass carbon tube with carbon contact. Oxygen was detected as CO and measured by thermal conductivity detection.

Oxygen in the ceramic state

The sample was degassed in a hot graphite crucible. The CO/CO_2 produced by the reaction of the released oxygen with the graphite was pumped off and detected by IR spectroscopy.

Silicon in the polymer and oxidized state

After pressure digestion with nitric acid, the silicon dioxide formed was digested with sodium hydroxide solution under pressure. Detection was carried out by ICP-AES (inductively coupled plasma-atomic emission spectroscopy).

Silicon in the ceramic state

The sample was digested under melting (with a soda-borax mixture in a Pt crucible) and then dissolved with water. The detection was done by ICP-AES.

Scanning transmission electron microscopy

We performed HAADF-STEM imaging and chemical analyses on a field emission scanning transmission electron microscope [Field Electron and Ion Company (FEI), Titan G2 80-200 S/TEM], equipped with an EDS (four silicon drift detectors, Bruker

Quantax) and electron energy-loss spectrometer (EELS; Gatan Imaging Filter, Quantum SE) to observe and analyze the chemical compositions and relative thicknesses of the samples against a chemical standard of a C/SiCON nonwoven, respectively. For the TEM sample preparation, we used ultramicrotomy and Ar-milling methods to make thin cross-sectional specimens using an ultramicrotomy machine and Jeol Ion Slice. The TEM thin foils were a thickness of 50 to 150 nm, but we selected approximately the same thickness areas for the EDS by using zero-loss spectra in the EELS. The EDS maps were taken at a resolution of 5 to 10 nm per pixel and a dwell time of 16 μs using a subnanometer-sized electron beam with less than 0.09-nA probe current at 200-kV acceleration voltage. To accumulate statistically enough characteristic x-ray counts in a quantitative EDS map, the total acquisition time was about 60 min. During the acquisition, an image drift correction function was always activated to prevent artifacts in the profile. To get quantitative compositions of the samples, we corrected z-number and absorption effects on the evaluations of EDS spectrum, based on the chemical compositions of a C/SiCON-50 nonwoven measured in Laboratory Pascher.

Limiting oxygen index

The LOI experiments were carried out on an Fire Testing Technology Oxygen Index Apparatus ISO 4589-3-NES 715 (Edenharter, Germany). The nonwoven samples were cut in shapes (width about 1 cm and length about 6 cm) and fixed in the device. The respective oxygen and nitrogen composition were adjusted before the measurement. Then, the samples were exposed to the oxygen and nitrogen composition atmosphere for 5 min and followed by burning with a methane flame. The composition of oxygen and nitrogen at which the sample burned down independently was recorded. When the methane flame was removed and even at 100% O_2 , the flame was immediately extinguished, and an LOI value of 100 $\text{O}_2\%$ was recorded (movie S4).

Burning tests

The burning test was conducted in a hood in the air atmosphere. For the burning tests, the nonwovens were cut in rectangular shapes (width: 4 cm and length: 6 cm) and fixed in a metal frame. The metal frame with the nonwoven was placed on a metal rack, with a methane burner installed beneath it. Then, the samples were burned with a methane flame (rate: 0.5 liter/min). After ignition, the samples were burned for 5 min, and the whole process was recorded by video (movie S5).

Supplementary Materials

This PDF file includes:

Figs. S1 to S22
Tables S1 to S4
Legends for movies S1 to S5
References

Other Supplementary Material for this manuscript includes the following:

Movies S1 to S5

Downloaded from https://www.science.org at Universitaet Bayreuth on April 03, 2023

REFERENCES AND NOTES

- X. Qian, J. Zhou, G. Chen, Phonon-engineered extreme thermal conductivity materials. *Nat. Mater.* **20**, 1188–1202 (2021).
- Q. D. Gibson, T. Zhao, L. M. Daniels, H. C. Walker, R. Daou, S. Hébert, M. Zanella, M. S. Dyer, J. B. Claridge, B. Slater, M. W. Gaultois, F. Corà, J. Alaria, M. J. Rosseinsky, Low thermal conductivity in a modular inorganic material with bonding anisotropy and mismatch. *Science* **373**, 1017–1022 (2021).
- D. J. Voneshen, K. Refson, E. Borissenko, M. Krisch, A. Bosak, A. Piovano, E. Cernal, M. Enderle, M. J. Gutmann, M. Hoesch, M. Roger, L. Gannon, A. T. Boothroyd, S. Uthayakumar, D. G. Porter, J. P. Goff, Suppression of thermal conductivity by rattling modes in thermoelectric sodium cobaltate. *Nat. Mater.* **12**, 1028–1032 (2013).
- J. S. Kang, H. Wu, M. Li, Y. Hu, Intrinsic low thermal conductivity and phonon renormalization due to strong anharmonicity of single-crystal Tin selenide. *Nano Lett.* **19**, 4941–4948 (2019).
- W. Li, S. Lin, M. Weiss, Z. Chen, J. Li, Y. Xu, W. G. Zeier, Y. Pei, Crystal structure induced ultralow lattice thermal conductivity in thermoelectric Ag_3AlSe_6 . *Adv. Energy Mater.* **8**, 1800030 (2018).
- S. K. Saha, Exploring the origin of ultralow thermal conductivity in layered BiOCuSe . *Phys. Rev. B* **92**, 041202 (2015).
- J. Yang, B. Zhang, A. D. Christodoulides, Q. Xu, A. Zangiabadi, S. R. Peurifoy, C. K. McGinn, L. Dai, E. Meirzadeh, X. Roy, M. L. Steigerwald, I. Kyimissis, J. A. Malen, C. Nuckolls, Solution-processable superlattice thin-films. *J. Am. Chem. Soc.* **141**, 10967–10971 (2019).
- B. Jiang, Y. Yu, J. Cui, L. Liu, L. Xie, J. Liao, Q. Zhang, Y. Huang, S. Ning, B. Jia, B. Zhu, S. Bai, L. Chen, S. J. Pennycook, J. He, High-entropy-stabilized chalcogenides with high thermoelectric performance. *Science* **371**, 830–834 (2021).
- J. J. Kuo, M. Wood, T. J. Slade, M. G. Kanatzidis, G. J. Snyder, Systematic over-estimation of lattice thermal conductivity in materials with electrically-resistive grain boundaries. *Energ. Environ. Sci.* **13**, 1250–1258 (2020).
- G. Chen, Size and interface effects on thermal conductivity of superlattices and periodic thin-film structures. *J. Heat Mass Transf.* **119**, 220–229 (1997).
- W. Sun, A. Du, G. Gao, J. Shen, G. Wu, Graphene-templated carbon aerogels combining with ultra-high electrical conductivity and ultra-low thermal conductivity. *Microporous Mesoporous Mater.* **253**, 71–79 (2017).
- L. Peng, Z. Xu, Z. Liu, Y. Guo, P. Li, C. Gao, Ultrahigh thermal conductive yet superflexible graphene films. *Adv. Mater.* **29**, 1700589 (2017).
- G. Xin, T. Yao, H. Sun, S. M. Scott, D. Shao, G. Wang, J. Lian, Highly thermally conductive and mechanically strong graphene fibers. *Science* **349**, 1083–1087 (2015).
- Y. Wang, Y. Chen, S. D. Lacey, L. Xu, H. Xie, T. Li, V. A. Danner, L. Hu, Reduced graphene oxide film with record-high conductivity and mobility. *Mater. Today* **21**, 186–192 (2018).
- N. K. Mahanta, A. R. Abramson, M. L. Lake, D. J. Burton, J. C. Chang, H. K. Mayer, J. L. Ravine, Thermal conductivity of carbon nanofiber mats. *Carbon* **48**, 4457–4465 (2010).
- L. C. Herrera-Ramírez, M. Cano, R. G. de Villoria, Low thermal and high electrical conductivity in hollow glass microspheres covered with carbon nanofiber-polymer composites. *Compos. Sci. Technol.* **151**, 211–218 (2017).
- Y. Shang, Z. Liu, J. Dong, M. Yao, Z. Yang, Q. Li, C. Zhai, F. Shen, X. Hou, L. Wang, N. Zhang, W. Zhang, R. Fu, J. Ji, X. Zhang, H. Lin, Y. Fei, B. Sundqvist, W. Wang, B. Liu, Ultrahard bulk amorphous carbon from collapsed fullerene. *Nature* **599**, 599–604 (2021).
- S. S. Roy, M. S. Arnold, Improving graphene diffusion barriers via stacking multiple layers and grain size engineering. *Adv. Funct. Mater.* **23**, 3638–3644 (2013).
- S. Zhao, G. Siqueira, S. Drdova, D. Norris, C. Ubert, A. Bonnin, S. Galmarini, M. Ganobjak, Z. Pan, S. Brunner, G. Nyström, J. Wang, M. M. Koebel, W. J. Malfait, Additive manufacturing of silica aerogels. *Nature* **584**, 387–392 (2020).
- X. Xu, Q. Zhang, M. Hao, Y. Hu, Z. Lin, L. Peng, T. Wang, X. Ren, C. Wang, Z. Zhao, C. Wan, H. Fei, L. Wang, J. Zhu, H. Sun, W. Chen, T. Du, B. Deng, G. J. Cheng, I. Shakir, C. Dames, T. S. Fisher, X. Zhang, H. Li, Y. Huang, X. Duan, Double-negative-index ceramic aerogels for thermal superinsulation. *Science* **363**, 723–727 (2019).
- L. Su, H. Wang, M. Niu, S. Dai, Z. Cai, B. Yang, H. Huan, X. Pan, Anisotropic and hierarchical SiC@SiO_2 nanowire aerogel with exceptional stiffness and stability for thermal superinsulation. *Sci. Adv.* **6**, eaay6689 (2020).
- M. Biesuz, E. Zera, M. Tomasi, P. Jana, O. Ersen, W. Baaziz, A. Lindemann, G. D. Soraru, Polymer-derived Si_3N_4 nanofelts for flexible, high temperature, lightweight and easy-manufacturable super-thermal insulators. *Appl. Mater. Today* **20**, 100648 (2020).
- D. P. Anderson, Carbon fiber morphology. 2. Expanded wide-angle x-ray diffraction studies of carbon fibers. Wright-Patterson, Air Force Base, Dayton, Ohio (Accession Number: ADA235599), (1991).
- L. F. B. Ribeiro, O. Flores, P. Furtat, C. Gervais, R. Kempe, R. A. F. Machado, G. Motz, A novel PAN/silazane hybrid polymer for processing of carbon-based fibres with extraordinary oxidation resistance. *J. Mater. Chem. A* **5**, 720–729 (2017).
- E. Zussman, X. Chen, W. Ding, L. Calabri, D. A. Dikin, J. P. Quintana, R. S. Ruoff, Mechanical and structural characterization of electrospun PAN-derived carbon nanofibers. *Carbon* **43**, 2175–2185 (2005).
- S. Prilutsky, E. Zussman, Y. Cohen, The effect of embedded carbon nanotubes on the morphological evolution during the carbonization of poly (acrylonitrile) nanofibers. *Nanotechnology* **19**, 165603 (2008).
- C. A. Klein, STB model and transport properties of pyrolytic graphites. *J. Appl. Phys.* **35**, 2947–2957 (1964).
- A. Philipp, N. W. Pech-May, B. A. F. Kopera, A. M. Lechner, S. Rosenfeldt, M. Retsch, Direct measurement of the in-plane thermal diffusivity of semitransparent thin films by lock-in thermography: An extension of the slopes method. *Anal. Chem.* **91**, 8476–8483 (2019).
- A. Mendioroz, R. Fuente-Dacal, E. Apiñaniz, A. Salazar, Thermal diffusivity measurements of thin plates and filaments using lock-in thermography. *Rev. Sci. Instrum.* **80**, 074904 (2009).
- O. Philips Gloeilampenfabrieken, A method of measuring specific resistivity and Hall effect of discs of arbitrary shape. *Philips Res. Rep.* **13**, 1–9 (1958).
- D. Van Krevelen, K. Te Nijenhuis, “[Product properties (II) Environmental behaviour and failure]” in *Properties of Polymers*, (Elsevier, 2009), chap. 26, pp. 847–873.
- X. Xu, Q. Zhang, Y. Yu, W. Chen, H. Hu, H. Li, Naturally dried graphene aerogels with superelasticity and tunable poisson's ratio. *Adv. Mater.* **28**, 9223–9230 (2016).
- Z. Fan, D. Z. Y. Tng, C. X. T. Lim, P. Liu, S. T. Nguyen, P. Xiao, A. Marconnet, C. Y. H. Lim, H. M. Duong, Thermal and electrical properties of graphene/carbon nanotube aerogels. *Colloids Surf. A Physicochem. Eng. Asp.* **445**, 48–53 (2014).
- X. Hou, R. Zhang, D. Fang, Superelastic, fatigue resistant and heat insulated carbon nanofiber aerogels for piezoresistive stress sensors. *Ceram. Int.* **46**, 2122–2127 (2020).
- B. Wicklein, A. Kocjan, G. Salazar-Alvarez, F. Carosio, G. Camino, M. Antonietti, L. Bergström, Thermally insulating and fire-retardant lightweight anisotropic foams based on nanocellulose and graphene oxide. *Nat. Nanotechnol.* **10**, 277–283 (2015).
- Y. Xie, S. Xu, Z. Xu, H. Wu, C. Deng, X. Wang, Interface-mediated extremely low thermal conductivity of graphene aerogel. *Carbon* **98**, 381–390 (2016).
- Y. Lei, Z. Hu, B. Cao, X. Chen, H. Song, Enhancements of thermal insulation and mechanical property of silica aerogel monoliths by mixing graphene oxide. *Mater. Chem. Phys.* **187**, 183–190 (2017).
- C. Yue, J. Feng, J. Feng, Y. Jiang, Efficient gaseous thermal insulation aerogels from 2-dimension nitrogen-doped graphene sheets. *Int. J. Heat Mass Transf.* **109**, 1026–1030 (2017).
- Q. Peng, Y. Qin, X. Zhao, X. Sun, Q. Chen, F. Xu, Z. Lin, Y. Yuan, Y. Li, J. Li, W. Yin, C. Gao, F. Zhang, X. He, Y. Li, Superlight, mechanically flexible, thermally superinsulating, and antifrosting anisotropic nanocomposite foam based on hierarchical graphene oxide assembly. *ACS Appl. Mater. Interfaces* **9**, 44010–44017 (2017).
- Y. Qin, Q. Peng, Y. Zhu, X. Zhao, Z. Lin, X. He, Y. Li, Lightweight, mechanically flexible and thermally superinsulating rGO/polyimide nanocomposite foam with an anisotropic microstructure. *Nanoscale Adv.* **1**, 4895–4903 (2019).
- X. Lu, O. Nilsson, J. Fricke, R. W. Pekala, Thermal and electrical conductivity of monolithic carbon aerogels. *J. Appl. Phys.* **73**, 581–584 (1993).
- Y. W. Chen, H. Zhan, J. N. Wang, A direct foaming approach for carbon nanotube aerogels with ultra-low thermal conductivity and high mechanical stability. *Nanoscale* **13**, 11878–11886 (2021).
- M. J. Oh, J. H. Lee, P. J. Yoo, Graphene-based ultralight compartmentalized isotropic foams with an extremely low thermal conductivity of $5.75 \text{ mW m}^{-1} \text{ K}^{-1}$. *Adv. Funct. Mater.* **31**, 2007392 (2020).

Acknowledgments: We thank S. Rettinger for DSC measurements and acknowledge technical support from Hot Disk AB company for communicating, discussing, and confirming the thermal conductivity and ANSYS Inc. for the ANSYS License Key. We thank F. Puchter and J. Breu for support in the LOI and burning test; C. Kunert and M. Schwarzmann for preparing thin cross-sectional specimens for the TEM measurement; R. Siegel, B. Bojer, and J. Senker for ^{29}Si solid NMR measurement; and H. Zhang for the technical support with Fig. 1. We acknowledge the use of the research facilities of the University of Bayreuth, the Bavarian Polymer Institute (keyLabs: optical and electron microscopy and mesoscale characterization: scattering techniques), Bayerisches Geoinstitut, and Northern Bavarian NMR Centre for this project. **Funding:** The work was supported by the University of Bayreuth and the Deutsche Forschungsgemeinschaft (DFG). A.G. and G.M. would like to thank DFG (Deutsche Forschungsgemeinschaft) for the financial support (GR 972/61-1 and 455984818 (MO 851/251-1). The Titan G2 TEM at BGI (Bayerisches Geoinstitut) was financed by DFG grant INST 917/251-1 FUGG. **Author contributions:** A.G., G.M., and S.A. conceived and supervised the project. Concept, methodology, and the objectives of the research were decided by X.L. in consultation with J.D., A.G., G.M., M.R., and S.A. The preparation of nonwovens and characterization by SEM, electrical conductivity, LOI, and burning test measurements were done by X.L. and J.D. XRD and mechanical folding tests were done by X.L. Thermal conductivity (TPS) and Raman measurements were performed by L.B. T.T. measured the thermal conductivity (LIT and LFA)

SCIENCE ADVANCES | RESEARCH ARTICLE

and electrical conductivity and evaluated the data. N.M. performed the STEM-EDS microscopy. S.R. measured XPS. All authors contributed to the discussion of the data. S.S. helped in discussions. The manuscript is written by input from all authors under the lead of X.L., S.A., and A.G. **Competing interests:** The authors declare that they have no competing interests. **Data and materials availability:** All data needed to evaluate the conclusions in the paper are present in the paper and/or the Supplementary Materials.

Submitted 26 August 2022
Accepted 2 March 2023
Published 31 March 2023
10.1126/sciadv.ade6066

Downloaded from <https://www.science.org> at Universitaet Bayreuth on April 03, 2023

ScienceAdvances

Extremely low thermal conductivity and high electrical conductivity of sustainable carbon ceramic electrospun nonwoven materials

Xiaojian Liao, Jakob Denk, Thomas Tran, Nobuyoshi Miyajima, Lothar Benker, Sabine Rosenfeldt, Stefan Schaffner, Markus Retsch, Andreas Greiner, Gnter Motz, and Seema Agarwal

Sci. Adv., **9** (13), eade6066.
DOI: 10.1126/sciadv.ade6066

View the article online

<https://www.science.org/doi/10.1126/sciadv.ade6066>

Permissions

<https://www.science.org/help/reprints-and-permissions>

Downloaded from <https://www.science.org> at Universitaet Bayreuth on April 03, 2023

Use of this article is subject to the [Terms of service](#)

Science Advances (ISSN) is published by the American Association for the Advancement of Science, 1200 New York Avenue NW, Washington, DC 20005. The title *Science Advances* is a registered trademark of AAAS.
Copyright © 2023 The Authors, some rights reserved; exclusive licensee American Association for the Advancement of Science. No claim to original U.S. Government Works. Distributed under a Creative Commons Attribution License 4.0 (CC BY).



Supplementary Materials for

Extremely low thermal conductivity and high electrical conductivity of sustainable carbon-ceramic electrospun nonwoven materials

Xiaojian Liao *et al.*

Corresponding author: Seema Agarwal, agarwal@uni-bayreuth.de; Günter Motz, guenter.motz@uni-bayreuth.de; Markus Retsch, markus.retsch@uni-bayreuth.de

Sci. Adv. **9**, eade6066 (2023)
DOI: 10.1126/sciadv.ade6066

The PDF file includes:

Figs. S1 to S22
Tables S1 to S4
Legends for movies S1 to S5
References

Other Supplementary Material for this manuscript includes the following:

Movies S1 to S5

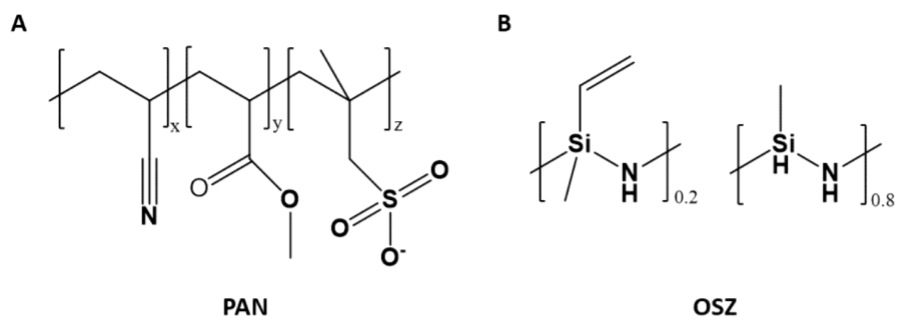


Fig. S1.

Chemical structures of the precursors. (A) polyacrylonitrile copolymer (PAN) and (B) oligosilazane (OSZ).

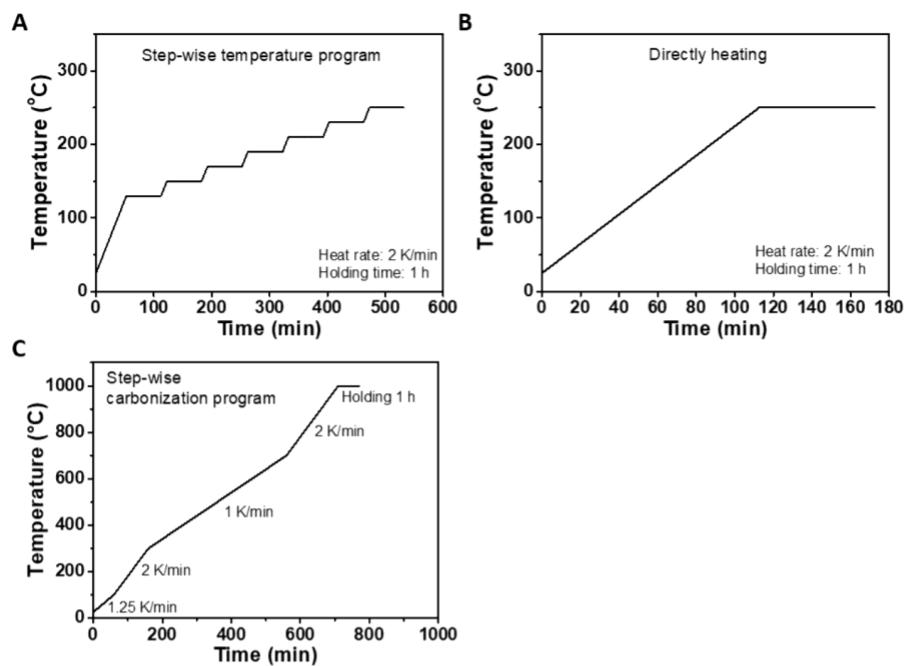


Fig. S2.

Heating program plots during the stabilization and the carbonization and ceramization processes. (A) Step-wise stabilization temperature program. (B) Directly stabilization heating program. (C) Step-wise carbonization and ceramization temperature program.

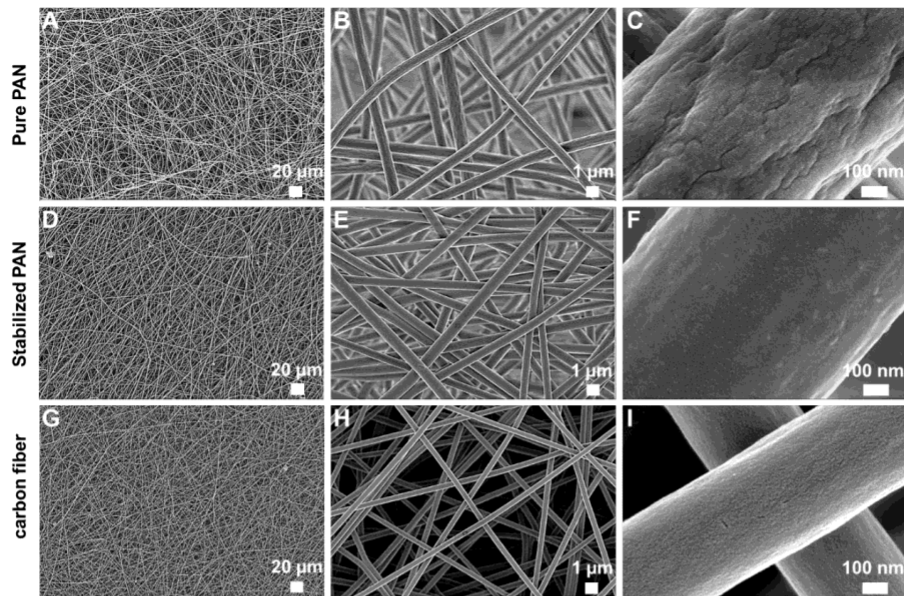


Fig. S3.

Surface SEM images of nonwovens with different magnifications. (A-C) Pure PAN. (D-F) Stabilized PAN nonwoven. (G-I) Carbon nonwoven.

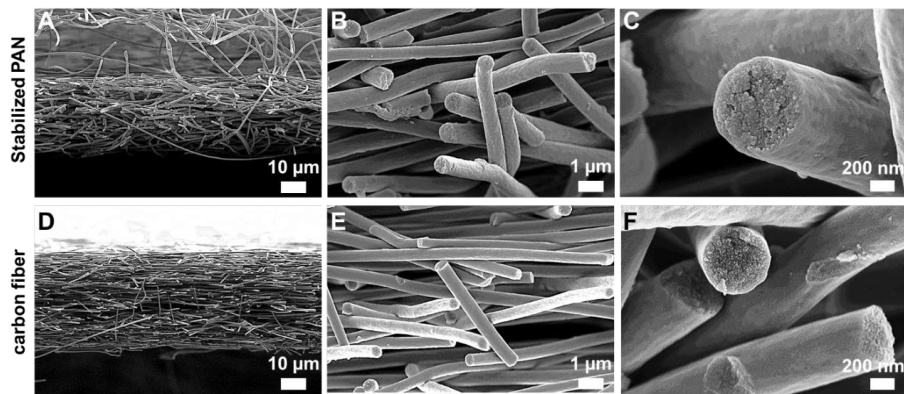


Fig. S4.

Cross-sectional SEM images of nonwovens with different magnifications. (A-C) stabilized PAN nonwoven. (D-F) carbon nonwoven.

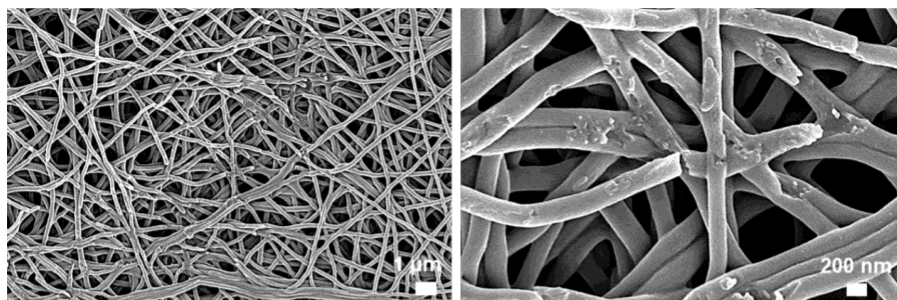


Fig. S5.

Surface SEM images of brittle pure carbon nonwoven in different magnifications. The samples were stabilized by heating from 20 °C to 250 °C with a heating rate of 2 K/min and holding the temperature at 250 °C for 1 h in the air. Afterward, the carbonization was performed under nitrogen in a tube oven, for which the samples were heated with 2 K/min to 1000 °C and annealed at this temperature for 1 h.

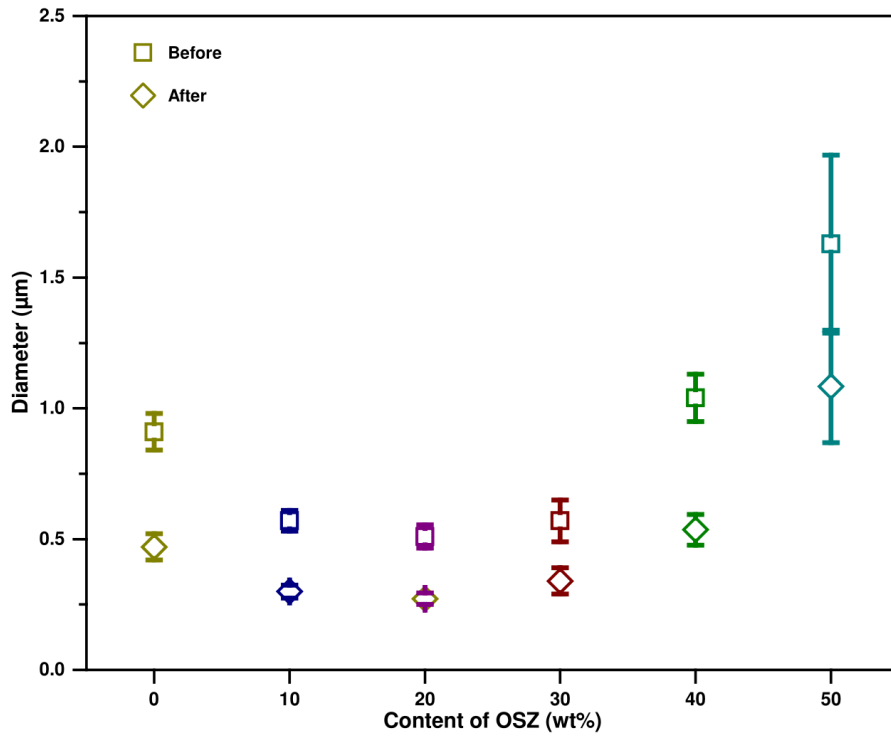


Fig. S6.

Changes in fiber diameter with the function of the content of OSZ. Before: polymer PAN/OSZ-X fibers. After: C/SiCON-X fibers. The SEM images were used to determine the diameter of fibers. The quantitative analysis of the average diameter and standard deviation of the mean values was carried out by ImageJ software.

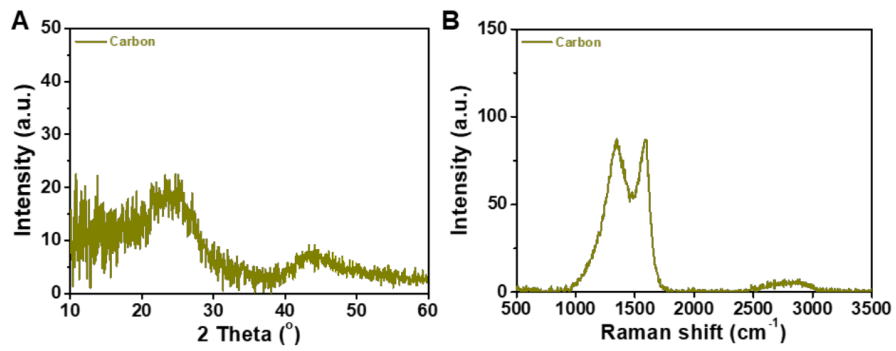


Fig. S7.

Characterization of pure carbon nonwovens. (A) XRD analysis of the pure carbon nonwovens. (B) Raman spectra of the pure carbon nonwovens.

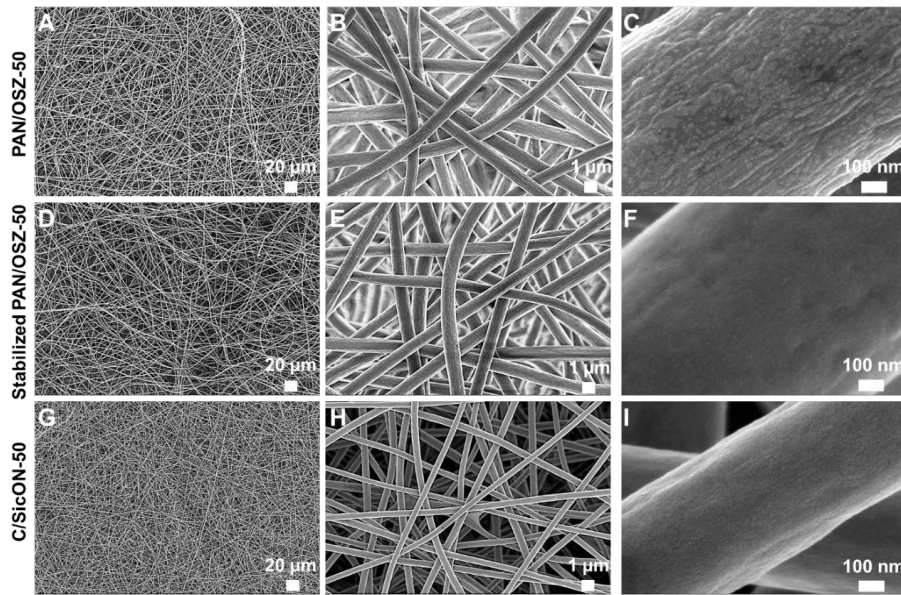


Fig. S8.

Surface SEM images of nonwovens with different magnifications. (A-C) PAN/OSZ-50 nonwoven. (D-F) stabilized PAN/OSZ-50 nonwoven. (G-I) C/SiCON-50 nonwoven.

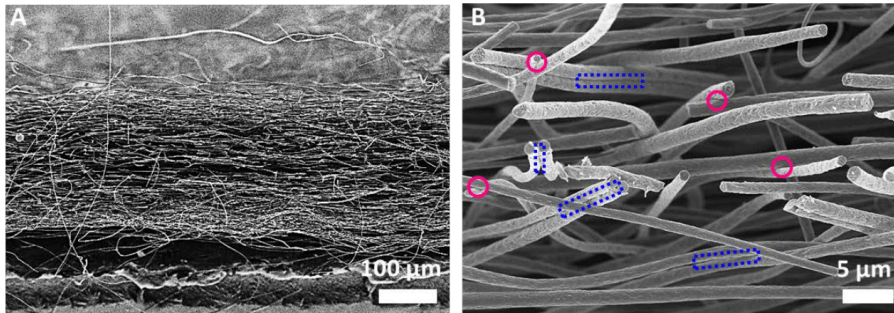


Fig. S9.

SEM images of the cross-section of C/SiCON-50 nonwoven in different magnifications. The two typical fiber-fiber contact points are marked in B: 1, pink circles (solid line) are the intersection points of two fibers; 2, blue rectangles (dotted line) are the side-by-side contacts.

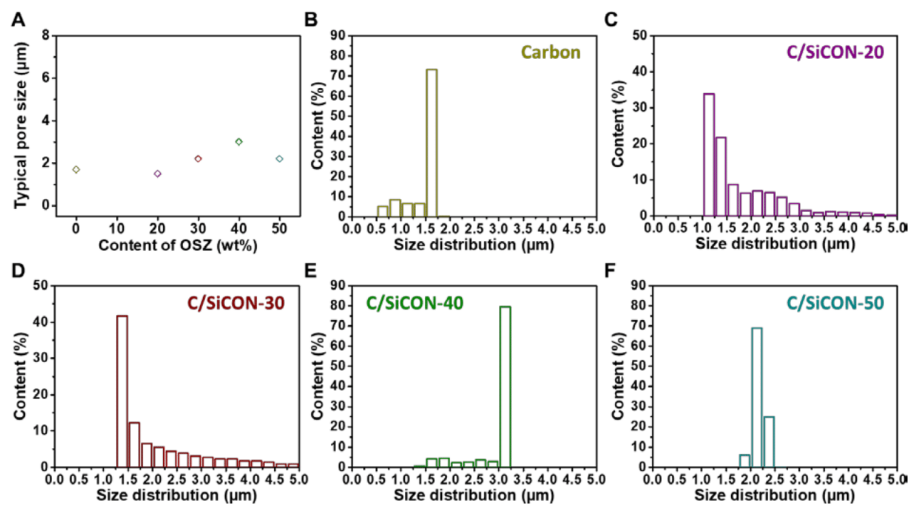


Fig. S10.

Pore size analysis of nonwovens with different contents of OSZ to PAN. (A) Changes in typical pore size as the function of the content of OSZ. (B-F) Size distribution of nonwovens.

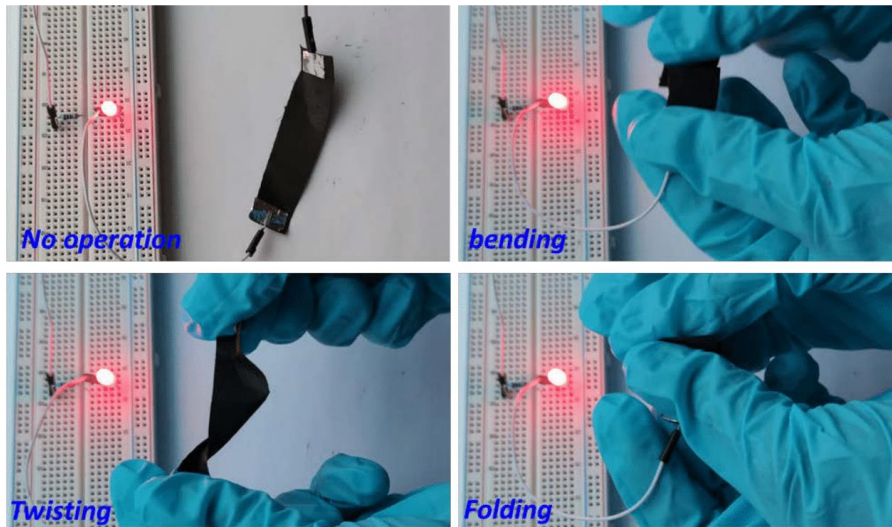


Fig. S11.
Digital photos showing the C/SiCON-50 nonwoven lighting a LED lamp under bending, twisting, and folding operations.

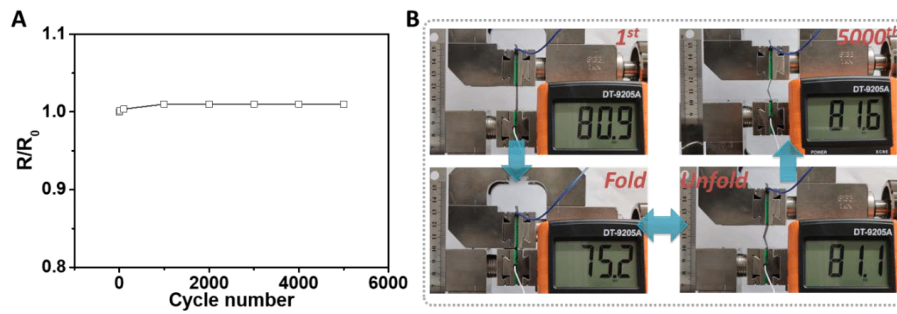


Fig. S12.

Analysis of the foldability of the nonwoven. (A) Resistance ratio change of C/SiCON-50 during the 5000-cycle folding-unfolding test (folding strain from 10% to 99%). (B) Photographs of the folding test at the 1st cycle and unfolding test at the 5000th cycle.

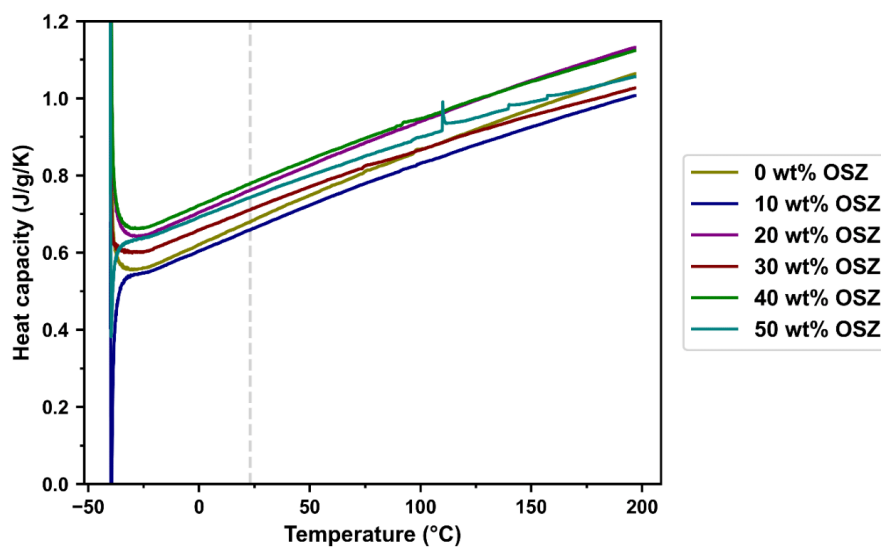


Fig. S13.

Temperature-dependent heat capacity for different OSZ contents. An increase of the heat capacity with increasing temperature can be seen. No phase transition is visible in the investigated temperature region. For evaluation of thermal conductivity, the average value at 23°C (dashed line) for four different measurements was taken.

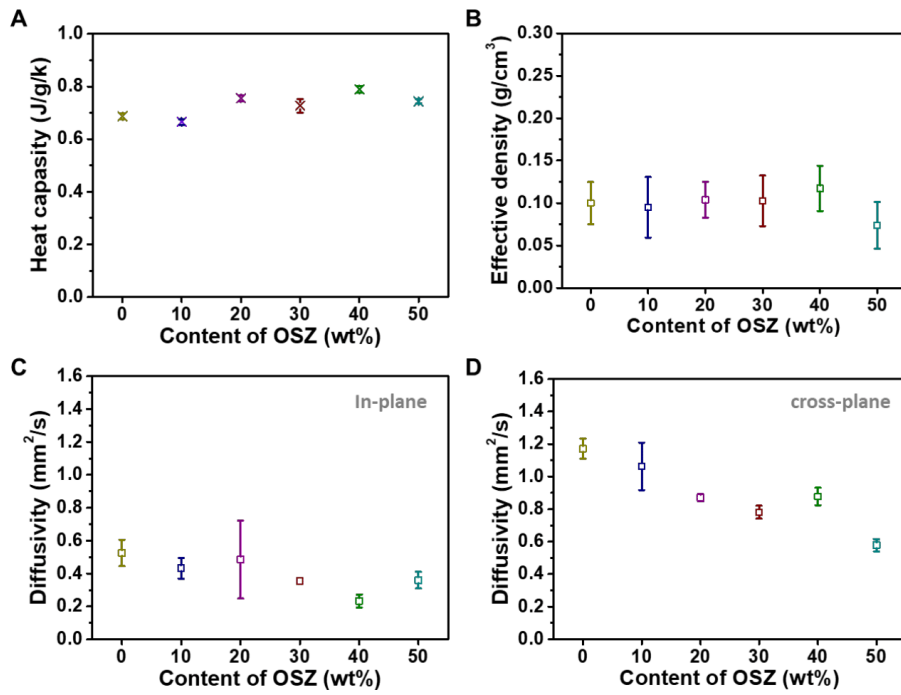


Fig. S14.

Characterization of nonwovens with different contents of OSZ to PAN. (A) heat capacity, (B) effective density, (C) in-plane diffusivity, and (D) cross-plane diffusivity.

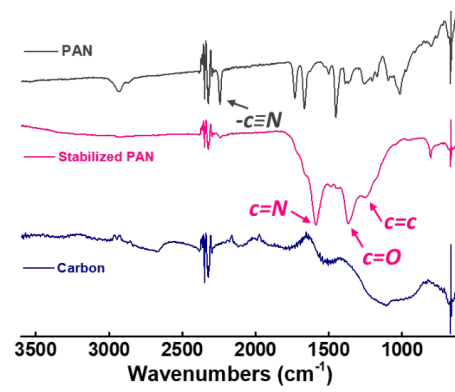


Fig. S15.
ATR-FTIR spectra of the polymer, stabilized and carbonized nonwovens from PAN.

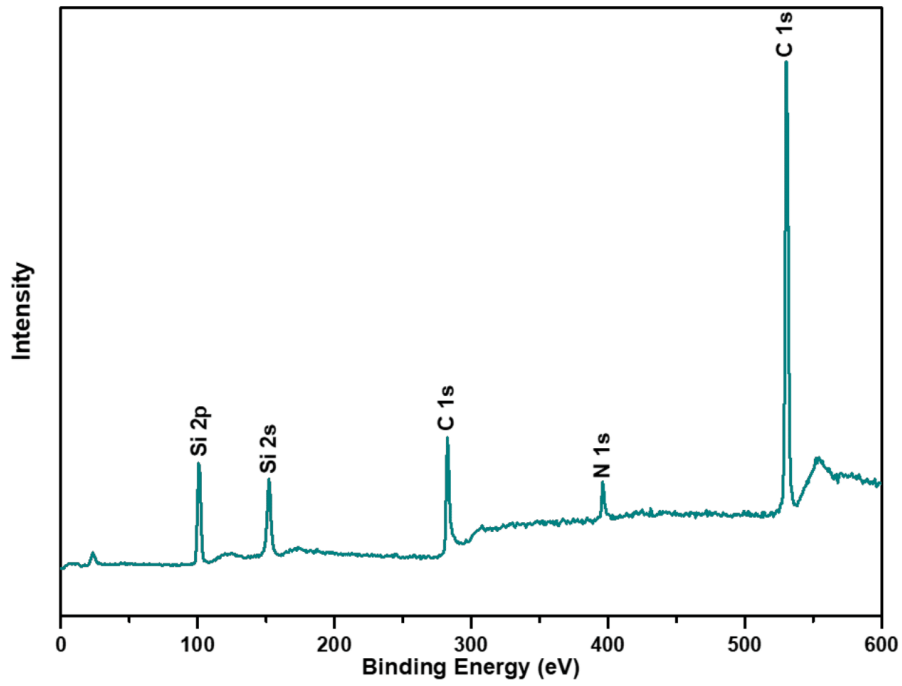


Fig. S16.

Full XPS spectra of C/SiCON-50 nonwoven. An atomic ratio of C:Si:N:O species of 31.6:17.6:5.6:5.6 % (equal to 22.5:29.5:4.7:43.5 wt%).

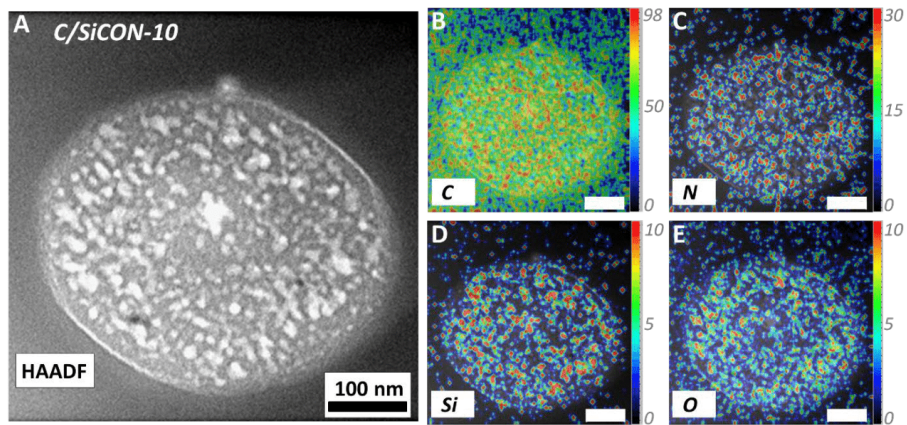


Fig. S17.

Nanostructure and elemental distribution of the C/SiCON-10 fiber. (A) High-resolution HAADF-STEM cross-section image. (B-E) EDS mapping (wt%) images showing a field of single C/SiCON-10 fiber's cross-section. Scale bars are 100 nm.

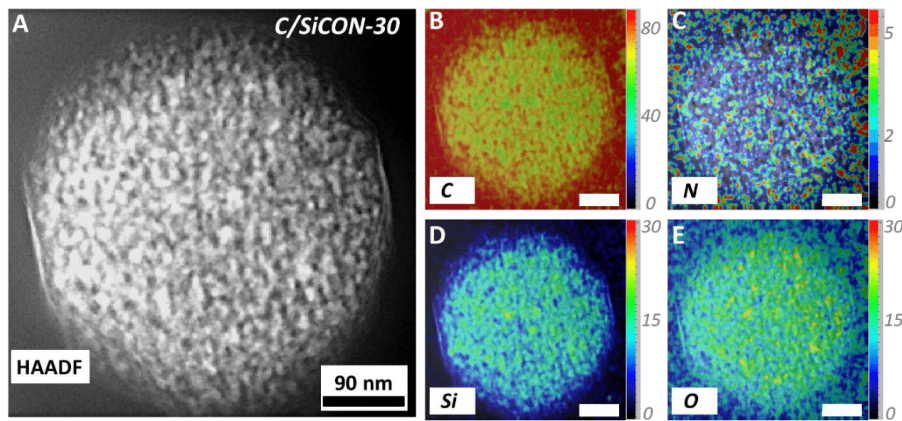


Fig. S18.

Nanostructure and elemental distribution of the C/SiCON-30 fiber. (A) High-resolution HAADF-STEM cross-section image. (B-E) EDS mapping (wt%) images showing a field of single C/SiCON-30 fiber's cross-section. Scar bars are 90 nm.

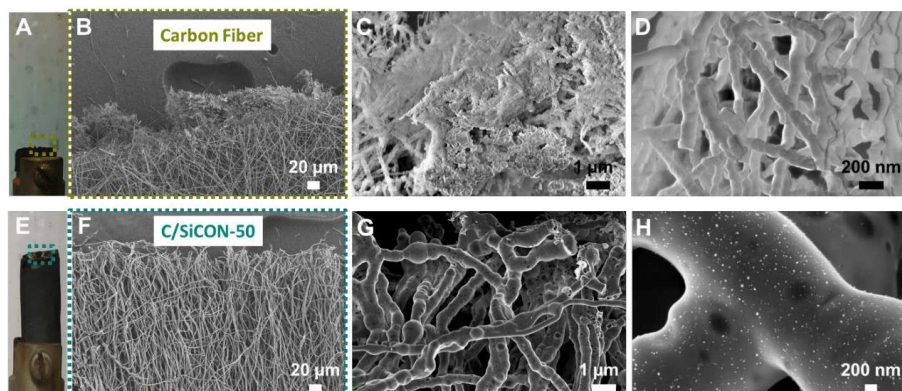


Fig. S19.

Digital photos and SEM images of nonwovens after LOI testing. (A-D) carbon nonwovens and (E-H) C/SiCON-50 nonwovens.

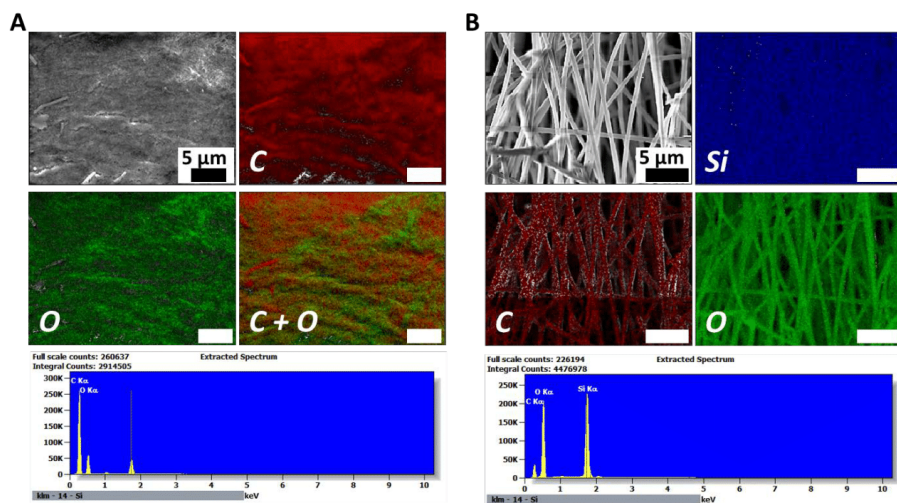


Fig. S20.

SEM and EDS maps of the nonwovens after LOI testing. (A) carbon nonwovens and (B) C/SiCON-50 nonwovens (B). The C and O weight percentages are 53.6 wt% and 46.4 wt% during the carbon nonwoven after LOI testing, respectively. The C, O, and Si weight percent are 10.4 wt%, 46.5 wt%, and 43.1 wt% during the C/SiCON-50 nonwoven after LOI testing, respectively.

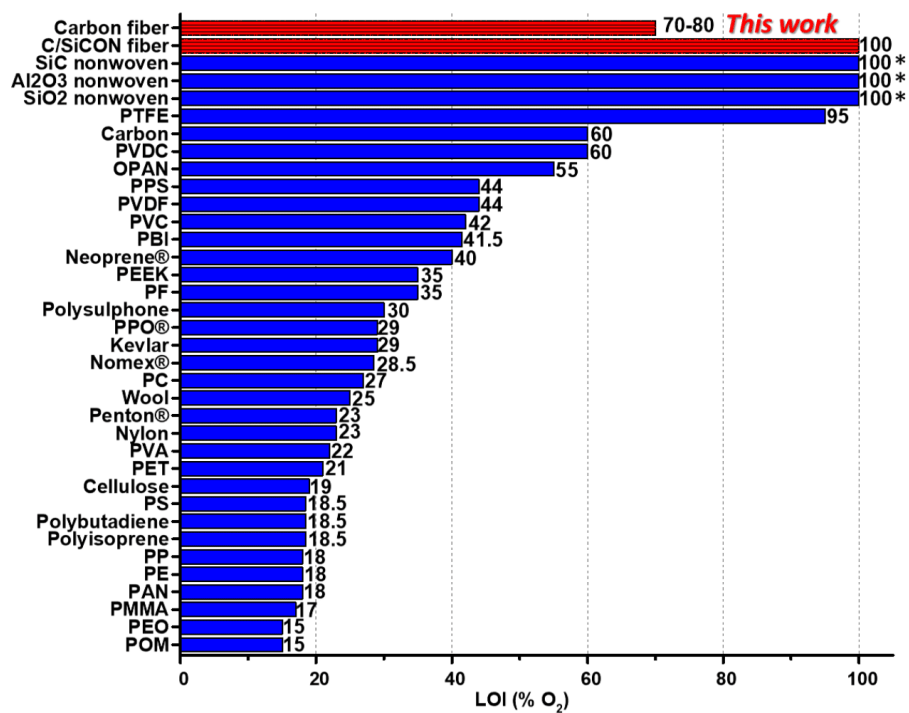


Fig. S21

Comparison of the LOI values between carbon nonwovens, C/SiCON nonwovens, and other materials (*: Measured by ourselves). The data in the plot are taken from the book: Properties of polymers, Chapter 26 - Product properties (II) Environmental behaviour and failure (31).

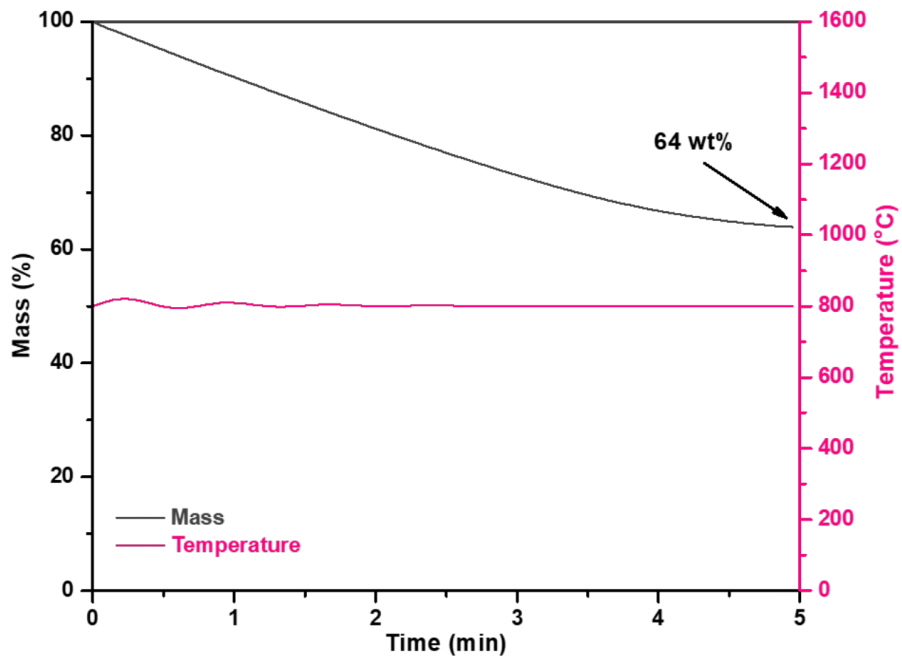


Fig. S22.

Isothermal measurement of C/SiCON-50 nonwoven at 800 °C for 5 min in air.

Content	PAN	OSZ	DMF	Acetone
wt%	g	g	g	g
0	1.0	0	4.7	0.96
10	1.0	0.11	5.10	0.57
20	1.0	0.25	5.53	0.61
30	1.0	0.43	6.03	0.67
40	1.0	0.67	6.03	0.67
50	1.0	1.0	6.40	0.67

Table S1.

Compositions of the electrospinning solutions. The solutions had 3 wt% DCP with respect to the weight of OSZ.

Materials	Thermal conductivity	Electrical conductivity	Density	Ref.
	mW/m/K	S/cm	mg/cm ³	
Graphene Aerogels	18	1.3	2-10	(32)
carbon nanofiber - polymer composites	170	7*10 ⁻⁶	820-1200	(16)
Graphene-templated carbon aerogels	27	2.25	23.5	(11)
Graphene/carbon nanotube aerogels	100	0.005	31-40	(33)
Graphene films	1.94*10 ⁶	10000	2000	(12)
Graphene fibers	1.3*10 ⁶	2210	1450-1850	(13)
Carbon nanofiber nonwovens	In-plane: 1.2-15.7 (*10 ⁴) Cross-plane: 428-711	--	106-739	(15)
Amorphous carbon	2.6*10 ⁴	--	3200-3300	(17)
Carbon nanofiber aerogels	26.5	--	6.6	(34)
Nanocellulose/graphene oxide foam	15	--	7	(35)
Graphene aerogel	4	--	2-6	(36)
SiO ₂ /GO composite aerogel	7.2-8.9	--	80-190	(37)
Nitrogen-doped graphene aerogel	12.58	--	32	(38)

Reduced graphene oxide/polyimide aerogel	9	--	9.2	(39)
Graphene oxide and polyimide aerogel	12-22	--	9-16	(40)
Carbon aerogels	29	0.6	82	(41)
Carbon nanotube aerogels	16.5		4.6	(42)
Graphene-based foam	5.75	--	2.4	(43)
Hexagonal boron nitride aerogels	20-24	Insulator	0.1-10	(20)
Si ₃ N ₄ nanofelts	11 (Ar)	Insulator	21	(22)
SiC@SiO ₂ nanowire aerogel	14	Insulator	6.5	(21)
Silica aerogels	15.9	Insulator	180	(19)
	In-plane: 31.8			
This work	cross-plane: 10-19.8	4.2	100	

Table S2.

Thermal conductivity, electrical conductivity and density of materials in relevant additional literature.

	2θ (°)	FWHM (°)	d ₀₀₀₂ spacing (Å) ^a	crystallite size, L _c (Stacking Height) (nm) ^b	crystallite size, L _a (Lateral Size) (nm) ^c
C-fiber	25.0	7.23	3.56	1.17	
	43.7	6.24			2.80
C/SiCON-50	25.4	8.65	3.49	0.98	
	43.8	6.65			2.63

^a: $2d \cdot \sin\theta = n\lambda$, $\lambda = 0.154$ nm.

^b: $L_c = 0.94\lambda / (B(2\theta) \cdot \cos(\theta))$, $B(2\theta)$ is FWHM.

^c: $L_a = 1.84\lambda / (B(2\theta) \cdot \cos(\theta))$, $B(2\theta)$ is FWHM.

Table S3.

XRD analysis of the pure carbon and C/SiCON-50 nonwovens. The information of the nanocrystallites was calculated based on the XRD analysis.

Element	PAN/OSZ-50	Stabilized PAN/OSZ-50	C/SiCON-50
	wt%	wt%	wt%
C	48.6	43.3	47.0
Si	14.0	16.1	23.2
O	8.6	16.3	21.8
N	17.4	13.1	6.5
H	6.0	4.18	0.5

Table S4.

Elemental analysis result of the nanofibrous nonwovens: PAN/OSZ-50, stabilized PAN/OSZ-50, and C/SiCON-50.
The measurements were carried out at Mikroanalytisches Labor Pascher (www.mikrolabor.com, Germany). 206

Movie S1.

Foldability of C/SiCON-50 nonwoven compared to printing paper.

Movie S2.

Flexible C/SiCON-50 nonwoven suffering the 5000-cycle folding-unfolding test with negligible electrical resistance change.

Movie S3.

Flexible C/SiCON-50 nonwoven conducting LED lamp.

Movie S4.

LOI tests of carbon nonwoven (80 % oxygen) and C/SiCON-50 nonwoven (100% oxygen).

Movie S5.

Burning test of carbon nonwoven and C/SiCON-50 nonwoven at about 800 degrees Celsius for 5 min.

REFERENCES AND NOTES

1. X. Qian, J. Zhou, G. Chen, Phonon-engineered extreme thermal conductivity materials. *Nat. Mater.* **20**, 1188–1202 (2021).
2. Q. D. Gibson, T. Zhao, L. M. Daniels, H. C. Walker, R. Daou, S. Hébert, M. Zanella, M. S. Dyer, J. B. Claridge, B. Slater, M. W. Gaultois, F. Corà, J. Alaria, M. J. Rosseinsky, Low thermal conductivity in a modular inorganic material with bonding anisotropy and mismatch. *Science* **373**, 1017–1022 (2021).
3. D. J. Voneshen, K. Refson, E. Borissenko, M. Krisch, A. Bosak, A. Piovano, E. Cemal, M. Enderle, M. J. Gutmann, M. Hoesch, M. Roger, L. Gannon, A. T. Boothroyd, S. Uthayakumar, D. G. Porter, J. P. Goff, Suppression of thermal conductivity by rattling modes in thermoelectric sodium cobaltate. *Nat. Mater.* **12**, 1028–1032 (2013).
4. J. S. Kang, H. Wu, M. Li, Y. Hu, Intrinsic low thermal conductivity and phonon renormalization due to strong anharmonicity of single-crystal Tin selenide. *Nano Lett.* **19**, 4941–4948 (2019).
5. W. Li, S. Lin, M. Weiss, Z. Chen, J. Li, Y. Xu, W. G. Zeier, Y. Pei, Crystal structure induced ultralow lattice thermal conductivity in thermoelectric Ag_9AlSe_6 . *Adv. Energy Mater.* **8**, 1800030 (2018).
6. S. K. Saha, Exploring the origin of ultralow thermal conductivity in layered BiOCuSe . *Phys. Rev. B* **92**, 041202 (2015).
7. J. Yang, B. Zhang, A. D. Christodoulides, Q. Xu, A. Zangiabadi, S. R. Peurifoy, C. K. McGinn, L. Dai, E. Meirzadeh, X. Roy, M. L. Steigerwald, I. Kymissis, J. A. Malen, C. Nuckolls, Solution-processable superatomic thin-films. *J. Am. Chem. Soc.* **141**, 10967–10971 (2019).
8. B. Jiang, Y. Yu, J. Cui, X. Liu, L. Xie, J. Liao, Q. Zhang, Y. Huang, S. Ning, B. Jia, B. Zhu, S. Bai, L. Chen, S. J. Pennycook, J. He, High-entropy-stabilized chalcogenides with high thermoelectric performance. *Science* **371**, 830–834 (2021).
9. J. J. Kuo, M. Wood, T. J. Slade, M. G. Kanatzidis, G. J. Snyder, Systematic over-estimation of lattice thermal conductivity in materials with electrically-resistive grain boundaries. *Energ. Environ. Sci.* **13**, 1250–1258 (2020).
10. G. Chen, Size and interface effects on thermal conductivity of superlattices and periodic thin-film structures. *J. Heat Mass Transf.* **119**, 220–229 (1997).
11. W. Sun, A. Du, G. Gao, J. Shen, G. Wu, Graphene-templated carbon aerogels combining with ultra-high electrical conductivity and ultra-low thermal conductivity. *Microporous Mesoporous Mater.* **253**, 71–79 (2017).
12. L. Peng, Z. Xu, Z. Liu, Y. Guo, P. Li, C. Gao, Ultrahigh thermal conductive yet superflexible graphene films. *Adv. Mater.* **29**, 1700589 (2017).

13. G. Xin, T. Yao, H. Sun, S. M. Scott, D. Shao, G. Wang, J. Lian, Highly thermally conductive and mechanically strong graphene fibers. *Science* **349**, 1083–1087 (2015).
14. Y. Wang, Y. Chen, S. D. Lacey, L. Xu, H. Xie, T. Li, V. A. Danner, L. Hu, Reduced graphene oxide film with record-high conductivity and mobility. *Mater. Today* **21**, 186–192 (2018).
15. N. K. Mahanta, A. R. Abramson, M. L. Lake, D. J. Burton, J. C. Chang, H. K. Mayer, J. L. Ravine, Thermal conductivity of carbon nanofiber mats. *Carbon* **48**, 4457–4465 (2010).
16. L. C. Herrera-Ramírez, M. Cano, R. G. de Villoria, Low thermal and high electrical conductivity in hollow glass microspheres covered with carbon nanofiber-polymer composites. *Compos. Sci. Technol.* **151**, 211–218 (2017).
17. Y. Shang, Z. Liu, J. Dong, M. Yao, Z. Yang, Q. Li, C. Zhai, F. Shen, X. Hou, L. Wang, N. Zhang, W. Zhang, R. Fu, J. Ji, X. Zhang, H. Lin, Y. Fei, B. Sundqvist, W. Wang, B. Liu, Ultrahard bulk amorphous carbon from collapsed fullerene. *Nature* **599**, 599–604 (2021).
18. S.S. Roy, M.S. Arnold, Improving graphene diffusion barriers via stacking multiple layers and grain size engineering. *Adv. Funct. Mater.* **23**, 3638–3644 (2013).
19. S. Zhao, G. Siqueira, S. Drdova, D. Norris, C. Ubert, A. Bonnin, S. Galmarini, M. Ganobjak, Z. Pan, S. Brunner, G. Nyström, J. Wang, M. M. Koebel, W. J. Malfait, Additive manufacturing of silica aerogels. *Nature* **584**, 387–392 (2020).
20. X. Xu, Q. Zhang, M. Hao, Y. Hu, Z. Lin, L. Peng, T. Wang, X. Ren, C. Wang, Z. Zhao, C. Wan, H. Fei, L. Wang, J. Zhu, H. Sun, W. Chen, T. Du, B. Deng, G. J. Cheng, I. Shakir, C. Dames, T. S. Fisher, X. Zhang, H. Li, Y. Huang, X. Duan, Double-negative-index ceramic aerogels for thermal superinsulation. *Science* **363**, 723–727 (2019).
21. L. Su, H. Wang, M. Niu, S. Dai, Z. Cai, B. Yang, H. Huyan, X. Pan, Anisotropic and hierarchical SiC@SiO₂ nanowire aerogel with exceptional stiffness and stability for thermal superinsulation. *Sci. Adv.* **6**, eaay6689 (2020).
22. M. Biesuz, E. Zera, M. Tomasi, P. Jana, O. Ersen, W. Baaziz, A. Lindemann, G. D. Sorarù, Polymer-derived Si₃N₄ nanofelts for flexible, high temperature, lightweight and easy-manufacturable super-thermal insulators. *Appl. Mater. Today* **20**, 100648 (2020).
23. D. P. Anderson, Carbon fiber morphology. 2. Expanded wide-angle x-ray diffraction studies of carbon fibers. Wright-Patterson, Air Force Base, Dayton, Ohio (Accession Number: ADA235599), (1991).
24. L. F. B. Ribeiro, O. Flores, P. Furtat, C. Gervais, R. Kempe, R. A. F. Machado, G. Motz, A novel PAN/silazane hybrid polymer for processing of carbon-based fibres with extraordinary oxidation resistance. *J. Mater. Chem. A* **5**, 720–729 (2017).
25. E. Zussman, X. Chen, W. Ding, L. Calabri, D. A. Dikin, J. P. Quintana, R. S. Ruoff, Mechanical and structural characterization of electrospun PAN-derived carbon nanofibers. *Carbon*, **43**, 2175–2185 (2005).

26. S. Prilutsky, E. Zussman, Y. Cohen, The effect of embedded carbon nanotubes on the morphological evolution during the carbonization of poly (acrylonitrile) nanofibers. *Nanotechnology* **19**, 165603 (2008).
27. C. A. Klein, STB model and transport properties of pyrolytic graphites. *J. Appl. Phys.* **35**, 2947–2957 (1964).
28. A. Philipp, N.W. Pech-May, B. A. F. Kopera, A. M. Lechner, S. Rosenfeldt, M. Retsch, Direct measurement of the in-plane thermal diffusivity of semitransparent thin films by lock-in thermography: An extension of the slopes method. *Anal. Chem.* **91**, 8476–8483 (2019).
29. A. Mendioroz, R. Fuente-Dacal, E. Apiñaniz, A. Salazar, Thermal diffusivity measurements of thin plates and filaments using lock-in thermography. *Rev. Sci. Instrum.* **80**, 074904 (2009).
30. O. Philips'Gloeilampenfabrieken, A method of measuring specific resistivity and Hall effect of discs of arbitrary shape. *Philips Res. Rep.* **13**, 1–9 (1958).
31. D. Van Krevelen, K. Te Nijenhuis, “[Product properties (II) Environmental behaviour and failure]” in *Properties of Polymers*, (Elsevier, 2009), chap. 26. pp. 847–873.
32. X. Xu, Q. Zhang, Y. Yu, W. Chen, H. Hu, H. Li, Naturally dried graphene aerogels with superelasticity and tunable poisson's ratio. *Adv. Mater.* **28**, 9223–9230 (2016).
33. L. C. Herrera-Ramírez, M. Cano, R. G. de Villoria, Low thermal and high electrical conductivity in hollow glass microspheres covered with carbon nanofiber-polymer composites. *Compos. Sci. Technol.* **151**, 211–218 (2017).
34. Z. Fan, D. Z. Y. Tng, C. X. T. Lim, P. Liu, S. T. Nguyen, P. Xiao, A. Marconnet, C. Y. H. Lim, H. M. Duong, Thermal and electrical properties of graphene/carbon nanotube aerogels. *Colloids Surf. A Physicochem. Eng. Asp.* **445**, 48–53 (2014).
35. N. K. Mahanta, A. R. Abramson, M. L. Lake, D. J. Burton, J. C. Chang, H. K. Mayer, J. L. Ravine, Thermal conductivity of carbon nanofiber mats. *Carbon* **48**, 4457–4465 (2010).
36. X. Hou, R. Zhang, D. Fang, Superelastic, fatigue resistant and heat insulated carbon nanofiber aerogels for piezoresistive stress sensors. *Ceram. Int.* **46**, 2122–2127 (2020).
37. B. Wicklein, A. Kocjan, G. Salazar-Alvarez, F. Carosio, G. Camino, M. Antonietti, L. Bergström, Thermally insulating and fire-retardant lightweight anisotropic foams based on nanocellulose and graphene oxide. *Nat. Nanotechnol.* **10**, 277–283 (2015).
38. Y. Xie, S. Xu, Z. Xu, H. Wu, C. Deng, X. Wang, Interface-mediated extremely low thermal conductivity of graphene aerogel. *Carbon* **98**, 381–390 (2016).
39. Y. Lei, Z. Hu, B. Cao, X. Chen, H. Song, Enhancements of thermal insulation and mechanical property of silica aerogel monoliths by mixing graphene oxide. *Mater. Chem. Phys.* **187**, 183–190 (2017).
40. C. Yue, J. Feng, J. Feng, Y. Jiang, Efficient gaseous thermal insulation aerogels from 2-dimension nitrogen-doped graphene sheets. *Int. J. Heat Mass Transf.* **109**, 1026–1030 (2017).

41. Q. Peng, Y. Qin, X. Zhao, X. Sun, Q. Chen, F. Xu, Z. Lin, Y. Yuan, Y. Li, J. Li, W. Yin, C. Gao, F. Zhang, X. He, Y. Li, Superlight, mechanically flexible, thermally superinsulating, and antifrosting anisotropic nanocomposite foam based on hierarchical graphene oxide assembly. *ACS Appl. Mater. Interfaces* **9**, 44010–44017 (2017).
42. Y. Qin, Q. Peng, Y. Zhu, X. Zhao, Z. Lin, X. He, Y. Li, Lightweight, mechanically flexible and thermally superinsulating rGO/polyimide nanocomposite foam with an anisotropic microstructure. *Nanoscale Adv.* **1**, 4895–4903 (2019).
43. X. Lu, O. Nilsson, J. Fricke, R. W. Pekala, Thermal and electrical conductivity of monolithic carbon aerogels. *J. Appl. Phys.* **73**, 581–584 (1993).
44. Y. W. Chen, H. Zhan, J. N. Wang, A direct foaming approach for carbon nanotube aerogels with ultra-low thermal conductivity and high mechanical stability. *Nanoscale* **13**, 11878–11886 (2021).
45. M. J. Oh, J. H. Lee, P. J. Yoo, Graphene-based ultralight compartmentalized isotropic foams with an extremely low thermal conductivity of $5.75 \text{ mW m}^{-1} \text{ K}^{-1}$. *Adv. Funct. Mater.* **31**, 2007392 (2020).
46. X. Xu, Q. Zhang, M. Hao, Y. Hu, Z. Lin, L. Peng, T. Wang, X. Ren, C. Wang, Z. Zhao, C. Wan, H. Fei, L. Wang, J. Zhu, H. Sun, W. Chen, T. Du, B. Deng, G. J. Cheng, I. Shakir, C. Dames, T. S. Fisher, X. Zhang, H. Li, Y. Huang, X. Duan, Double-negative-index ceramic aerogels for thermal superinsulation. *Science* **363**, 723–727 (2019).
47. M. Biesuz, E. Zera, M. Tomasi, P. Jana, O. Ersen, W. Baaziz, A. Lindemann, G. D. Sorarù, Polymer-derived Si_3N_4 nanofelts for flexible, high temperature, lightweight and easy-manufacturable super-thermal insulators. *Appl. Mater. Today* **20**, 100648 (2020).
48. L. Su, H. Wang, M. Niu, S. Dai, Z. Cai, B. Yang, H. Huyan, X. Pan, Anisotropic and hierarchical $\text{SiC}@ \text{SiO}_2$ nanowire aerogel with exceptional stiffness and stability for thermal superinsulation. *Sci. Adv.* **6**, eaay6689 (2020).
49. S. Zhao, G. Siqueira, S. Drdova, D. Norris, C. Ubert, A. Bonnin, S. Galmarini, M. Ganobjak, Z. Pan, S. Brunner, G. Nyström, J. Wang, M. M. Koebel, W. J. Malfait, Additive manufacturing of silica aerogels. *Nature* **584**, 387–392 (2020).

5.2 Novel multifibrillar carbon and oxidation-stable carbon/ceramic hybrid fibers consisting of thousands of individual nanofibers with high tensile strength

www.nature.com/scientificreports

scientific reports



OPEN Novel multifibrillar carbon and oxidation-stable carbon/ceramic hybrid fibers consisting of thousands of individual nanofibers with high tensile strength

Jakob Denk¹, Xiaojian Liao^{2,✉}, Wolfgang Knolle⁴, Axel Kahnt⁴, Andreas Greiner², Stefan Schafföner¹, Seema Agarwal^{2,3,✉} & Günter Motz^{1,✉}

In this study, multifibrillar carbon and carbon/ceramic (C/SiCON) fibers consisting of thousands of single nanofibers are continuously manufactured. The process starts with electrospinning of polyacrylonitrile (PAN) and PAN/oligosilazane precursors resulting in poorly aligned polymer fibers. Subsequent stretching leads to parallel aligned multifibrillar fibers, which are continuously stabilized and pyrolyzed to C or C/SiCON hybrid fibers. The multifibrillar carbon fibers show a high tensile strength of 911 MPa and Young's modulus of 154 GPa, whereas the multifibrillar C/SiCON fibers initially have only tensile strengths of 407 MPa and Young's modulus of 77 GPa, due to sticking of the nanofibers during the stabilization in air. Additional curing with electron beam radiation, results in a remarkable increase in tensile strength of 707 MPa and Young's modulus of 98 GPa. The good mechanical properties are highlighted by the low linear density of the multifibrillar C/SiCON fibers (~ 1 tex) compared to conventional C and SiC fiber bundles (~ 200 tex). In combination with the large surface area of the fibers better mechanical properties of respective composites with a reduced fiber content can be achieved. In addition, the developed approach offers high potential to produce advanced endless multifibrillar carbon and C/SiCON nanofibers in an industrial scale.

Keywords Carbon fiber, Ceramic fiber, Electrospun multifibrillar fiber, Oligosilazane, High strength, Electron beam treatment

Carbon fibers are one of the most important technical fibers. They are indispensable in numerous technical applications, for example in aviation, automotive, military technology, aerospace, medical, and sport products^{1,2}. The commercial processing of these fibers is mostly performed by wet-spinning of polyacrylonitrile (PAN). Usually, PAN is dissolved in *N,N'*-dimethylformamide (DMF) or dimethyl sulfoxide (DMSO) and extruded into a precipitation bath, in which it is insoluble. The fibers obtained are then drawn, dried, and wound up^{1,3}. Afterwards, thermal stabilization is carried out under tensile stress at 200–300 °C in air. During this process, the linear macromolecules form a cyclic ladder-like structure^{4,5}. Then these stabilized fibers are carbonized at above 1000 °C in an inert atmosphere and are converted into carbon fibers. For high tensile carbon fibers, the pyrolysis occurs up to 1600 °C. High-modulus fibers are graphitized up to 3000 °C, whereby the tensile strength decreases^{6,7}.

Carbon fibers are interesting for many applications due to their extraordinary mechanical properties^{1,8}. For example, TORAY™ T1100 carbon fibers, achieve a tensile strength of 7 GPa at a low density of 1.79 g cm⁻³⁹. Despite these exceptional properties, commercial carbon fibers have only a fraction of the theoretical value.

¹Chair of Ceramic Materials Engineering, University of Bayreuth, 95440 Bayreuth, Germany. ²Macromolecular Chemistry 2 and Bavarian Polymer Institute, University of Bayreuth, 95440 Bayreuth, Germany. ³Bavarian Center for Battery Technology (BayBatt), University of Bayreuth, 95440 Bayreuth, Germany. ⁴Leibniz Institute of Surface Engineering (IOM), Permoserstr. 15, 04318 Leipzig, Germany. ✉email: xj_liao24@tju.edu.cn; Seema.Agarwal@uni-bayreuth.de; Guenter.Motz@uni-bayreuth.de

According to theoretical calculations, the tensile strength could be as high as 180 GPa^{10,11}. However, for multi-walled carbon nanotubes (CNTs) with diameters of 10 nm, a tensile strength of 150 GPa have already been determined, which is very close to the theoretical limit¹². Furthermore, for CNT fiber bundles, a tensile strength up to 80 GPa was reported¹³. The reason for these large differences in the theoretical and the measured tensile strength of fibers made from brittle materials like carbon and ceramics is, that only one defect leads to a catastrophic failure. A promising approach to reduce the probability for occurring defects in a defined fiber volume, is to reduce the diameter^{14,15}. This phenomenon was already described for glass fibers by Griffith in 1921¹⁶. Flores et al. reported similar effects for SiCN ceramic fibers made from melt-spun oligosilazanes (OSZ). For example, a tensile strength of 800 MPa was measured for fibers with diameters of 90 μm , but for the same fibers with a diameter of only 30 μm a tensile strength of 1600 MPa was achieved¹⁷.

A promising technique to produce fibers with strongly reduced diameters in the nanometer scale is electrospinning. During electrospinning a suitable polymer is dissolved in a solvent and pumped through a syringe, where the solution is charged because of the friction with the cannula and accelerated by an electric field. On its way to the collector, the solvent evaporates and fibers with a diameter of several hundred nanometers are obtained and deposited on a collector. Usually, a flat collector is used, to produce nonwovens¹⁸. In principle, this technique is suitable to process almost all soluble polymers¹⁹ and was used in the past for example for carbon and ceramic precursors like PAN^{19–22}, OSZ^{23,24} and siloxanes²⁵.

Previously our groups developed highly flexible electrospun C/SiCON nonwovens from polymer blends of PAN and the OSZ²⁶. In addition to extraordinary electrothermal properties, the nanofiber nonwovens were highly oxidation resistant. The reason for this combination of properties was the unique “sea-island” nanostructure where the ceramic interfaces protected the carbon from oxidation. However, this material has so far only been produced as nonwovens in which fibers were randomly laid onto each other. Because of their anisotropic structure fibers can withstand significantly higher loads in the direction of tension¹⁴. Spinning into parallel, continuous multifibrillar fibers, could therefore achieve significantly higher tensile strengths and enable textile applications, for example as reinforcing fibers.

Aligned fibers can be collected on a fast-rotating collector. This technique was used by different research groups for producing PAN fibers. Stretching and twisting of such aligned fibers followed by pyrolysis provided yarns with a tensile strength of up to 1.7 GPa^{27,28}. However, the length of the fiber bundles is limited by the diameter of the wheel, therefore only fibers with a length of several centimeters were obtained.

However, a novel electrospinning approach allows the processing of continuous multifibrillar fibers. In this method, the polymer solution is spun by two differently charged syringes and the nanofibers are caught by a rotating funnel and wound to a continuous multifibrillar fiber. Since the individual fibers are not perfectly aligned directly after spinning, the fibers are subsequently stretched by two rollers turning at different speeds^{29–32}. Extremely strong and tough multifibrillar polymer fibers were developed by additionally interconnecting the PAN nanofibers with polyethylene glycol (PEG) as a crosslinker via a click reaction³³. The fibers were highly entangled and unaligned directly after electrospinning (as-spun), but by subsequent heating and stretching over the glass transition temperature the fibers were stretched to an almost perfect alignment of 99.6%³¹. In another publication electrospun multifibrillar PAN fibers were stretched with different ratios. Afterwards short fiber segments with lengths of several centimeters were finally pyrolyzed to carbon fibers with tensile strengths of up to 1.1 GPa²⁹. However, a stabilization step or optimization of the pyrolysis towards a continuous process was not carried out. In principle, this approach is extremely promising for producing ceramic and carbon fibers with extraordinary mechanical properties. As discussed before, because of the Griffith principle,¹⁶ such fibers with smaller diameters should have higher tensile strengths. Additionally, because of the multifibrillar nature of these fibers, it is assumed that the failure of some single filaments due to defects would not lead to a catastrophic failure of the multifibrillar fiber, as illustrated in Fig. 1. SiC fiber rovings, for example, usually consist of 3000 individual fibers, each with a diameter between 5 and 10 μm ^{9,34}. Using electrospinning, it would be possible to produce multifibrillar fibers from thousands of nanofibers, which would mean a significant reduction in linear density and is very interesting for lightweight construction. Particularly for fiber-reinforced plastics, it is important that the fibers are bound to the matrix as strongly as possible so that the strength of the fibers can be transferred to the matrix. Due to the extremely large surface to volume ratio of the multifibrillar fibers, a decisive improvement could also be expected for this application. Another important aspect for high temperature applications is the already proven increased oxidation stability of C/SiCON compared to pure carbon. However, so far only short fibers^{35,36} or nonwovens³⁶ and no continuous multifibrillar fibers have been developed.

Therefore, the aim of this study was to create advanced, parallel aligned, continuous multifibrillar fibers with a high tensile strength composed of carbon and in particular of C/SiCON²⁴. In order to adjust our approach as close as possible to a commercial fiber production and achieve good mechanical properties, all manufacturing steps including spinning, thermal stabilization, and pyrolysis, were carried out in an optimized continuous process.

Experimental section

Materials

The polyacrylonitrile copolymer (PAN) was obtained from Dolan GmbH (Germany) (copolymer with max. 8% methyl acrylate and methylsulfonate according to the datasheet; number average molar mass (M_n) = 95,000; registration No. 26658–88–8). The oligosilazane Durazane 1800 (OSZ) was acquired from Merck (Germany). Dicumylperoxide (DCP) was ordered from Sigma-Aldrich (Germany). *N,N'*-dimethylformamide (DMF) 99.99% and 99.9% acetone were shipped from Thermo Fisher Scientific GmbH (Germany). All materials were used as received, without further purification.

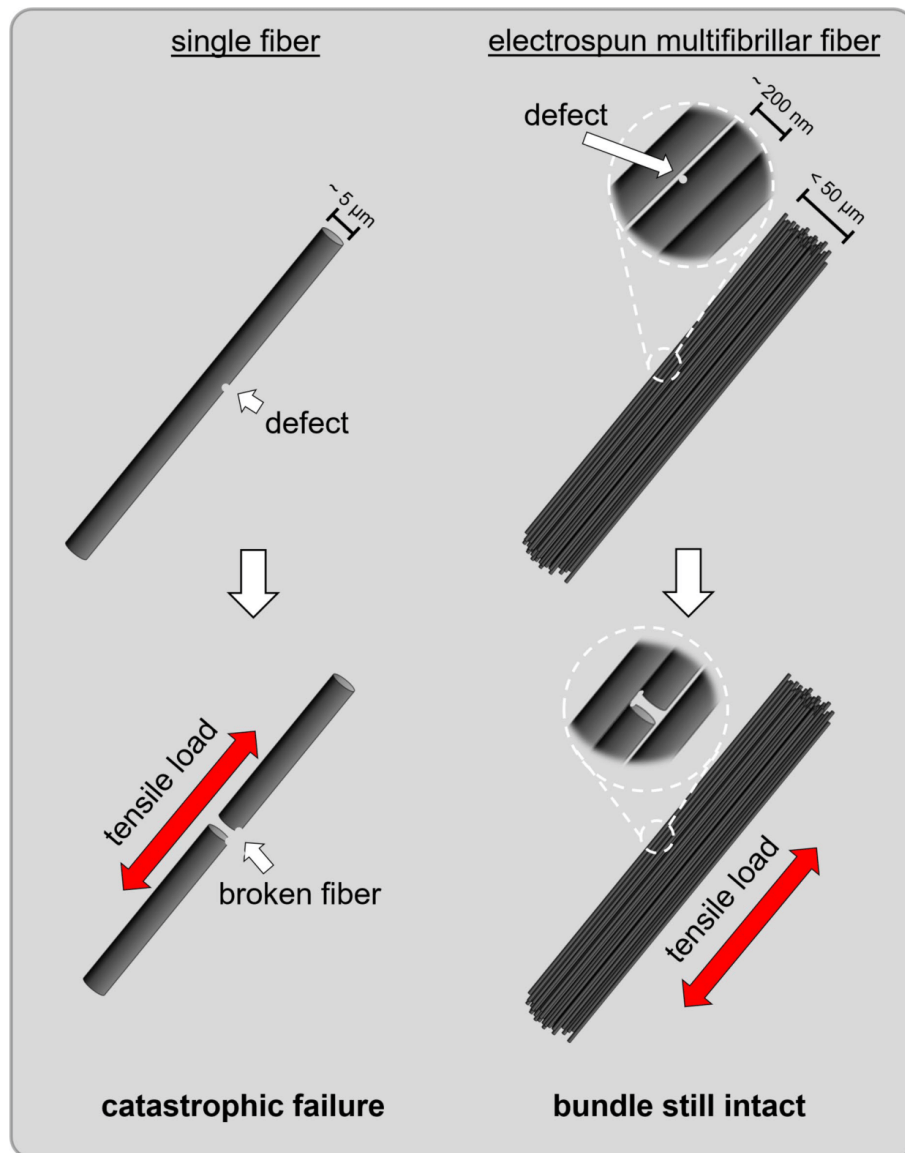


Figure 1. Schematic comparison of a defective single carbon or ceramic fiber with a multifibrillar fiber consisting of thousands of nanofibers. In contrast to the single fiber, the failure of one of the nanofibers under tensile load does not lead to the failure of the whole bundle.

Electrospinning and stretching of polymer fibers

Continuous yarns were obtained by yarn electrospinning following a procedure as published previously³³. The solution for electrospinning was prepared by dissolving PAN powder and the OSZ Durazane 1800 in DMF solution with acetone according to Table S2. The continuous yarns were fabricated using a homemade setup comprising two syringe pumps, a high-voltage DC power supply, a poly(vinyl chloride) (PVC) funnel (8.0 cm in diameter) with a motor controller and a yarn winder collector with 2 cm in diameter. The solution was loaded

into two syringes capped with metal needles, respectively (controllable feed rate of 0.5 mL h⁻¹ by two syringe pumps), which were connected separately to the positive and negative electrodes of the DC power supply. After adjusting the angle (13 degree of inclination), distance (40 cm) and altitude (perpendicular distance to the plane of the end of funnel: 2 cm) of these two syringes, high voltages (positive pole: +12 kV; negative pole: -12 kV) were applied to the two needle tips respectively, resulting in positively and negatively charged continuous fibrils. At first, by the force of electric field, these two oppositely charged fibrils flew to the end of the funnel with 1500 rpm rotation speed and a fibril membrane would be formed. Followed by switching on the winder collector of 13 rpm rotation speed, the membrane was dragged by a pre-suspended yarn which was connected with the winder collector. Then a rotodynamic fibril cone could be formed above the funnel. Simultaneously, helical form fibrils in the fibril cone were pulled up in a spiral path. Due to the cone maintained by the continuous helical form fibrils, a polymer yarn with continuous and twisted form was prepared from the apex of the fibril cone and wound around the collector. The whole electrospun yarn process was operated with 10–15% humidity.

Stabilization and pyrolysis to continuous C and C/SiCON fibers

For the continuous stabilization process eight fibers each were combined to a roving. The rovings were stabilized continuously under tension in air in a tubular furnace with three heating zones (Pyrolos AT). For the three stabilization runs, the furnace was programmed as follows:

I. 130–150–170 °C, II. 190–210–230 °C, III. 230–250–250 °C. Subsequently, the continuous pyrolysis was performed under tension at 1200 °C in N₂ atmosphere (Nabertherm RHTC 80-710/15, Germany). The gas flow rate was set to 250 ml min⁻¹. After pyrolysis the fibers were cut into smaller pieces for the analytical investigations.

Thermogravimetric analysis and differential scanning calorimetry

Thermogravimetric measurements were performed using a STA 449 F5 Jupiter system (Netzsch, Germany). For this purpose, 5 to 8 mg samples were placed in an Al₂O₃ crucible. The heating rate was fixed to 5 K min⁻¹ in air respectively nitrogen and the samples were heated to the respective maximum temperature. No hold time or special cooling rate was executed.

Scanning electron microscopy

For the SEM images a Zeiss Sigma 300 VP (Gemini, Germany) scanning electron microscope equipped with a field emission cathode, a secondary electron (SE2) and an InLens detector was used by an acceleration voltage of 3 kV and a working distance between 5 and 6 mm. Before the measurement small fiber samples were cut in liquid nitrogen. The pieces were fixed with a sample holder with a conductive double-sided carbon tape. The samples were subsequently sputter-coated with an 8 nm gold layer by a Cressington 108 auto sputter coater.

ATR-FTIR spectroscopy

For the ATR-FTIR analysis a Tensor 27 system (Bruker, Germany) equipped with an ATR unit with a diamond crystal was used. After a background measurement, the samples were ground to a fine powder with a mortar and pressed against the measuring diamond to receive a suitable signal. The measurements took place in a wavenumber range of 4000–400 cm⁻¹ at a resolution of 5 cm⁻¹. 32 measurements were averaged per sample to obtain higher signal-to-noise ratios. After the measurement, the received data were saved as a .csv file and plotted graphically using Origin 2022 software.

Raman spectroscopy

A combined Raman-imaging/scanning force microscope system (WITTEC ALPHA 300 RA +, Germany) with WiTec Control FIVE 5.3 software was used for RAMAN measurements. The laser is equipped with a UHTS 300 spectrometer combined with a back-illuminated Andor Newton 970 EMCCD camera (Resolution: ca. 300–400 nm (lateral) and 900 nm (z) with 100× objective). The measurements were carried out at an excitation wavelength of λ = 532 nm and a laser power of 1 mW with 50 accumulations with an integration time of 0.5 s pixel⁻¹. The samples were fixed on a glass slide with a tape. A slight stress was applied to prevent movement or vibration of the fiber. After adjusting the focus on the fibers at 100× magnification, the Raman spectrum was recorded. A cosmic ray removal and a baseline correction were applied for all spectra. The measured data were fitted with the GaussAmp function in Origin 2022.

Transmission electron microscopy

TEM measurements were performed by a JEM-2200FS TEM (JEOL Corporation, Japan) at an acceleration voltage of 200 kV. For the sample preparation a bundle of 5 to 10 fibers were glued together with EPO-TEK 375 epoxy glue (Epotek, Germany) and afterwards put into EPO-TEK 301 epoxy resin (Epotek, Germany). The embedded fibers were cut with ultramicrotomy (Leica, Germany) to thicknesses of 50 nm at room temperature.

Linear density

The linear density of the multifibrillar fibers (Table S3) were measured by weighing fiber bundles with a defined length and calculated by Eq. 1:

$$D = \frac{W}{L} \quad (1)$$

where the D is the linear density ($\text{tex} = \text{g km}^{-1}$), W is the weight and L is the length of the multifibrillar fibers. The weight of the C and C/SICON multifibrillar fibers with a length of 10–30 cm was measured by an ultramicro balance (Sartorius MSE2.7S-000-DM Cubis, capacity of 2.1 g, readability of 0.0001 mg, Germany).

Determination of the density

The densities (Table S4) were determined using a helium pycnometer AccuPyc II 1340 (micromeritics, USA) with a 1 cm³ sample cup. To obtain a sufficient sample mass, electrospun nonwovens were used for the density measurements. The preparation of nonwovens is explained in detail elsewhere²⁶. Between 0.02 and 0.04 g of each samples were used for the measurement. The mean value was calculated, from 10 measurements.

Single fiber tensile strength

The tensile strengths were determined using a tensile tester (zwickiLine Z0.5, BT1-FR0.5TN.D14, Zwick/Roell, Germany) with a clamping length of 10 mm, a crosshead rate of 5 mm min⁻¹ at 25 °C and a pre-tension of 0.001 N. The load cell was a Zwick/Roell KAF TC with a nominal load of 20 N. The fibers were glued to a paper frame according to german DIN1007 for single fibers tensile strength measurements (test length 25 mm). The multifibrillar fiber tensile tests were performed by a testing software belonging to the device for multifibrillar fiber shape cross-section calculation, while the linear density and density of the specimen material were input parameters. After the tensile test measurement, quantitative analysis of the tensile strength and Young's modulus was carried out by Origin 2022 software.

Electron beam treatment

An electron accelerator MB10-30MP (MeveX Corp., Stittsville, Canada) was used for electron beam treatment. The beam energy was 10 MeV and the total doses used were 300 – 1500 kGy. The dose was applied in partial steps of approximately 25 kGy to prevent heating of the samples over 60 °C. The nominal dose per path was determined by means of a calibrated graphite calorimeter. The polymer samples were sealed in a thin PVC-foil before irradiation. Samples were placed on an aluminum cooling block, kept at 35 °C operating temperature, to quickly dissipate the energy (heat) introduced by the irradiation. The fibers were wound onto a 10 mL syringe and a gentle nitrogen flow was adjusted through the inside and outside of the syringe to cool the sample during the treatment. The syringes were rotated by 90° after a quarter of total dose to account for differences in the dose depth profile and to ensure a homogeneous irradiation.

Gel fraction

To determine the gel fraction of the crosslinked polymers, PAN or the solution of PAN/OSZ-40 in DMF listed in Table S1 were dried under reduced pressure at 70 °C for four days. After the electron beam treatment with different doses, 0.30 g of each polymer sample was dissolved in DMF for two days. Finally, the insoluble amount was then removed by filtration, washed, dried and weighted. The gel fraction was determined according to Eq. 2:

$$G = \frac{m_2}{m_1} \cdot 100 \quad (2)$$

where G is the gel fraction in %, m_1 is the mass of the polymer before dissolution, and m_2 is the mass of the insoluble fraction after filtration.

Melting tests

0.2 g each of the polymer powders of PAN and crosslinked OSZ were pressed to pellets (1 cm radius) with 400 bar using a hydraulic hand press (Enerpac, USA) with an HPS-2 /0,7A hydraulic system (Yale, Germany) and self-made steel molds. The synthesis of the crosslinked Durazane 1800 is explained in detail elsewhere⁴⁰. The PAN/OSZ-40 pellets were prepared from the spinning solution in Table S2, poured into a glass mold, and dried in a vacuum drying oven at 70 °C for four days. Subsequently, the samples were treated with electron beam dose from 0 to 1000 kGy. Two samples were placed on top of each other, pressed together with a 200 g weight (~6200 Pa) and heated to 250 °C in air with a heating rate of 2 K min⁻¹. The experiments were performed at least three times each.

Results and Discussion

Processing of fibers

The electrospinning process of the multifibrillar fibers was carried out using a special electrospinning approach and has been described in detail before³³. For the preparation of the spinning solutions, PAN and the oligosilazane (OSZ) were dissolved in DMF and acetone. The solution was filled into two syringes, placed opposite to each other. Both solutions were continuously pumped from the syringes, one needle acted as a positive electrode, the other was negatively charged. A rotating funnel was located between the syringes, through which the spun nanofibers were collected and wound to a collector on the top. The aim was to produce multifibrillar fibers with the largest possible content of OSZ, since a larger proportion of OSZ leads to a better oxidation stability^{26,35,36}. For the electrospinning of multifibrillar fibers OSZ composition of 40 wt.%³³ was chosen, to ensure a stable spinning jet without fragmentation. For larger OSZ ratios, the jet kept splitting up and no continuous fiber was produced. Additionally, pure PAN fibers for the processing of multifibrillar carbon fibers were spun.

Since the individual fibers were initially largely disordered, they were stretched and oriented. This was achieved by two rollers rotating at different speeds at 160 °C. The schematics, photographs and SEM micrographs of the fibers before and after stretching are displayed in Fig. 2 a. The stretching process is essential to obtain an almost parallel fiber alignment with a high orientation of the roughly counted 3000 individual nanofibers.

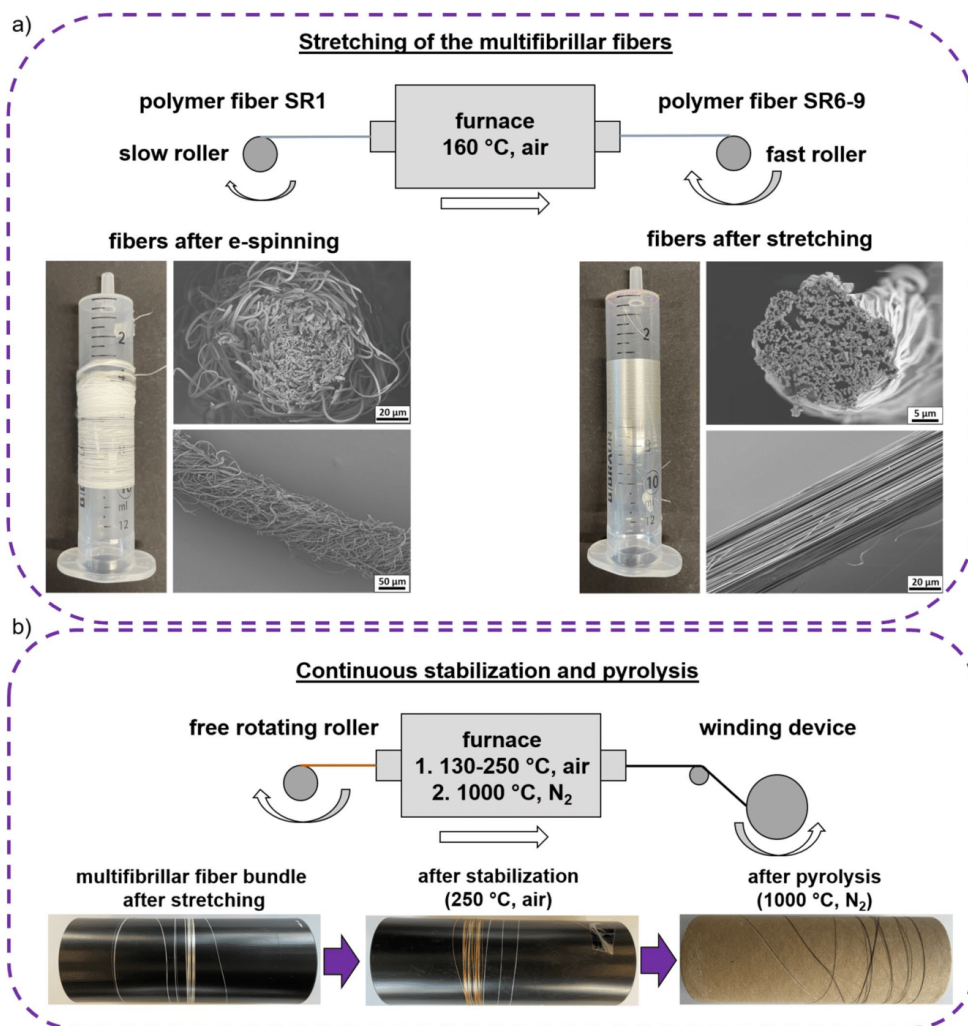


Figure 2. (a) Optical images and SEM micrographs of the stretching process of multifibrillar fibers from a disordered structure (SR1) to a highly aligned multifibrillar fiber (SR6-9). (b) Continuous oxidative stabilization at 250 °C in air and pyrolysis of the multifibrillar fibers at 1000 °C under N_2 -atmosphere.

Additionally, the stretching process led to reduced fiber diameters which should lead to better mechanical properties. Each multifibrillar fiber was stretched to the maximum stretch ratio (SR) without breaking. SR is defined as the length of stretched fibers divided by the length of the as-spun fibers (SR = 1 means unstretched). For pure PAN a maximum SR of 9 was achieved, whereas for fibers with 40 wt.% OSZ a SR of only 6 was reached (Fig. 2 a). A reason could be, that the OSZ was already partly crosslinked before or during the stretching process and therefore it was not possible to stretch as much. The resulting fibers are referred to as PAN or PAN/OSZ-40 in the polymer and C or C/SiCON-40 in the pyrolyzed state. The continuous stabilization and pyrolysis processes were optimized for PAN and PAN/OSZ-40 fibers. Therefore, 5 to 8 multifibrillar fiber bundles with lengths of 10 to 15 m were combined to a bundle. The stabilization (curing) step is crucial to obtain fibers that are mechanically and thermally stable enough to survive the subsequent pyrolysis without tearing. For the curing, the fibers were pulled through a tube furnace with three heating zones with a length of 30 cm each. The stabilization was performed in total in three runs from 130 to 250 °C. When the fibers were pulled through the furnace too quickly

or at a maximum temperature lower than 250 °C, the fiber bundles always ruptured either during the stabilization or in the subsequent pyrolysis step.

The continuous pyrolysis was carried out at 1000 °C by drawing the fiber bundle through a tube furnace under nitrogen atmosphere with a self-made drawing machine and a free rotating roller as presented in Fig. 2 b.

Investigation of the pyrolysis behaviour

The curing and the pyrolysis behavior were investigated in detail by differential scanning calorimetry (DSC) and thermogravimetric analysis (TGA). During the stabilization process in air, the linear PAN chains react to a ladder-like structure by dehydrogenation and cyclization reactions^{6,37,38}. These reactions are very exothermic leading to a strong signal in the DSC spectra for the two fiber types PAN and PAN/OSZ-40 (Fig. 3 a). Therefore, the heating rate during the stabilization process has to be very slow and should not exceed 250 °C, to prevent overheating of the fibers, which would lead to undesired reactions or damage the fibers³⁹. The mass loss of 1–2 wt.% was negligible for PAN and for PAN/OSZ-40 during the stabilization process up to 250 °C (Fig. 3 b). During the stabilization, the PAN crosslinks to a ladder-like structure, which is accelerated by oxygen^{1,3}. To further increase the degree of crosslinking and the yield of OSZ in the pyrolysis, dicumyl peroxide (DCP) was added to the OSZ as a radical initiator. DCP is known to start to crosslink OSZ at temperatures at 100 °C via vinyl polymerization and hydrosilylation during the stretching process, which avoids the release of volatile oligomers of the OSZ^{40–43}. The actual mass loss of PAN and OSZ only starts at higher temperatures during the pyrolysis process (Fig. 3 c). The yield in the TGA measurement was slightly higher for C/SiCON-40 (64 wt.%) than for the pure carbon fiber (53 wt.%). The ladder-like structure of the crosslinked PAN still contains a large amount of nitrogen, which is released by the formation of HCN and N₂ during the pyrolysis process between 200–1000 °C, leading to the formation of sp² hybridized carbon^{6,7}. The further crosslinking of the OSZ component occurs via dehydrocoupling and transamination reactions above 250 °C, with the release of H₂ and NH₃. In the range of 400–800 °C the precursor is transformed into an amorphous SiCON ceramic, by the formation of mainly H₂ and CH₄⁴². Thus, the PAN/OSZ-40 material, was converted to amorphous carbon and to an amorphous SiCON ceramic by the pyrolysis, resulting in a C/SiCON hybrid fiber²⁶.

Chemical characterization of the fibers

Investigations of the PAN with attenuated total reflectance-fourier-transformed infrared spectroscopy (ATR-FTIR) confirmed that during the stabilization up to 250 °C the C≡N (2245 cm⁻¹) groups were converted to C=N and C=C (1575 cm⁻¹) bonds by cyclization reactions as can be seen in Fig. 4 a^{1,8}. For the PAN/OSZ blend (Fig. 4 b), additionally N–H (3377 cm⁻¹), Si–H (2139 cm⁻¹), Si–CH₃ (1263 cm⁻¹) groups were detected belonging to the structure of the OSZ Durazane 1800 (Fig. S1). Since the silazane chains reacted with oxygen from air or were partially hydrolyzed from humidity in the air during the spinning process, additional Si–O–Si (1047 cm⁻¹) groups were also detected^{44,45}. The stabilization in air introduced more oxygen into the fiber which is clearly evident from the intensity increase in the Si–O–Si absorption band. Additionally, crosslinking reactions like hydrosilylation and dehydrocoupling proceeded in the OSZ, which is the reason for the less intensive Si–H and N–H absorption bands⁴². After pyrolysis, all organic groups disappeared and only Si–O–Si signals were detected for the C/SiCON-40 fibers. The Raman analysis delivered broad D and G bands with slightly higher I(D) to I(G) ratios of 1.06 for C/SiCON-40 fibers than for pure C with 0.94. This indicates a higher disordering of the carbon phase for C/SiCON-40 compared to pure C (Fig. 4 c and d). Transmission electron microscope (TEM) revealed that the microstructure of the C and C/SiCON-40 fibers consisted mainly of amorphous phases, confirmed also by the diffuse ring of the fast fourier-transformation (FFT) micrograph (Fig. 4 e). With higher magnifications some small graphitic carbon structures were also detected (Fig. 4 f). The mainly amorphous structure with free carbon phases was already described for similar materials after pyrolysis at temperatures of 1000 °C^{26,35,36}.

The analytical results agree well with previous studies from our groups for similar materials from electrospun nonwovens, which are chemically identical to the multifibrillar fibers presented here²⁶. The hybrid fibers in the nonwovens consisted of ceramic phases (SiO₂, SiC_xO_y, SiN_xO_y, and SiC_xN_y) in a carbon matrix. The X-ray diffraction (XRD) and Raman analysis revealed the typical signals of amorphous carbon in the pyrolyzed fibers as well. ¹³C and ²⁹Si solid state nuclear magnetic resonance (NMR) revealed the expected signals of sp² carbon and a

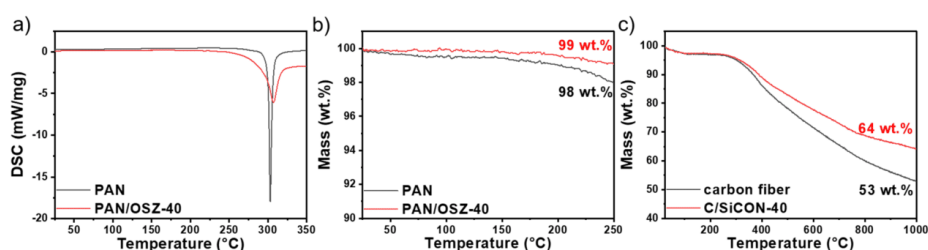


Figure 3. (a) DSC and (b) TGA measurements of PAN and PAN/OSZ-40 fibers during the stabilization process (heating rate 5 K min⁻¹, air). (c) TGA measurements of the stabilized PAN and PAN/OSZ fibers during the pyrolysis process to carbon and C/SiCON-40 fibers (heating rate 5 K min⁻¹, N₂).

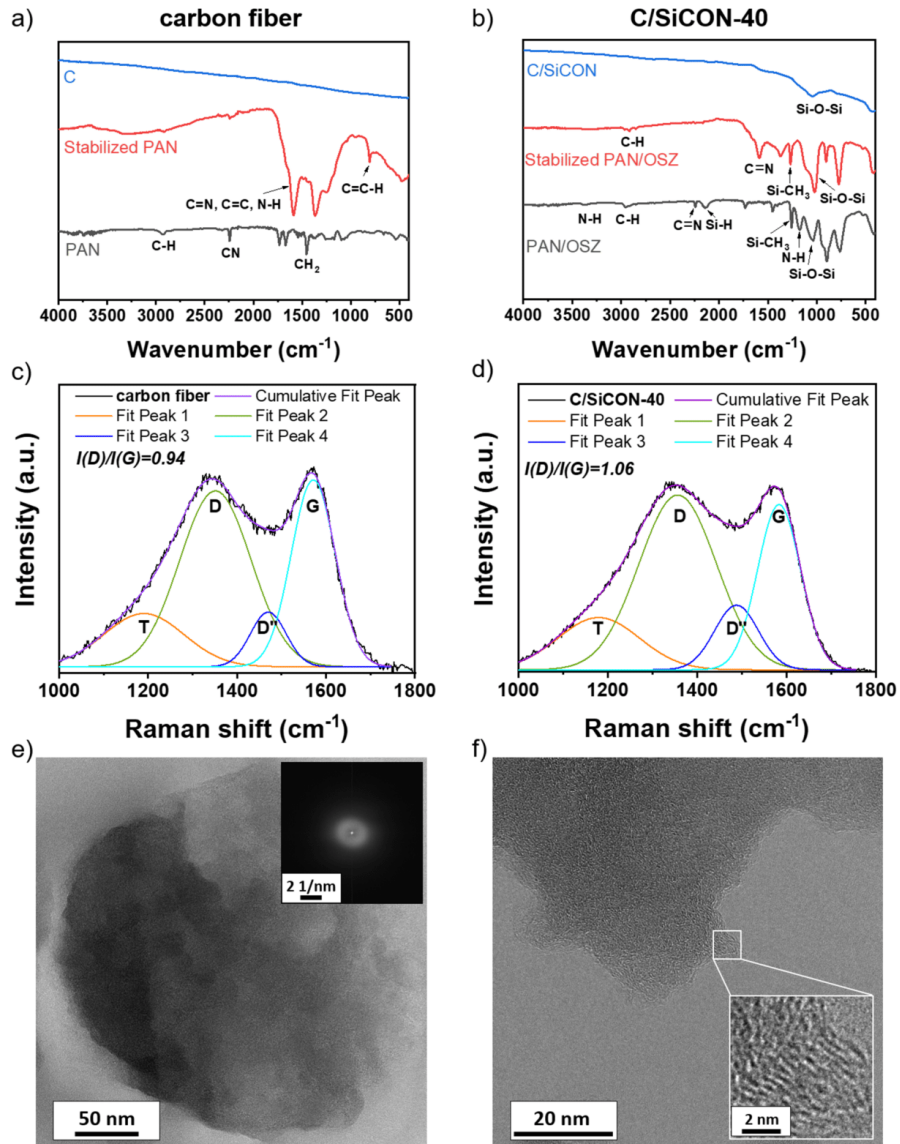


Figure 4. FTIR measurement from (a) carbon and (b) C/SiCON-40 multifibrillar fibers in the polymer, stabilized and pyrolyzed state. Raman analysis from (c) C and (d) C/SiCON-40 multifibrillar fibers in pyrolyzed state fitted with a Gaussian function and integrated area ratios²⁶. TEM micrographs of C/SiCON-40 multifibrillar fibers in pyrolyzed state showing (e) amorphous phases with the corresponding FFT and (f) higher magnifications with graphitic carbon structures (inset shows the magnified graphitic-like structure).

complex mixture of different SiO_4 , Si_xO_y , SiN_xO_y , and SiC_xN_y environments. The elemental analyses confirmed the presence of oxygen, which was introduced during the electrospinning and thermal stabilization in air.

Investigation of the mechanical properties

To investigate the mechanical properties of the multifibrillar carbon and C/SiCON-40 fibers, single fiber tensile tests were performed (Fig. 5). The determined tensile strength of the multifibrillar carbon fibers with values of 911 ± 132 MPa and a Young's modulus of 154 ± 50 GPa were much better than those of the C/SiCON-40 hybrid fibers with a tensile strength of 407 ± 73 MPa and a Young's modulus of 77 ± 17 MPa. A first reason for the lower tensile strength of C/SiCON-40 was the smaller SR of 6, compared to SR 9 for carbon fibers. Therefore, the C/SiCON-40 fibers were less oriented and stretched, which led also to thicker multifibrillar C/SiCON-40 fibers with diameters of 40.7 ± 3.1 μm in comparison to the respective carbon fibers with diameters of 21.0 ± 3.5 μm . Similarly, the C/SiCON-40 individual nanofibrils had a larger diameter of 333 ± 41 nm compared to 269 ± 35 nm for the carbon fibers.

In addition, the fiber surface of the hybrid fibers was slightly rippled (Fig. 6 f) and not as smooth as for the carbon fibers (Fig. 6 c). As already described, the OSZ crosslinks during the stretching process at 160 °C and is therefore not as stretchable as the still not crosslinked PAN, which leads to a bulging morphology of each nanofiber. However, such a rough, uneven fiber structure of the individual nanofibrils in the multifibrillar C/SiCON-40 fibers usually leads to a severe deterioration of the mechanical properties.

Another remarkable limitation of the tensile strengths of both fiber types is shown by analyzing the cross-section SEM micrographs of the multifibrillar fibers. The individual nanofibrils in the polymer state (Fig. 6 a and d) partly fused together during the stabilization process (Fig. 6 b and e). Due to the very large surface of the nanofibrils, the pressure on the fibers during stretching and their immediate contact, the softening of the PAN was sufficient for the fibers to stick together. Because of the described effect, many of the nanofibrils did not exist individually, which might have resulted in a total failure of the multifibrillar structure.

Electron beam treatment of the fibers

Different approaches were studied to prevent the softening of the PAN and the fusion of the individual fibers. In a first set of experiments, it was attempted to isolate the nanofibrils with a separating agent. For example, the fibers were extracted with a Soxhlet apparatus in acetone to remove residual DMF and afterwards impregnated with silicone oil (flash point > 315 °C) to act as a spacer between the individual nanofibrils during thermal stabilization step (Fig. S2).

Furthermore, the use of catalysts should reduce the crosslinking temperature to such an extent that the PAN does not soften during the thermal stabilization and thus the nanofibrils can be prevented from sticking together. Therefore, various salts from Sn⁴⁶⁻⁴⁹, Zn⁵⁰, Co⁵¹⁻⁵³, Cu^{49,54} and KMnO₄^{49,53,55} were added as catalysts, as already reported in literature. A positive effect was observed in DSC for SnCl₂ and ZnAc₂ (Table S1 and Fig. S3). But neither the use of separating agents nor catalytic crosslinking prevented the fusion of the fibers (Figs. S2 and S4) or led to improved tensile strengths as shown in Fig. S3.

A more promising approach to improve the mechanical properties by avoiding sticking of the nanofibrils was the crosslinking of the hybrid fibers by electron irradiation. This approach was reported for pure PAN fibers⁵⁶⁻⁵⁹ as well as for OSZ^{17,60} and is used commercially for polycarbosilanes during the production of ceramic SiC fibers of the second and third generation^{34,61-64}. The electron radiation leads to the formation of reactive radicals and functional groups in the polymer structure, which subsequently crosslinks with each other and consequently increases the degree of crosslinking of the polymers remarkably at low temperatures.

To investigate and compare the crosslinking behavior, both pure PAN and blends of PAN/OSZ-40 were treated with different doses of electron radiation from 0 to 1500 kGy. For this purpose, the samples were dissolved in DMF after the treatment, filtered, and the percentage ratio of the mass of the dried, insoluble fraction relative to the untreated polymer was determined (Fig. 7 a1 and b1). As expected, with higher irradiation doses a higher degree of crosslinking for all polymers was achieved. The crosslinked fraction for pure PAN increased slightly from 24 to 40% at irradiation doses from 200 to 600 kGy. The largest gain in crosslinking was detected

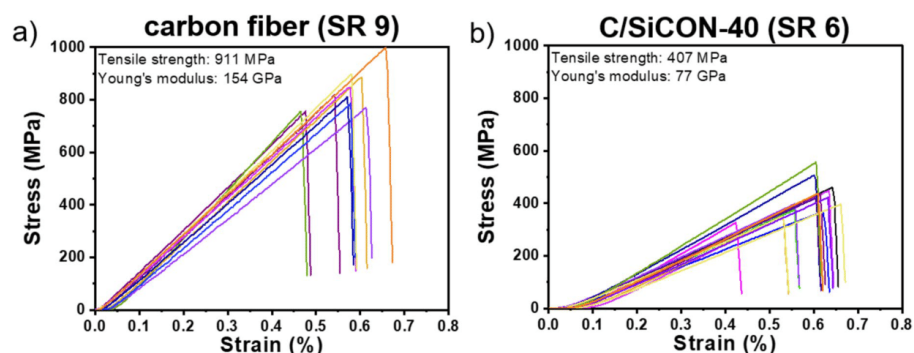


Figure 5. (a) Single fiber tensile tests of carbon multifibrillar fibers with a stretch ratio of 9. (b) Single fiber tensile tests of C/SiCON-40 multifibrillar fibers with a stretch ratio of 6.

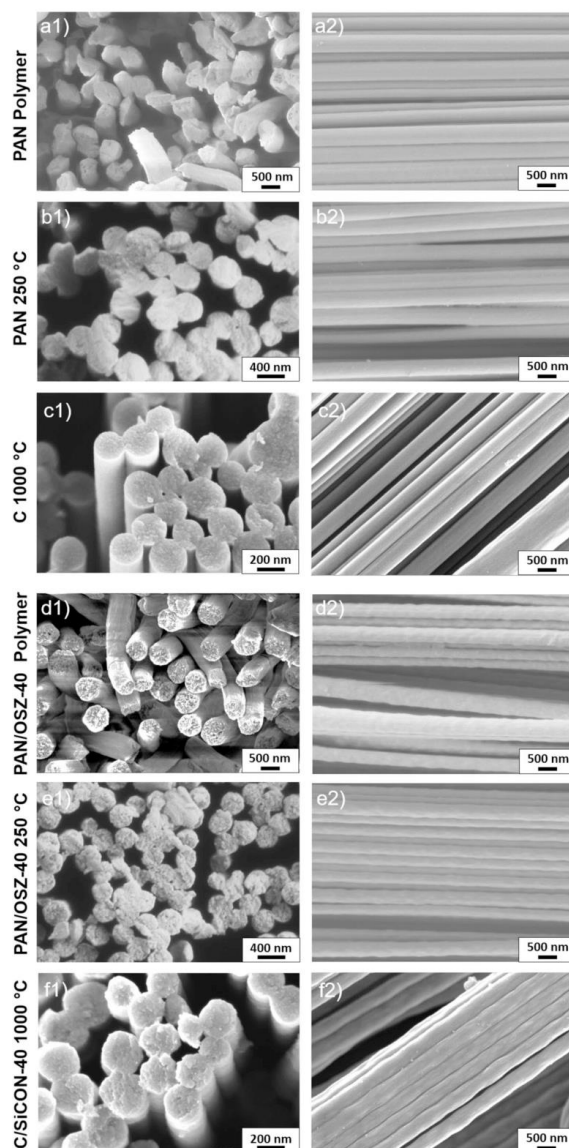


Figure 6. SEM micrographs of the PAN (a–c) and C/SiCON-40 (d–f) multifibrillar fibers in polymer condition, after stabilization at 250 °C and after pyrolysis at 1000 °C.

after the irradiation dose was raised to 800 kGy. After the treatment between 800 and 1500 kGy, the crosslinked fraction increased slower from 68 to 77%. For the PAN/OSZ-40 blends, a very high crosslinked fraction of 89% was determined already at a very low electron beam dose of 200 kGy. Above a dose of 400 kGy the polymer blend was almost completely crosslinked. The TGA measurements of the different PAN samples and PAN/OSZ blends (Fig. 7 a2 and b2) confirmed previous results that the ceramic yield, increased with the radiation dose⁶⁰.

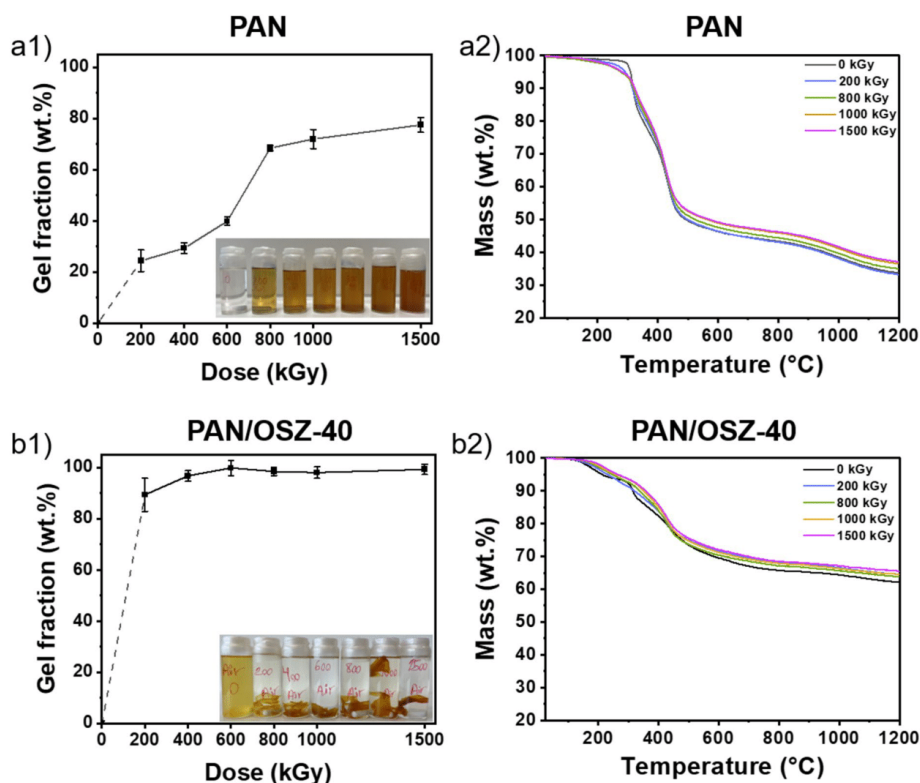


Figure 7. Gel fractions with optical images of the partly dissolved samples and TGA measurements (N_2 , 5 K min^{-1}) of (a) PAN and (b) PAN/OSZ-40 with different doses of electron beam treatment.

The reason for the increased yield is the additional crosslinking during irradiation, which reduced the amount of volatile oligomers.

In order to better understand the effects which led to the fusion of the nanofibers, pellets were pressed from powders of PAN and from catalytically polymerized OSZ (HTTS)⁴⁰ or cast from PAN/OSZ-40 solutions, respectively. The resulting pellets were initially treated with different electron beam doses, placed on top of each other, and heated up to $250\text{ }^\circ\text{C}$ in air according to the stabilization process of the fibers. As shown in Fig. 8, regardless of the electron beam treatment the pure PAN samples softened on the surface and stuck together. This is also clearly evident from the evaluation of the SEM micrographs of the cross-section. On the other hand, for polymerized OSZ (HTTS) melts, even electron beam treatment with low dose prevented sticking because of the high degree of crosslinking. As expected, the effect of electron irradiation on the crosslinking is therefore significantly higher for OSZ than for the pure PAN. The PAN/OSZ-40 pellets still fused together up to a radiation dose of 200 kGy, but this was no longer observed for higher doses.

Since the experiments to crosslink the polymers with electron irradiation were promising, the C and C/SiCON-40 multifibrillar fibers were treated with a high dose of 1000 kGy to ensure complete crosslinking. Afterwards the fibers were stabilized at $250\text{ }^\circ\text{C}$ and pyrolyzed at $1000\text{ }^\circ\text{C}$ as before. Despite the high electron beam dose, the SEM micrographs provided no evidence for damage of the PAN (Fig. S5) and PAN/OSZ-40 fibers (Fig. S6). But after further oxidative stabilization, the PAN fibers strongly fused together, whereas larger portions of the C/SiCON-40 fibers were found to be separated. Finally, the tensile strengths for the pyrolyzed electron beam treated multifibrillar carbon fibers (Fig. 9a) and the multifibrillar C/SiCON-40 fibers (Fig. 9 b) were determined and compared with the respective untreated fibers (Fig. 9 c and d). Because of the electron beam treatment, the tensile strength of the C/SiCON-40 fibers increased by 75% from $407 \pm 73\text{ MPa}$ to $707 \pm 80\text{ MPa}$. Moreover, the Young's modulus increased from $77 \pm 11\text{ GPa}$ to $103 \pm 10\text{ GPa}$ as well. In contrast, the electron beam curing of the carbon fibers, led to a strong decrease of 41% of the tensile strengths from $911 \pm 190\text{ MPa}$ to $536 \pm 85\text{ MPa}$. Thus, it can be concluded that the additional crosslinking was not sufficient to reduce the sticking of the multifibrillar carbon fibers. Additionally, treatment by electron irradiation results in either degradation or crosslinking

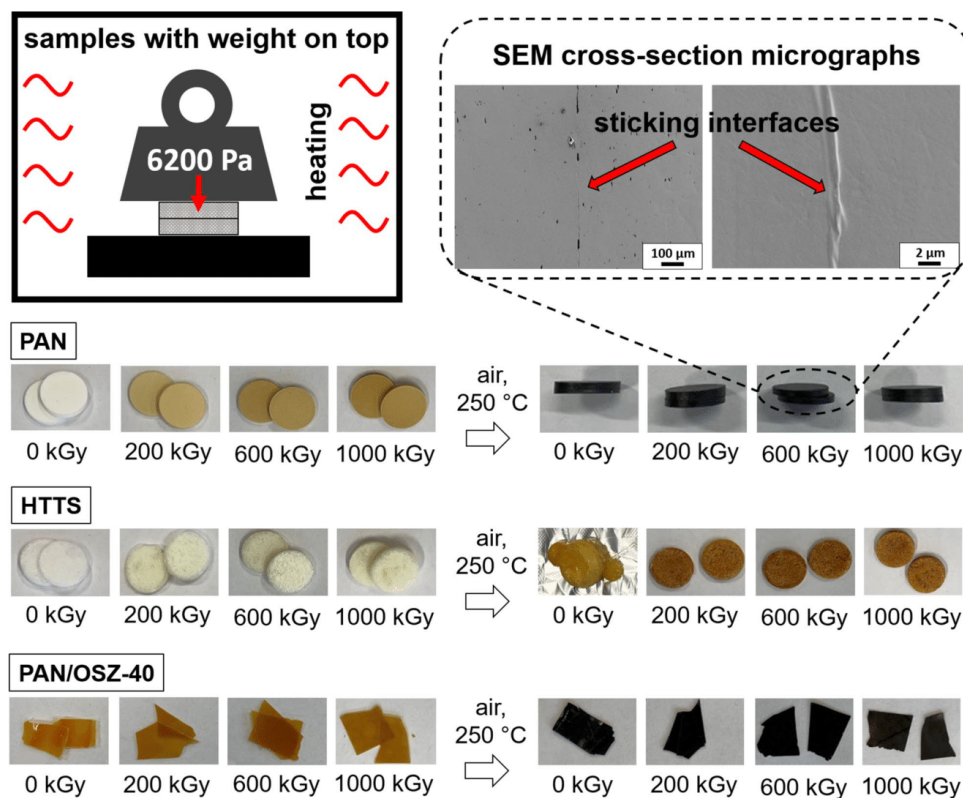


Figure 8. Schematic drawing of the sticking experiment of the irradiated polymer samples, and related optical images of the PAN, HTTS and PAN/OSZ-40 samples, treated with different doses of electron beam and SEM cross-section micrographs of the sticking PAN interfaces of the heated PAN samples.

of a polymer structure^{65–67}, and therefore it cannot be ruled out that defects are introduced into the fiber by the irradiation that led to a deterioration of the tensile strength.

Although the tensile strengths should be higher for the multifibrillar nanofibers due to the Griffith principle¹⁶ discussed before, the values are decreased by various factors. For example, even in the multifibrillar C/SiCON-40 fibers, sticking was only reduced, but not completely prevented. In addition, during the spinning process the fibers were collected and entangled by a rotating funnel as a collector³³. Due to the subsequent stretching, the fibers were aligned very well, but entanglements within the multifibrillar fibers were still very likely. These led to lateral shear forces, in the brittle ceramic fibers, and thus severely limited the tensile strengths. In addition, for the determined tensile strengths it must be considered that the multifibrillar fibers are comparable with fiber rovings and not with single fibers. Fiber rovings generally have a significantly lower tensile strength than single fibers^{68,69}. A first reason is friction between the individual fibers in the bundle, which is enhanced if weaker fibers break under low load, and additional friction occurs between the intact fibers and the fiber fragments^{68–70}. Moreover, the breakage of individual fibers in the bundle caused a sudden load on the neighboring intact fibers, which results in their breakage even if these fibers would have withstood a corresponding uniform load⁷¹. Because the individual fibers have diameters in the nanoscale, it was not possible to prepare single-fiber tensile tests, which are normally used for mechanical fiber tests.

Furthermore, the low weight expressed by the linear density of the multifibrillar fibers has to be considered for the mechanical properties. The corresponding tex value (g km^{-1}) of the multifibrillar carbon fibers was 0.33 tex and 1.04 tex for the multifibrillar C/SiCON-40 fibers. Commercial carbon fibers are in the order of 198 tex for rovings made of 3000 single fibers (TORAY T300 fibers)⁹ or ~200 tex for SiC ceramic rovings made of 1800 single fibers (Hi-Nicalon)⁷². The low inherent weight of the fibers in combination with the high values for tensile strengths shows the potential of the electrospun multifibrillar fibers. The unique combination of mechanical properties, the ability to produce these fibers continuously in an industrial process, and the previously published

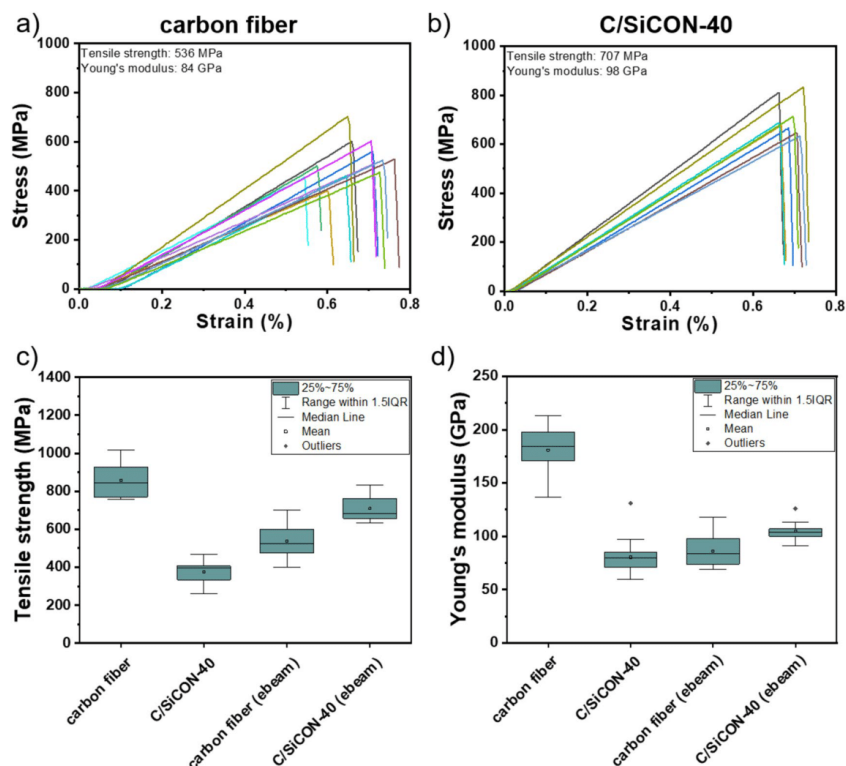


Figure 9. Single fiber tensile strength of (a) carbon multifibrillar fibers and (b) C/SiCON-40 multifibrillar fibers treated with an electron beam of a dose of 1000 kGy. Box-plots of the (c) tensile strengths and (d) Young's modulus of C and C/SiCON-40 multifibrillar fibers with and without electron beam treatment.

high oxidation stability of this material²⁶, makes this approach highly promising for an advanced carbon and ceramic fiber class. It offers potential applications in a wide range of uses.

Conclusions

In this work we presented for the first time continuous electrospun carbon and C/SiCON multifibrillar nanofibers, consisting of thousands of single filaments in the nanometer scale. The initially disordered polymer fibers were stretched almost perfectly to parallel aligned multifibrillar nanofibers. Subsequently, the fibers were continuously stabilized at 250 °C in air and pyrolyzed at 1000 °C in nitrogen atmosphere to carbon and ceramic C/SiCON nano-fibers, which consist of an amorphous carbon structure containing nano-scaled ceramic phases. Because of fiber sticking the tensile strength was only 407 MPa and the Young's modulus 77 GPa for the C/SiCON-40 multifibrillar fibers, whereas for the respective multifibrillar carbon fibers a higher tensile strength of 911 MPa and a Young's modulus of 154 GPa were determined. However, an additional electron beam treatment for the multifibrillar C/SiCON fibers led to a significant increase in both in the tensile strength up to 707 MPa and in the Young's modulus up to 103 GPa. In contrast, for the pure carbon the tensile strength decreased to 536 MPa and the Young's modulus to 98 GPa fibers probably due to the generation of defects within the fiber structure during irradiation.

Considering the low linear density of the multifibrillar C/SiCON nanofibers (~ 1 tex) compared to conventional C and SiC fiber bundles (~ 200 tex), the high mechanical properties of the fibers become evident. Since all steps were carried out in a continuous approach, this method can be extended and applied to any fiber length and is suitable for an industrial scale and setup. Because of the high tensile strength in combination with the low inherent weight, the extremely large surface to volume ratio and the already shown flame stability (C/SiCON) the multifibrillar fibers are of high interest as reinforcing component for example in the field of advanced fiber-reinforced plastics. In addition, the high-temperature and oxidation stability (C/SiCON) demonstrated in previous studies also enables use in composite materials for high temperature applications with carbon and ceramics

as a matrix. The future research activities are focused on further improving the processing of the multifibrillar fibers to obtain significantly better mechanical properties.

Data availability

The datasets used and/or analyzed during the current study available from the corresponding author on reasonable request.

Received: 15 May 2024; Accepted: 29 July 2024

Published online: 05 August 2024

References

- Frank, E., Steudle, L. M., Ingildeev, D., Spörl, J. M. & Buchmeiser, M. R. Carbon fibers: Precursor systems, processing, structure, and properties. *Angew. Chem. Int. Ed.* **53**, 5262 (2014).
- Chand, S. Carbon fibers for composites. *J. Mater. Sci.* **35**(6), 1303 (2000).
- Morgan, P. *Carbon Fibers and Their Composites* (CRC Press, Boca Raton, 2005).
- Liao, X. *et al.* Polyacrylonitrile-derived polyconjugated ladder structures for high performance all-organic dielectric materials. *Chem. Commun.* **51**, 10127 (2015).
- Sánchez-Soto, P. J. *et al.* Thermal study of the effect of several solvents on polymerization of acrylonitrile and their subsequent pyrolysis. *J. Anal. Appl. Pyrolysis* **58**, 155 (2001).
- Frank, E., Hermanutz, F. & Buchmeiser, M. R. Carbon fibers: Precursors, manufacturing, and properties. *Macromol. Mater. Eng.* **297**, 493 (2012).
- Frank, E., Steudle, L. M., Ingildeev, D., Spörl, J. M. & Buchmeiser, M. R. Carbon fibers: Precursor systems, processing, structure, and properties. *Angew. Chem. Int. Ed.* **53**, 5262 (2014).
- Rahaman, M. S. A., Ismail, A. F. & Mustafa, A. A review of heat treatment on polyacrylonitrile fiber. *Polym. Degrad. Stab.* **92**, 1421 (2007).
- TORAYCA* Carbon Fiber | Toray Composite Materials America. **2023**. <https://www.toraycma.com/products/carbon-fiber/>. Accessed 30 Mar 2023
- Fitzer, E. *Carbon Fibers and Their Composites* (Springer, Berlin, 1985).
- Donnet, J. B. & Chaneé Bansal, R. *Carbon Fibers* 3rd edn. (CRC Press, Boca Raton, 1998).
- Demczyk, B. G. *et al.* Direct mechanical measurement of the tensile strength and elastic modulus of multiwalled carbon nanotubes. *Mater. Sci. Eng. A* **334**, 173 (2002).
- Bai, Y. *et al.* Carbon nanotube bundles with tensile strength over 80 GPa. *Nat. Nanotechnol.* **13**, 589 (2018).
- Jang, D., Lee, M. E., Choi, J., Cho, S. Y. & Lee, S. Strategies for the production of PAN-based carbon fibers with high tensile strength. *Carbon* **186**, 644 (2022).
- Danzer, R. Some notes on the correlation between fracture and defect statistics: Are Weibull statistics valid for very small specimens? *J. Eur. Ceram. Soc.* **26**, 3043 (2006).
- Griffith, A. A. VI. The phenomena of rupture and flow in solids. *Philos. Trans. R Soc. Lond.* **221**, 163 (1921).
- Flores, O. *et al.* Processing and characterization of large diameter ceramic sicc monofilaments from commercial oligosilazanes. *RSC Adv.* **5**, 107001 (2015).
- Wendorff, J. H., Agarwal, S. & Greiner, A. *Electrospinning Materials, Processing and Applications* (Wiley, Weinheim, 2008).
- Shin, E. H., Cho, K. S., Seo, M. H. & Kim, H. Determination of electrospun fiber diameter distributions using image analysis processing. *Macromol. Res.* **16**, 314 (2008).
- Wang, T. & Kumar, S. Electrospinning of polyacrylonitrile nanofibers. *J. Appl. Polym. Sci.* **102**, 1023 (2006).
- Nataraj, S. K., Yang, K. S. & Aminabhavi, T. M. Polyacrylonitrile-based nanofibers—a state-of-the-art review. *Prog. Polym. Sci.* **37**, 487 (2012).
- Inagaki, M., Yang, Y. & Kang, F. Carbon nanofibers prepared via electrospinning. *Adv. Mat.* **24**, 2547 (2012).
- Ramlow, H., Marangoni, C., Motz, G. & Machado, R. A. F. Statistical optimization of polysilazane-derived ceramic: Electrospinning with and without organic polymer as a spinning aid for manufacturing thinner fibers. *Chem. Eng. J. Adv.* **9**, 100220 (2022).
- Ribeiro, L. F. B. *et al.* Flexible and porous nonwoven SiCN ceramic material via electrospinning of an optimized silazane solution. *Adv. Eng. Mater.* **24**, 2100321 (2022).
- Ren, Z., Gervais, C. & Singh, G. Fabrication and characterization of silicon oxycarbide fibre-mats: Via electrospinning for high temperature applications. *RSC Adv.* **10**, 38446 (2020).
- Liao X, Denk J, Tran, T, Miyajima N, Benker L, Rosenfeldt S, Schafföner S, Retsch M, Greiner A, Motz G, Agarwal S. Extremely low thermal conductivity and high electrical conductivity of sustainable carbon ceramic electrospun nonwoven materials. *Sci. Adv.* **9** (2023).
- Zhou, Z. *et al.* Development of carbon nanofibers from aligned electrospun polyacrylonitrile nanofiber bundles and characterization of their microstructural, electrical, and mechanical properties. *Polymer (Guildf)* **50**, 2999 (2009).
- Moon, S. C. & Farris, R. J. Strong electrospun nanometer-diameter polyacrylonitrile carbon fiber yarns. *Carbon N Y* **47**, 2829 (2009).
- Xie, Z., Niu, H. & Lin, T. Continuous polyacrylonitrile nanofiber yarns: Preparation and dry-drawing treatment for carbon nanofiber production. *RSC Adv.* **5**, 15147 (2015).
- Ali, U., Zhou, Y., Wang, X. & Lin, T. Direct electrospinning of highly twisted, continuous nanofiber yarns. *J. Text. Inst.* **103**, 80 (2012).
- Pan, H., Li, L., Hu, L. & Cui, X. Continuous aligned polymer fibers produced by a modified electrospinning method. *Polymer (Guildf)* **47**, 4901 (2006).
- O'Connor, R. A. & McGuinness, G. B. Electrospun nanofiber bundles and yarns for tissue engineering applications: A review. *Proc. Inst. Mech. Eng. H* **230**, 987 (2016).
- Liao, X. *et al.* High strength in combination with high toughness in robust and sustainable polymeric materials. *Science* **1979** **366**, 1376 (2019).
- Flores, O., Bordia, R. K., Nestler, D., Krenkel, W. & Motz, G. Ceramic Fibers based on SiC and SiCN systems: Current research, development, and commercial status. *Adv. Eng. Mater.* **16**, 621 (2014).
- Ribeiro, L. *et al.* The influence of pyrolysis temperature on the oxidation resistance of carbon-rich SiCN ceramics derived from reaction of silazanes with acrylonitrile. *J. Eur. Ceram. Soc.* **41**, 3285 (2021).
- Ribeiro, L. F. B. *et al.* A novel PAN/silazane hybrid polymer for processing of carbon-based fibres with extraordinary oxidation resistance. *J. Mater. Chem. A Mater.* **5**, 720 (2017).
- Dalton, S., Heatley, F. & Budd, P. M. Thermal stabilization of polyacrylonitrile fibres. *Polymer (Guildf)* **40**, 5531 (1999).
- Wen, Q., Yu, Z. & Riedal, R. The fate and role of in situ formed carbon in polymer-derived ceramics. *Prog. Mater. Sci.* **109**, 100623 (2020).

39. Meinel, J. *et al.* Optimization of the temperature program to scale up the stabilization of polyacrylonitrile fibers. *Compos. Part A Appl. Sci. Manuf.* **96**, 37 (2017).
40. Flores, O., Schmalz, T., Krenkel, W., Heymann, L. & Motz, G. Selective cross-linking of oligosilazanes to tailored meltable polysilazanes for the processing of ceramic SiCN fibres. *J. Mater. Chem. A Mater.* **1**, 15406 (2013).
41. D'Elia, R. *et al.* Effect of dicumyl peroxide concentration on the polymerization kinetics of a polysilazane system. *Polym. Eng. Sci.* **58**, 859 (2018).
42. Traßl, S., Suttor, D., Motz, G., Rössler, E. & Ziegler, G. Structural characterisation of silicon carbonitride ceramics derived from polymeric precursors. *J. Eur. Ceram. Soc.* **20**, 215 (2000).
43. Ziegler, G. *et al.* Synthesis, microstructure and properties of SiCN ceramics prepared from tailored polymers. *Mater. Chem. Phys.* **61**, 55 (1999).
44. Müller, S., de Hazan, Y. & Penner, D. Effect of temperature, humidity and aminoalkoxysilane additive on the low temperature curing of polyorganosilazane coatings studied by ir spectroscopy, gravimetric and evolved gas analysis. *Prog. Org. Coat.* **97**, 133 (2016).
45. Zhan, Y., Grottenmüller, R., Li, W., Javadi, F. & Riedel, R. Evaluation of mechanical properties and hydrophobicity of room-temperature, moisture-curable polysilazane coatings. *J. Appl. Polym. Sci.* **138**, 50469 (2021).
46. Chen, J., Wang, C. G., Dong, X. G. & Liu, H. Z. Study on the coagulation mechanism of wet-spinning PAN fibers. *J. Polym. Res.* **13**, 515 (2006).
47. Zhang, S., Liu, H., Yu, J., Li, B. & Ding, B. Multi-functional flexible 2D carbon nanostructured networks. *Nat. Commun.* **11**, 5134 (2020).
48. Shiedlin, A., Marom, G. & Zilkha, A. Catalytic initiation of polyacrylonitrile stabilization. *Polymer (Guildf)* **26**, 447 (1985).
49. Mittal, J. & Mathur, R. B. Post spinning modification: A review of pan fibres. *Science* **1997**, 35 (1979).
50. Chen, R. *et al.* Facile fabrication of foldable electrospun polyacrylonitrile-based carbon nanofibers for flexible lithium-ion batteries. *J. Mater. Chem. A Mater.* **5**, 12914 (2017).
51. Ko, T. H. & Huang, L. C. The influence of cobaltous chloride modification on physical properties and microstructure of modified PAN fiber during carbonization. *J. Appl. Polym. Sci.* **70**, 2409 (1998).
52. Zhang, W. X. & Wang, Y. Z. Manufacture of carbon fibers from polyacrylonitrile precursors treated with CoSO₄. *J. Appl. Polym. Sci.* **85**, 153 (2002).
53. Yusof, N. & Ismail, A. F. Post spinning and pyrolysis processes of polyacrylonitrile (PAN)-based carbon fiber and activated carbon fiber: A review. *J. Anal. Appl. Pyrol.* **93**, 1 (2012).
54. Mathur, R. B., Gupta, D., Bahl, O. P. & Dhami, T. L. Infrared spectral studies of preoxidized PAN fibres incorporated with cuprous chloride additive. *J. Fiber. Sci.* **20**, 227 (1984).
55. Li, X. & Dang, X. Effect of potassium permanganate modification on plasticized spinning polyacrylonitrile fibers with different diameters. *Polymers (Basel)* **10**, 1330 (2018).
56. Shin, H. K., Park, M., Kim, H. Y. & Park, S. J. An overview of new oxidation methods for polyacrylonitrile-based carbon fibers. *Carbon Lett.* **16**, 11 (2015).
57. Shin, H. K., Park, M., Kang, P. H., Choi, H. S. & Park, S. J. *J. Ind. Eng. Chem.* **20**, 3789 (2014).
58. Park, S. *et al.* Comprehensive stabilization mechanism of electron-beam irradiated polyacrylonitrile fibers to shorten the conventional thermal treatment. *Sci. Rep.* **6**, 1 (2016).
59. König, S. *et al.* High-performance carbon fibers prepared by continuous stabilization and carbonization of electron beam-irradiated textile grade polyacrylonitrile fibers. *Macromol. Mater. Eng.* **306**, 2100484 (2021).
60. Kokott, S. & Motz, G. Cross-Linking via electron beam treatment of a tailored polysilazane (ABSE) for processing of ceramic SiCN-Fibers. *Soft. Mater.* **4**, 165 (2007).
61. Bunsell, A. R. & Piant, A. A review of the development of three generations of small diameter silicon carbide fibres. *J. Mater. Sci.* **41**, 823 (2006).
62. Ichikawa, H. Development of high performance SiC fibers derived from polycarbosilane using electron beam irradiation curing-a review. *J. Ceram. Soc. Jpn.* **114**, 455 (2006).
63. Ishikawa, T. Advances in inorganic fibers. *Adv. Polym. Sci.* **178**, 109 (2005).
64. Schawaller, D., Clauß, B. & Buchmeiser, M. R. Ceramic filament fibers: A review. *Macromol. Mater. Eng.* **297**, 502 (2012).
65. Dawes, K., Glover, L. C. & Vroom, D. A. *Physical Properties of Polymers Handbook* (Springer, Berlin, 2007).
66. Sezen, M. *et al.* An Investigation on focused electron/ion beam induced degradation mechanisms of conjugated polymers. *Phys. Chem. Chem. Phys.* **13**, 20235 (2011).
67. Drobny, J. G. *Radiation Technology for Polymers* (CRC Press, Boca Raton, 2020).
68. Callaway, E. B. & Zok, F. W. Strengths of ceramic fiber bundles: Theory and practice. *J. Am. Ceram. Soc.* **100**, 5306 (2017).
69. Calard, V. & Lamon, J. Failure of fiber bundles. *Compos. Sci. Technol.* **64**, 701 (2004).
70. Hill, R. & Okoroafor, E. U. Weibull statistics of fibre bundle failure using mechanical and acoustic emission testing: The Influence of interfibre friction. *Composites* **26**, 699 (1995).
71. Chi, Z., Chou, T. W. & Shen, G. Determination of single fibre strength distribution from fibre bundle testings. *J. Mater. Sci.* **19**, 3319 (1984).
72. Nicalon SiC Fiber - COI Ceramics. 2023. <https://www.coiceramics.com/technology/fiber/nicalon.html>. Accessed 30 Mar 2023.

Acknowledgements

We thank L. Benker for the Raman measurements. M. Schwarzmann and M. Drechsler for the TEM measurements. The work was supported by the University of Bayreuth and the Deutsche Forschungsgemeinschaft (DFG). A.G. and G.M. would like to thank DFG (Deutsche Forschungsgemeinschaft) for the financial support (GR 972/61-1 and MO 851/21-1 (455984818)).

Author contributions

J. D., X. L., A.G., G.M., and S.A. proposed the idea and designed the experiments. J. D., and X. L. conducted preparation of the fibers and characterization. W.K and A.K carried out the electron beam treatment. All authors contributed to the discussion of the data. The first draft of the manuscript was written by J.D. all other authors provided valuable input.

Funding

Open Access funding enabled and organized by Projekt DEAL.

Competing interests

The authors declare no competing interests.

Additional information

Supplementary Information The online version contains supplementary material available at <https://doi.org/10.1038/s41598-024-68794-w>.

Correspondence and requests for materials should be addressed to X.L., S.A. or G.M.

Reprints and permissions information is available at www.nature.com/reprints.

Publisher's note Springer Nature remains neutral with regard to jurisdictional claims in published maps and institutional affiliations.

Open Access This article is licensed under a Creative Commons Attribution 4.0 International License, which permits use, sharing, adaptation, distribution and reproduction in any medium or format, as long as you give appropriate credit to the original author(s) and the source, provide a link to the Creative Commons licence, and indicate if changes were made. The images or other third party material in this article are included in the article's Creative Commons licence, unless indicated otherwise in a credit line to the material. If material is not included in the article's Creative Commons licence and your intended use is not permitted by statutory regulation or exceeds the permitted use, you will need to obtain permission directly from the copyright holder. To view a copy of this licence, visit <http://creativecommons.org/licenses/by/4.0/>.

© The Author(s) 2024

Novel multifibrillar carbon and oxidation-stable carbon/ceramic hybrid fibers consisting of thousands of individual nanofibers with high tensile strength

Jakob Denk,^a Xiaojian Liao,^{b,*} Wolfgang Knolle,^d Axel Kahnt,^d Andreas Greiner,^b Stefan Schafföner,^a Seema Agarwal,^{b,c,*} and Günter Motz^{a,*}

a Chair of Ceramic Materials Engineering, University of Bayreuth, Bayreuth 95440, Germany.

b Macromolecular Chemistry 2 and Bavarian Polymer Institute, University of Bayreuth, Bayreuth 95440, Germany

c Bavarian Center for Battery Technology (BayBatt), University of Bayreuth, Bayreuth 95440, Germany

d Leibniz Institute of Surface Engineering (IOM), Permoserstr. 15, 04318 Leipzig, Germany

* Corresponding author. E-mail address: Guenter.Motz@uni-bayreuth.de (Günter Motz); Seema.Agarwal@uni-bayreuth.de (Seema Agarwal); xj_liao24@tju.edu.cn (Xiaojian Liao)

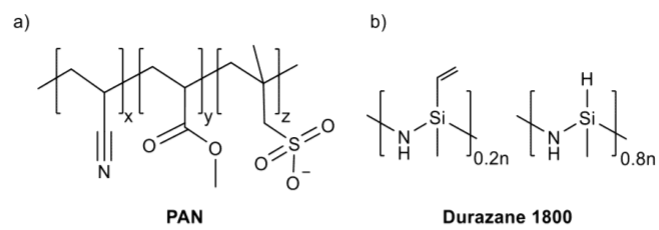


Fig. S1 Chemical structure of Polyacrylonitrile PAN and the oligosilazane Durazane 1800.

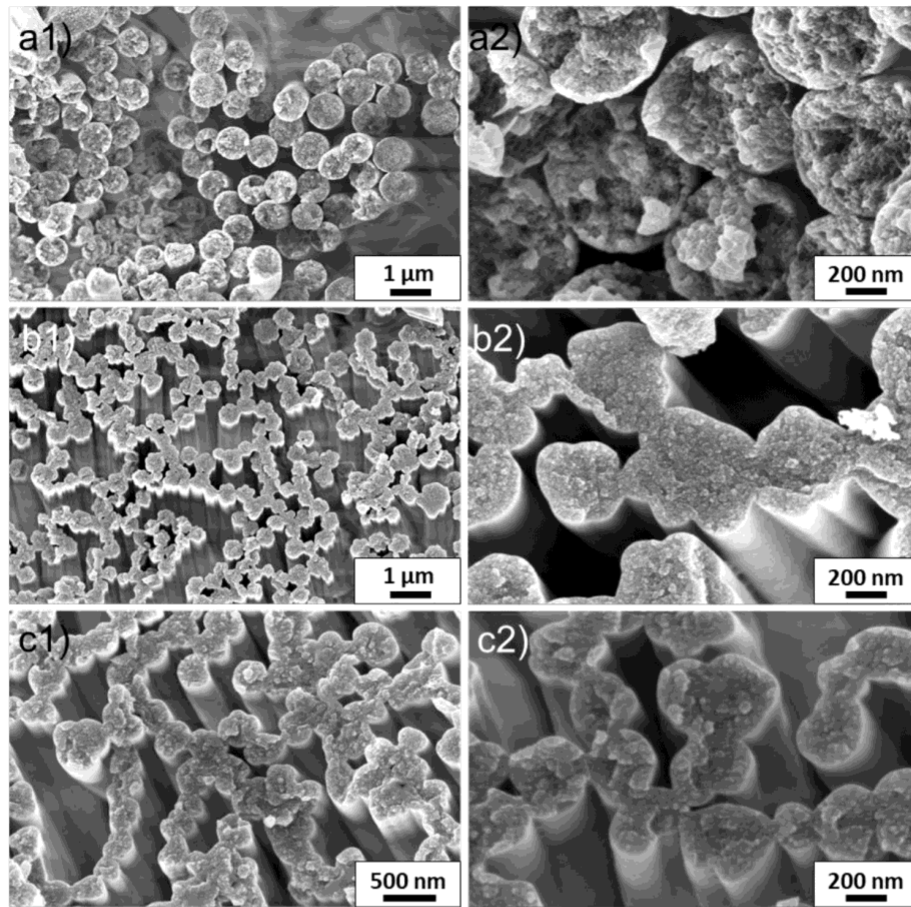


Fig. S2 SEM images of PAN multifibrillar fibers after a) soxhlet extraction in acetone, b) soxhlet extraction and oxidative stabilization at 250 °C and c) immersing in silicon oil and oxidative stabilization at 250 °C

Table S1 Peak location, onset and released energy of the crosslinking reaction of PAN with different catalysts.

Catalyst	Peak [°C]	Energy [J g ⁻¹]	Peak Onset [°C]
-	310	-1390	266
SnCl ₂	285	-635	167
ZnAc ₂	292	-756	205
SnF ₂	312	-720	266
Co(acac) ₃	302	-896	255
CoCl ₂	293	-716	246
CuAc ₂	298	-660	232

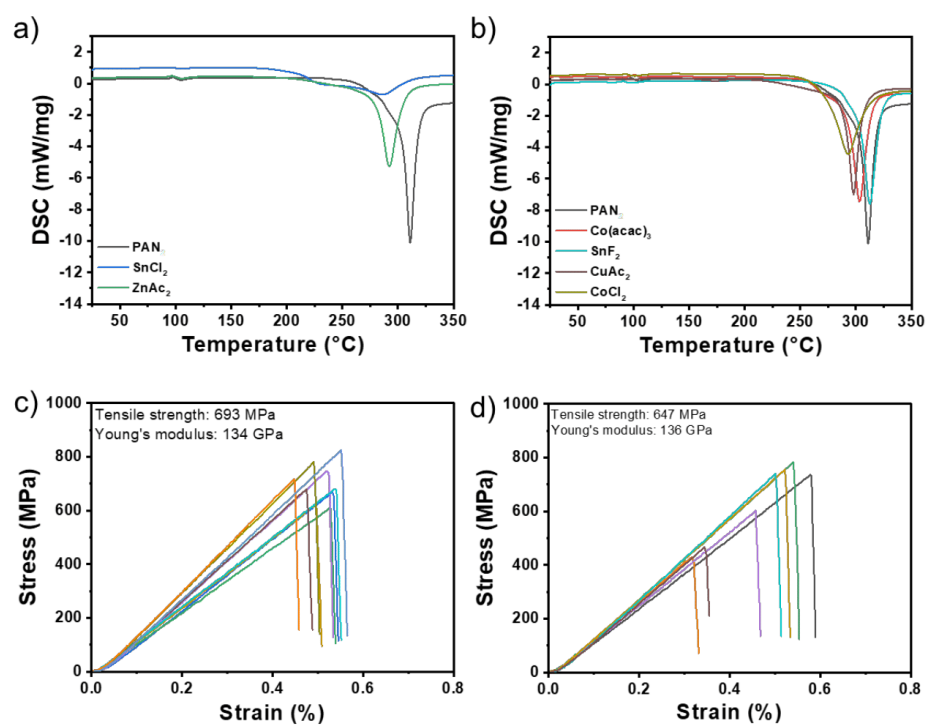


Fig. S3 DSC measurements of the stabilization process of PAN with the catalysts a) SnCl₂, ZnAc₂ and b) Co(acac)₃, SnF₂, CuAc₂ and CoCl₂. Single fiber tensile strength of multifibrillar carbon fibers with catalysts c) SnCl₂ and d) ZnAc₂

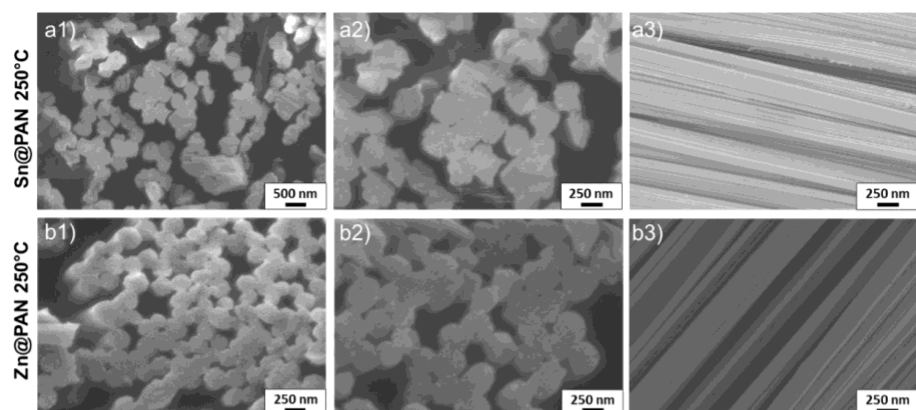


Fig. S4 SEM images of PAN multifibrillar fibers with 3 wt.% of the catalysts a) SnCl_2 and b) ZnAc_2 and oxidative stabilization at 250°C.

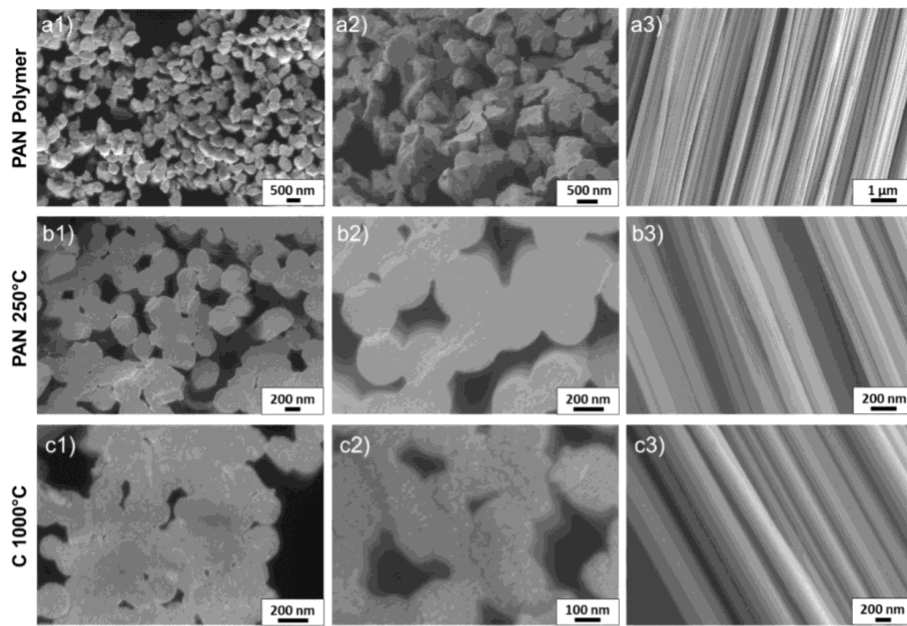


Fig. S5 SEM images of carbon multifibrillar fibers after an electronbeam treatment of 1000 kGy in a) polymer condition, b) after stabilization at 250 °C and c) pyrolysis at 1000°C.

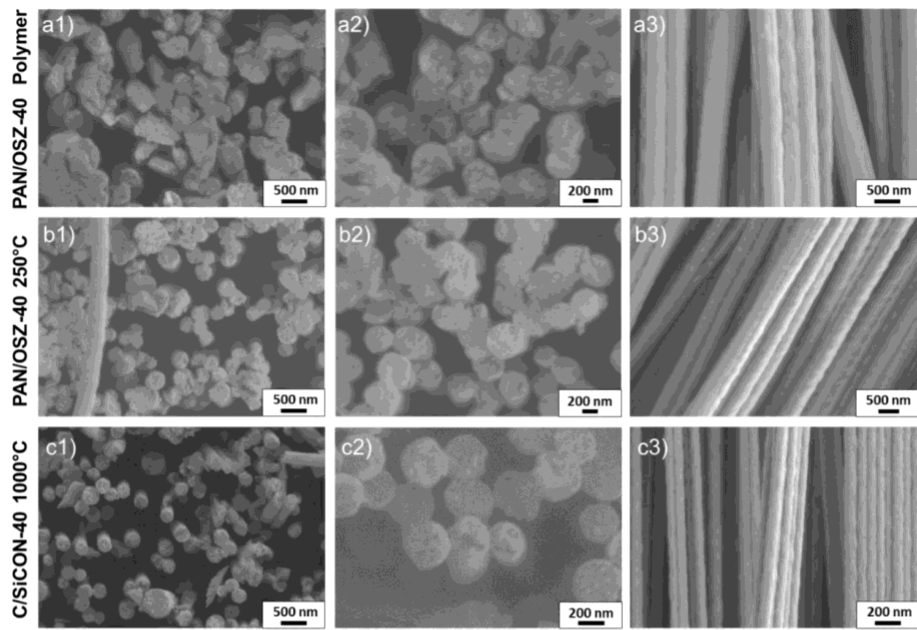


Fig. S6 SEM images of C/SiCON-40 multifibrillar fibers after an electronbeam treatment of 1000 kGy in a) polymer condition, b) after stabilization at 250 °C and c) pyrolysis at 1000°C.

Table S2: Compositions of electrospinning solutions of PAN and PAN/OSZ-40 fibers. 3 wt.% DCP was added with respect to OSZ.

Content [wt.%]	PAN [g]	OSZ [g]	DMF [g]	Acetone [g]	SR
0	1	-	4.70	0.96	9
40	1	0.67	6.03	0.67	6

Table S3: Linear densities of the various electrospun multifibrillar fibers.

sample	Linear density [tex]
carbon fiber SR9	0.33
C/SiCON-40 SR6	1.04

Table S4: Measured densities of the various electrospun fibers.

sample	Density [g cm ⁻³]
carbon fiber	1.80 (± 0.045)
C/SiCON-40	2.00 (± 0.075)

5.3 Synergistic enhancement of thermomechanical properties and oxidation resistance in aligned co-continuous carbon-ceramic hybrid fibers

Materials
Horizons



COMMUNICATION

View Article Online
View Journal



Cite this: DOI: 10.1039/d4mh00956h

Received 23rd July 2024,
Accepted 9th September 2024

DOI: 10.1039/d4mh00956h

rsc.li/materials-horizons

Synergistic enhancement of thermomechanical properties and oxidation resistance in aligned Co-continuous carbon–ceramic hybrid fibers†

Jakob Denk,^a Xiaojian Liao,^b ‡*^{bc} Martin Dulle,^d Stefan Schafföner,^a Stephan Förster,^d Andreas Greiner,^b Günter Motz^{id}*^a and Seema Agarwal^{id}*^b

Carbon fibers are highly valued for their lightweight characteristics, outstanding mechanical properties, and cost-efficiency. However, their limited oxidation resistance and low thermomechanical stability in hot air impose constraints on their utilization. Here, we present an approach to simultaneously achieve high thermomechanical properties and high-temperature oxidation resistance in carbon–ceramic hybrid fibers featuring a highly aligned co-continuous topological structure through a continuous process. These hybrid fibers exhibit superior mechanical properties compared to pure carbon fibers with the same diameter (20 μm), including a tensile strength of 2.0 ± 0.2 GPa, Young's modulus of 175 ± 34 GPa, and elongation at break of $1.3 \pm 0.2\%$. Moreover, when subjected to thermal exposure under stress loading conditions in air, the ceramic constituents form a protective oxidized ceramic layer that effectively mitigates thermal oxidation and mechanical loading effects at elevated temperatures, surpassing the performance of carbon fibers. Our discovery offers a promising avenue for bridging the performance gap between cost-effective high-strength carbon fibers and expensive SiC counterparts with exceptional oxidation resistance, which can be applied in many fields wherever high thermomechanical loading and oxidation-resistant properties are important.

In aerospace and energy industries, there is a critical demand for advanced materials that combine high-temperature thermal stability, high tensile strength, and high Young's modulus.^{1–6}

New concepts

Our work introduces a novel concept for carbon–ceramic hybrid fibers that exhibit exceptional thermomechanical properties and enhanced oxidation resistance. This advancement is achieved through a highly aligned co-continuous structure of carbon and silicon-based ceramic within the continuous fiber, leading to remarkable tensile strength and stability under thermal and oxidative stress. Unlike traditional carbon fibers, which suffer from limited oxidation resistance as well as thermomechanical stability in high-temperature environments, our hybrid material severely increased these resistances. This approach not only surpasses existing materials in performance but also holds significant potential for applications in demanding fields such as aerospace and energy. By expanding the possibilities for hybrid fibers combining carbon and ceramics, our concept provides new insights into the design and fabrication of advanced materials with superior durability and functionality.

Mechanical stability at high temperatures in an oxidizing atmosphere is crucial to ensure materials' reliability in these demanding fields.^{7–10} Carbon fibers have emerged as versatile materials with exceptional properties, including low density ($1.75\text{--}2.00$ g cm⁻³), cost-effectiveness (starting at about 10 € per kg), and impressive mechanical properties such as high tensile strength (up to 7 GPa) and Young's modulus (up to 900 GPa).^{11–14} Carbon fibers have become indispensable in various fields such as automotive, defense technology, wind turbines, medical and sports technology, and aerospace.^{15,16} Despite their high-temperature stability of over one thousand degrees celsius (°C) in the inert atmosphere, carbon fibers face a significant limitation in their operating temperature range in air due to degradation at approximately 400 °C, resulting in a loss of their mechanical function.^{17,18} To overcome this challenge, external oxidation protection strategies have been employed, including the application of ceramic,^{19,20} or metallic²¹ coatings. A typical option to improve the oxidation resistance is to apply SiC coatings with chemical vapor deposition^{22,23} and combine it with mixtures of glass-forming compounds based on Si, B, Al, and/or Zr.^{24–29} Nevertheless, these techniques are characterized by their

^a Chair of Ceramic Materials Engineering, University of Bayreuth, Bayreuth 95440, Germany. E-mail: guenter.motz@uni-bayreuth.de

^b Macromolecular Chemistry 2 and Bavarian Polymer Institute, University of Bayreuth, Bayreuth 95440, Germany. E-mail: agarwal@uni-bayreuth.de

^c School of Materials Science and Engineering, Tianjin University, Tianjin, 300072, People's Republic of China. E-mail: xj_liao24@tju.edu.cn

^d JCNIS-1 Neutron Scattering and Soft Matter, Forschungszentrum Jülich, 52428 Jülich, Germany

† Electronic supplementary information (ESI) available. See DOI: <https://doi.org/10.1039/d4mh00956h>

‡ Present address: School of Materials Science and Engineering, Tianjin University, Tianjin, 300072, People's Republic of China.

complexity and high cost, moreover, the mechanical strength is compromised due to the formation of cracks or pores.²⁹

On the other hand, non-oxide ceramic fibers, such as SiC-based fibers, exhibit exceptional tensile strength (2–4 GPa) at diameters of 7–15 μm and high oxidation resistance.^{26,30–33} However, the high cost of these fibers (starting at about 1200 € per kg) limits their widespread application, primarily confining their use to ceramic matrix composites.^{30,34} For pure SiCN fibers produced from pure polysilazanes *via* melt spinning that are chemically crosslinked and cured under inert gas by electron irradiation, a lower price cannot be expected due to the same manufacturing process.³⁵ However, to increase the thermal stability of carbon fibers in air and to reduce the price of ceramic fibers, highly thermal stable carbon, and ceramic hybrid materials derived from synthesized copolymers of poly(acrylonitrile-oligosilazane) were developed.³⁶ During the pyrolysis of these copolymers, interfaces between the carbon and ceramic occurred, and amorphous and homogeneously distributed Si_3N_4 nanocomposites were formed. These nanocomposites served as oxidation protection for the carbon and significantly increased the oxidation resistance depending on the proportion of oligosilazane (OSZ) in the ceramic phase. Despite achieving exceptional thermal stability in these hybrid materials, only short brittle fiber pieces with a thickness of

approximately 200 μm and poor mechanical properties were obtained, rendering them unsuitable for practical applications. Therefore, the simultaneous achievement of high-temperature oxidation resistance and high strength in carbon-based fibers remains an enduring challenge.

In this study, we propose a strategy to simultaneously achieve high mechanical strength and oxidation resistance in continuous carbon- and silicon-based ceramic hybrid fibers. The key to this discovery lies in the incorporation of carbon with ceramic phases, which exhibit a highly aligned co-continuous topological structure within the continuous fiber (Fig. 1). This distinctive structure is derived from hybrid polymer precursors composed of commercially available polyacrylonitrile (PAN) and oligosilazane, under carefully controlled process conditions. These hybrid fibers offer exceptional tensile strength along with significantly enhanced oxidation resistance and thermo-mechanical stability compared to conventional carbon fibers. Moreover, their production costs are lower than those associated with ceramic SiC fibers. Consequently, these novel hybrid fibers enable components to operate reliably at elevated temperatures while ensuring structural safety, expanding their potential for high-temperature applications.

The high-strength and high oxidation-resistant fibers were fabricated through a three-step process that focused on maintaining an

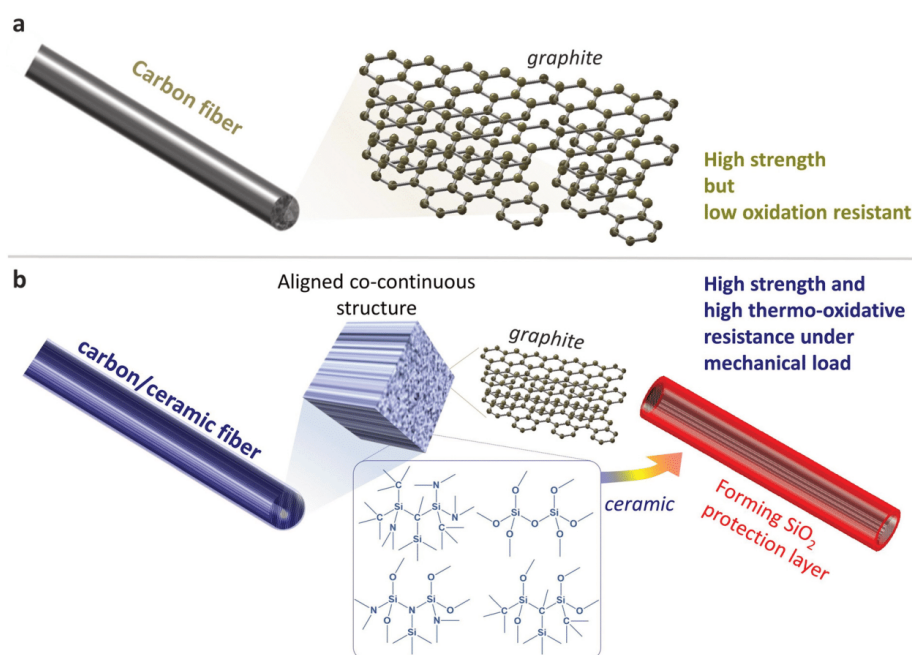


Fig. 1 Graphical illustration of a carbon and carbon–ceramic hybrid fiber and their properties. (a) Carbon fiber has high strength but low oxidation resistance. (b) A schematic of a continuous carbon–ceramic hybrid fiber with an aligned co-continuous structure allowing for high strength and oxidation resistance.

Materials Horizons

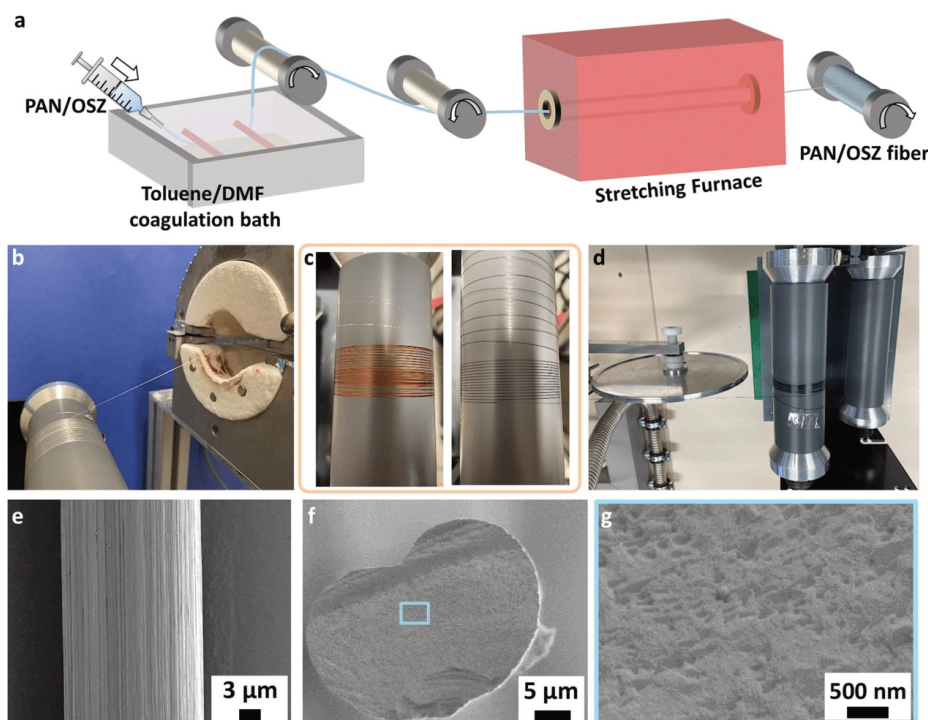


Fig. 2 Preparation and characterization of the fibers. (a) Schematic illustration of wet-spinning a continuous PAN/OSZ hybrid fiber with a continuous stretching process. (b) PAN/OSZ hybrid fiber bundle consisting of 8 filaments during the continuous stabilization process. (c) Oxidized PAN/OSZ hybrid fiber bundle consisting of 8 filaments after being stabilized at 170 °C (right) and 250 °C (left). (d) Collection of the C/SiCON hybrid fiber bundle consisting of 8 filaments on the reel after the continuous pyrolysis process. (e) SEM image of the long axis of the C/SiCON-40 hybrid fiber. (f) and (g) SEM images of the cross-section of C/SiCON-40 hybrid fiber in different magnifications.

aligned co-continuous structure throughout. First, a single continuous fiber was obtained by wet-spinning a PAN solution with different contents of OSZ with an additional stretching process at 150 °C, which aligned the PAN and OSZ along the fiber axis, reduced defects, and densified the fiber with fewer voids (Fig. 2a). Second, bundles of eight PAN/OSZ fibers were joined together and continuously stabilized in a tube furnace at temperatures from 130 °C to 250 °C with a step-wise stabilization program along with a fiber moving rate of 0.1 m h⁻¹ in air (atmospheric pressure, details in the method part) transformed the linear PAN chain into a ladder structure (Fig. 2b, c and Fig. S1, ESI†). Finally, we obtained the carbon ceramic hybrid fibers (C/SiCON) under optimized processing conditions for a definite composition (Fig. 2d). Several experiments were carried out to optimize the best combination for the desired properties by changing the pyrolysis procedure (continuous vs. noncontinuous), pyrolysis temperature (1000 °C, 1200 °C, 1350 °C, and 1500 °C), and the composition of PAN and OSZ in the spinning mixture. A maximum of 40 weight percent (wt%) of OSZ in the spinning mixture was spinnable. Higher than 40 wt% led to phase separation, impeding the stable and continuous spinning of fibers.

Within this context, the polymer fibers are referred to as PAN/OSZ-X, while the pyrolyzed fibers are labeled as C/SiCNO-X, with X denoting the wt% of OSZ in the polymer solution.

The fiber processing was carried out using a solution of PAN and OSZ in different ratios in dimethylformamide (DMF). The fibers were directly wet-spun and passed through a coagulation bath consisting of a mixture of DMF and toluene. Toluene was chosen for the coagulation bath due to its incapability of dissolving PAN and non-reactivity with OSZ. However, the use of pure toluene led to accelerated DMF diffusion from the fiber, resulting in a kidney or sickle-shaped fiber rather than a round or oval one (Fig. S2, ESI†). To resolve this issue, a mixture of toluene and DMF was used in the coagulation bath. The optimal DMF concentration was determined through a series of experiments, revealing that 30 volume percentage (vol%) DMF for PAN/OSZ-40 fibers and 20 vol% DMF for PAN/OSZ-20 fibers produced the most desirable fiber morphology (Table S1, ESI†).

After passing through the coagulation bath, the fibers underwent stretching using a custom-made roll-to-roll heat stretching production line. The stretching was conducted at

150 °C, a temperature above the glass transition temperature (T_g) of PAN (about 103 °C).³⁷ We fabricated the stretched fibers with a stretch ratio (SR) between 5 and 9. The incorporation of OSZ decreased the maximum SR from 9 for pure PAN fiber to 5 for PAN/OSZ-40 fiber (Table S1, ESI†). The ultimate fibers had a diameter of $\sim 37 \mu\text{m}$ (Fig. S3, ESI†). The orientation of the PAN and OSZ structure was determined by the 2D-WAXS (Fig. S4, ESI†). The sharp (200) reflections in the 2D-WAXS images suggest an aligned molecular structure in the stretched PAN/OSZ fibers (SR 5). The response calculated orientation order parameter value was about 0.75. The current fiber's production rate was about 0.3 m min^{-1} . Reduction of the diameter of the fiber and speeding up the production rate can be achieved simultaneously by simply using professional wet-spinning setups and lengthening the production line, which is similar to the industrial fabrication of carbon fibers.

Subsequently, the fibers were oxidized by heating them slowly from 130 °C to 250 °C, with a slow velocity rate of 0.1 m h^{-1} through the tube furnace in air (Fig. S1, ESI†). During this stabilization, the linear PAN chain reacts to a ladder structure by dehydrogenation and cyclization reactions,^{11,38} as indicated by the fiber's color change to brown and black (Fig. 2b and c) as well. This reaction is highly exothermic and shows a strong signal in the DSC curves for the different PAN/OSZ fibers (Fig. S5, ESI†). The previously established slow and stepwise heating program, utilized for the electrospun nanofiber nonwovens in our prior study,³⁹ was also applicable for the wet-spun PAN/OSZ fibers. To achieve complete carbonization and ceramization reactions of oxidized PAN and OSZ, the fibers were continuously pyrolyzed at temperatures exceeding 1000 °C under atmospheric pressure and a nitrogen atmosphere.

The pyrolysis behaviors of hybrid fibers with different amounts of OSZ were first investigated by TGA measurements up to 1550 °C under a nitrogen atmosphere (Fig. S6, ESI†). The ladder-structured PAN transformed into an sp^2 hybridized carbon structure, and HCN and N_2 were released at 250 °C to 1000 °C.¹¹ For OSZ, dehydrocoupling and transamination reactions continued to occur above 250 °C.⁴⁰ These reactions led to cross-linking of the oligomer, and the release of H_2 and NH_3 . In the range of 400–800 °C, the precursor transformed into an amorphous SiCNO ceramic, and the release of H_2 and CH_4 .⁴⁰ Once the temperature reached 1000 °C, a platonic state was achieved. Thus, the transformation into a C/SiCON ceramic was completed. Scanning electron microscopy (SEM) images show that the carbon fibers and the C/SiCON fibers have a uniform diameter for each fiber ($20 \pm 1.0 \mu\text{m}$), highly aligned traceable appearance, and dense cross-section (Fig. 2e–g and Fig. S7–S9, ESI†). However, above 1500 °C, decomposition of the ceramic occurs probably with the release of N_2 or CO as can be seen by the TGA analysis (Fig. S6, ESI†), and the material transforms from Si_3N_4 to SiC.⁴⁰ Fibers pyrolyzed at 1500 °C had a distinct porous structure in cross-section and in longitudinal direction, which are absent in fibers pyrolyzed at lower temperatures (Fig. S9, ESI†).

To determine the optimal parameters for creating remarkably strong fibers, the tensile strength, Young's modulus, and

elongation at break were analyzed for the fibers with varying compositions (0, 20, and 40 wt%) of OSZ to PAN (Fig. 3a–d). These fibers were pyrolyzed at varying temperatures for 1 hour in a batch-like non-continuous process, which allowed for completing the carbonization and ceramization reactions in the fiber. Our approach involved aligning bundles of approximately 25 fibers, each around 15 cm in length, and securing them onto movable carbon pieces within a quartz glass crucible, as shown in Fig. S10, ESI†. This technique ensured that the fibers remained under tension during the heat treatment while still being able to contract and move without fracturing. Increasing the pyrolysis temperature resulted in an arching trend in average tensile strength and Young's modulus (Fig. S11 and S12, ESI†). The maximum tensile strength of $1.60 \pm 0.15 \text{ GPa}$ was achieved at 1200 °C, whereas the maximum Young's modulus was achieved at 1350 °C. However, higher temperatures lead to decreased elongation at break. OSZ decomposed at 1500 °C, which resulted in many porous defects in the fiber, ultimately reducing its overall mechanical properties. Optimum values under a non-continuous pyrolysis process for different weight percents of OSZ to PAN system, concerning tensile strength, were obtained with 40 wt% and a pyrolysis temperature of 1200 °C (Fig. 3a–d and Fig. S13, ESI†). Interestingly, the subsequent continuous pyrolysis process with optimized conditions enhanced the mechanical properties of fibers. The continuous process ensured that every fiber was subjected to a consistent and uniform force, while also automating the process to minimize external factors. This continuous process did not result in any further changes in the diameters of the fibers (about $20 \mu\text{m}$, Fig. S7–S9, ESI†). Due to the continuous oxidation and pyrolysis processes, the influences of sample preparation are eliminated and the process is much more stable once running continuously. As a result, fewer defects are likely to occur in the continuous fibers. The average tensile strength was therefore higher at $2.0 \pm 0.2 \text{ GPa}$, while Young's modulus was $175 \pm 34 \text{ GPa}$, and the elongation at break was $(1.3 \pm 0.2) \%$ in continuous C/SiCON-40 fibers pyrolyzed at 1200 °C. The maximum tensile strength can be up to 2.5 GPa, and the maximum Young's modulus is up to 270 GPa (Fig. S13d, ESI†). For comparison, the strength of pure carbon fiber with the same diameter is about $1.1 \pm 0.14 \text{ GPa}$ and its Young's modulus is $140 \pm 30 \text{ GPa}$. It is noteworthy that this demonstrates the high potential of these fibers spun with simple laboratory equipment. With a professional fiber spinning device, it should be possible to produce fibers with smaller diameters and thus fewer defects per fiber length, which should again significantly improve the mechanical properties.

The TGA conducted in air with a heating rate of 5 K min^{-1} was used to investigate the oxidation resistance of the fibers with different amounts of OSZ to PAN (Fig. 3e). Pure carbon fibers are not very stable to oxidation and usually start to degrade at 400 °C in air.^{17,18} However, the oxidation stability was greatly increased with increasing contents of SiCON. For example, a mass loss of 20% occurred in pure carbon fibers already at 573 °C; by adding 20 and 40 wt% OSZ, this temperature increased to 721 °C and 833 °C, respectively (Fig. 3e). We further tested the response of

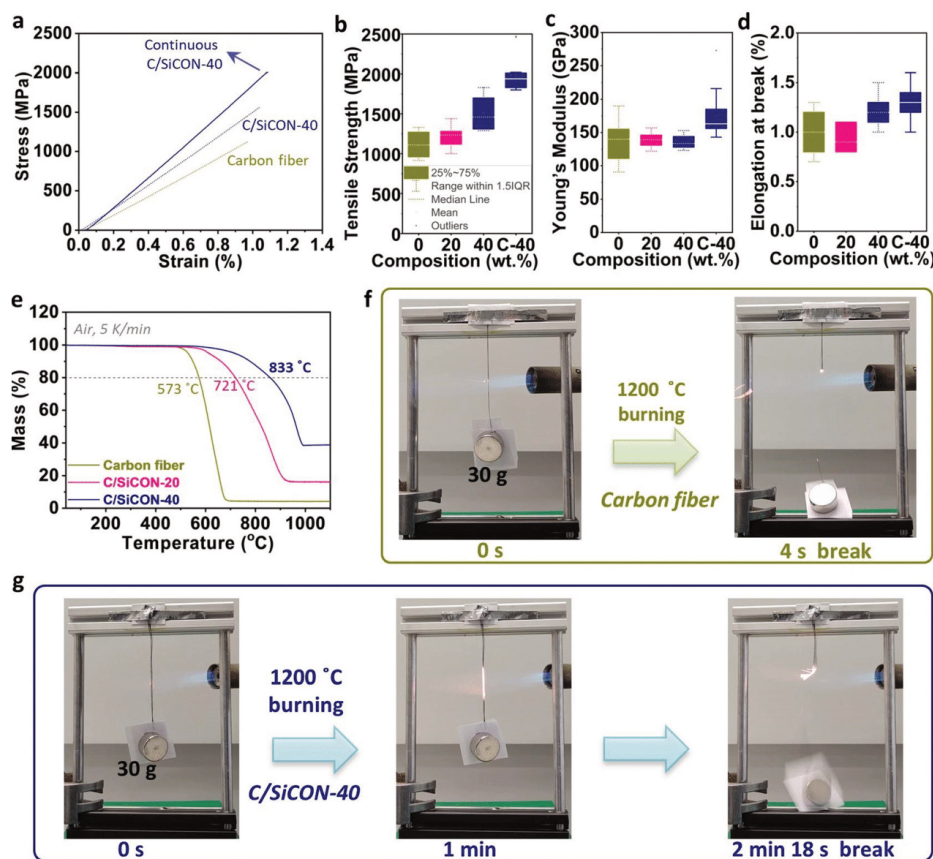


Fig. 3 Mechanical and thermal properties of the fibers. (a) Stress-versus-strain curves of noncontinuous carbon fibers (dark yellow, dot line), noncontinuous C/SiCON-40 fibers (blue, dot line), and continuous C/SiCON-40 fibers (blue, solid line). (b)–(d) Comparison of tensile strength, Young's modulus, and elongation at break of noncontinuous carbon fibers (yellow), noncontinuous C/SiCON-20 (pink), noncontinuous C/SiCON-40 fibers, and continuous C/SiCON-40 fibers (blue). The C-40 represents the continuous C/SiCON-40 fiber. The different colors follow the composition depicted in Fig. 3a. (e) Thermogravimetric analysis of carbon fiber and C/SiCON fibers with different content of OSZ in the polymer solution. (f)–(g) A set of real-time images showing carbon fiber bundle consisting of 40 filaments (f) and a continuous C/SiCON-40 hybrid fiber bundle consisting of 40 filaments (g) exposed to a 1200 °C gas flame under tension with 30 g weight in air, respectively.

fibers under mechanical stress at 1200 °C in air to test the mechanical stability of fibers under high temperature. For this purpose, two sets of fiber bundles, consisting of continuous C/SiCON-40 hybrid fibers and pure carbon fibers, each comprising 40 filaments, were exposed to a flame at about 1200 °C while suspended with weights of 30 g (Movie S1, ESI†). A set of real-time digital photos reveals an impressive outcome (Fig. 3f and g): the carbon fibers broke after 4 seconds, while the C/SiCON fiber could withstand mechanical stress at 1200 °C for 2 min 18 seconds. It suggests that our C/SiCON fibers surpass pure carbon fibers with the same diameter in high strength, oxidation resistance, and high-temperature degradation resistance even under mechanical stress, making them an exceptional choice for demanding applications.

ATR-FTIR (attenuated total reflectance-Fourier transform infrared spectroscopy) was used to study the sequence of reactions taking place during heat treatment (Fig. S14, ESI†). After the stabilization process, typically the –CH and –CN bands of the PAN strongly decreased, whereas the C=N band strongly increased. Meanwhile, the Si–CH₃ deformation (1250 cm⁻¹) and Si–O–Si stretching (1033 cm⁻¹) had their origin in the OSZ structure. After the process of pyrolysis, there were no remaining organic groups and only a few remnants of the OSZ's functional groups were present. Solid ¹³C- and ²⁹Si-NMR (nuclear magnetic resonance) provided additional information about the carbon and ceramic present in the C/SiCON-40 fiber. The ¹³C-NMR revealed a broad peak centered at 120–125 ppm, indicating the

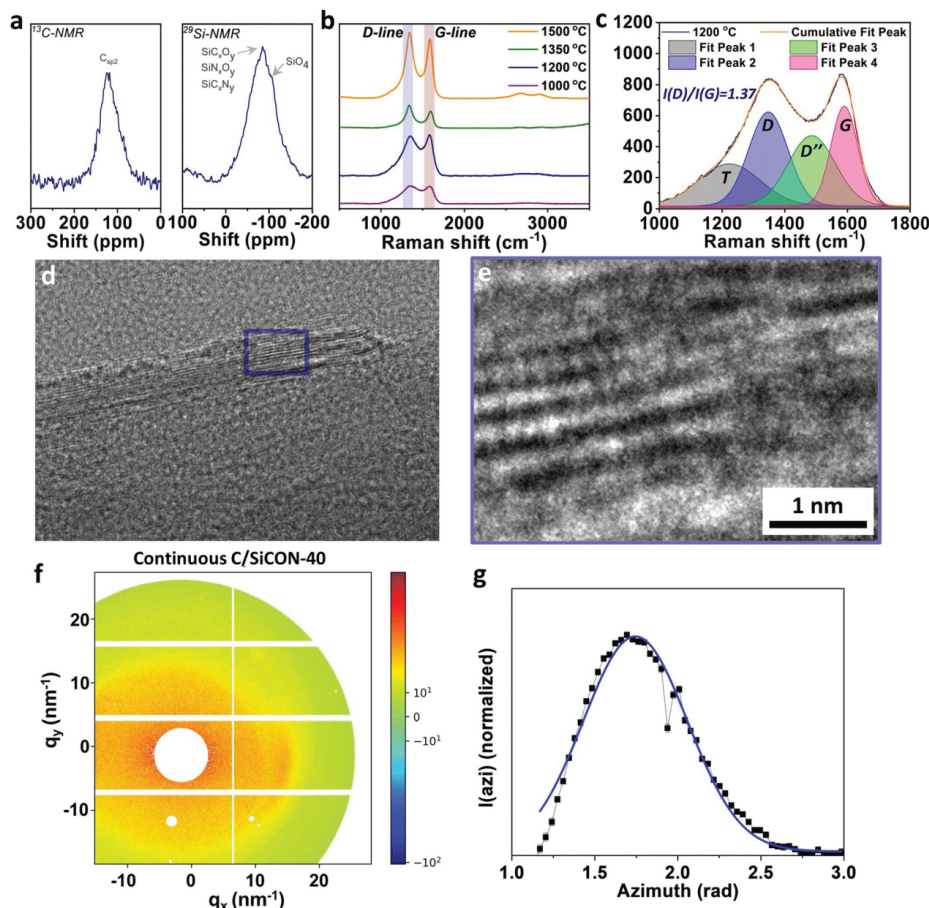


Fig. 4 Morphology and properties of C/SiCON hybrid fibers. (a) Solid ^{13}C - and ^{29}Si -NMR spectra of C/SiCON-40 hybrid fibers pyrolyzed at 1200 °C. (b) Raman spectra of the C/SiCON-40 hybrid fibers pyrolysis at different temperatures. (c) Curves fitted in Raman spectra of C/SiCON-40 hybrid fibers pyrolysis at 1200 °C with a Gaussian function. The area values of (D) and (G) peaks were used to calculate the ratio of $I_{\text{D}}/I_{\text{G}}$. The fitting curves also include the minor bands T and D', which are centered at approximately 1200 cm^{-1} and 1500 cm^{-1} , respectively. The T band is attributed to sp^2 - sp^3 bonds, or C=C and C-C stretching vibrations of polyene-like structures, while the D' band is associated with the fraction of amorphous carbon present in the samples. a.u., arbitrary units. (d) and (e) TEM images of C/SiCON-40 hybrid fibers in different magnifications showing the graphite nanocrystallites in the free carbon nanodomains. (f) 2D WAXS patterns of C/SiCON-40 hybrid fibers. (g) The azimuthal scan profiles of 2D WAXS patterns of (f), showing the alignment of graphite nanocrystals along the fiber axis individual order parameters are given in Table S2 (ESI †). The plots were normalized with respect to their base for visibility.

presence of sp^2 carbon in a graphitic-like form (Fig. 4a). Furthermore, the ^{29}Si -NMR detected a broad signal ranging from -25 to -140 ppm, suggesting the existence of complex SiO_4 , SiC_xO_y , SiN_xO_y , and SiC_xN_y environments. 39 To further evaluate the composition, elemental analysis of the stabilized, and pyrolyzed material was carried out (Table S3, ESI †). The contents of C, O, and Si increased, while the H and N decreased after the stabilization and pyrolysis. The composition of pyrolyzed C/SiCON-40 fiber was C/H/O/N/Si of about 62.9/2.4/16.9/7.6/10.2 (atomic ratio).

Clearly, these analyses strongly indicate that carbon and SiCON were incorporated into the C/SiCON hybrid fibers *via* wet-spinning, stretching, and additional oxidation and pyrolysis processes. Furthermore, the Raman spectra, 2D-WAXS/SAXS patterns (wide-angle X-ray scattering and small-angle X-ray scattering), and TEM (transmission electron microscope) were used for the characterization of the C/SiCON-40 fibers at various pyrolysis temperatures to study the structural interaction of graphite and ceramic units on an atomic level (Fig. 4b-g). Raman spectra showed that all fibers

exhibited D- and G-bands of graphite-like carbon at 1280 and 1600 cm^{-1} , respectively (Fig. 4b). The I_D/I_G ratio decreased as the pyrolysis temperature increased, from 1.65 at 1000 °C to 1.13 at 1500 °C (Fig. 4c and Fig. S15, ESI†). This indicates that higher temperatures resulted in fewer defects in graphene layers, which is consistent with previous findings on pure carbon-based materials.^{39,41} The C/SiCON-40 fibers exhibited a moderate I_D/I_G value of about 1.37 and a low crystalline degree, resembling sp^2 -rich amorphous carbon.

Upon closer inspection through TEM investigations, it was observed that the C/SiCON-40 fiber that was pyrolyzed at 1200 °C formed small nanocrystallites (Fig. 4d and e). These nanocrystallites mainly consist of graphitic structures with lattice fringes measuring 0.34 nm. Furthermore, the 2D-WAXS and SAXS patterns indicated that higher temperatures improved the alignment

of the graphene sheets (Fig. 4f and g and Fig. S16, ESI†). The crystal size changed from 0.97 nm to 2.46 nm with the increase in pyrolysis temperature, whereas for the continuous fiber the value was slightly higher at 2.51 nm (Table S2, ESI†). Meanwhile, for pyrolysis temperatures from 1000 °C to 1350 °C, a slight increase in the calculated orientation order parameter value was found (Table S2, ESI†). Additionally, the mechanical properties of the fiber followed the same trend as the order parameter increased from 1000 °C to 1350 °C and slightly decreased at 1500 °C. This suggests that the orientation of the nanostructure governs the mechanical properties. Upon thorough data analysis, we develop a compelling hypothesis that strongly suggests the aligned co-continuous structures caused by efficient heat-stretching and optimized pyrolysis process in the presence of PAN and OSZ as the precursors of carbon and ceramic, yield the combination of

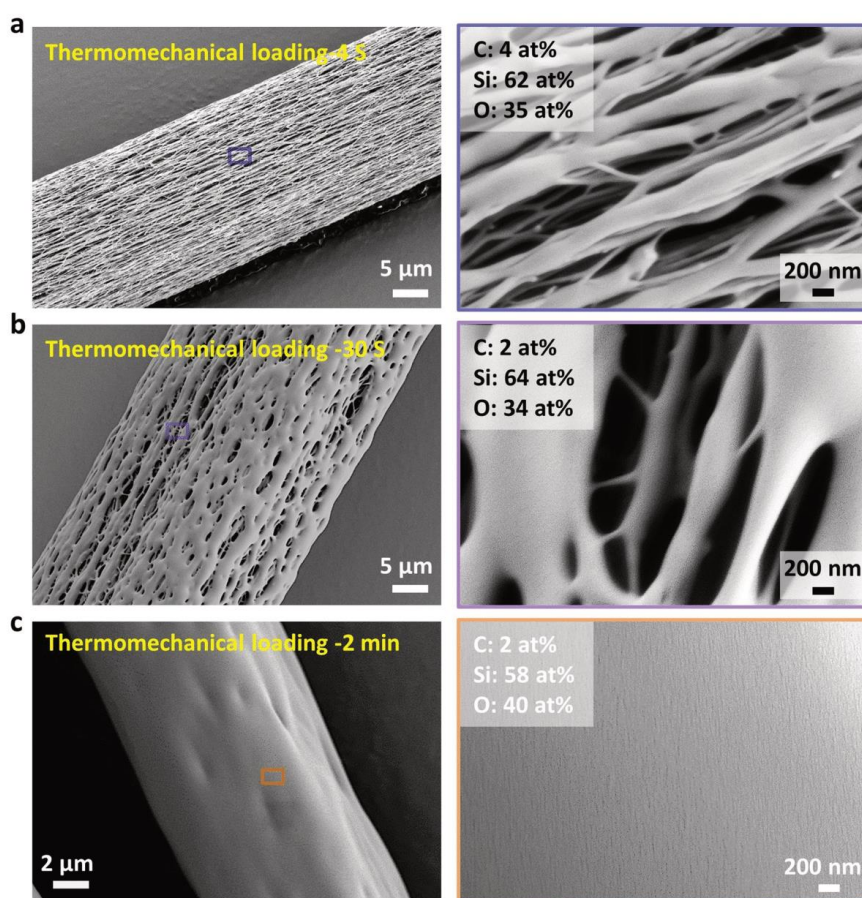


Fig. 5 Changes in the morphology of C/SiCON-40 hybrid fibers under thermomechanical loading at 1200 °C in air. (a) For 4 seconds. (b) For 30 seconds. (c) For 2 minutes. The insert numbers are the surface elemental composition of the fibers measured by SEM-EDS.

high strength and excellent oxidation resistance and mechanical degradation resistance in C/SiCON fibers.

The stretching of the PAN/OSZ fiber plays a crucial role in our wet-spinning process, as we observed significantly aligned co-continuous carbon and ceramic phases in the C/SiCON hybrid fibers. This, in turn, has led to the refinement of fiber dimensions. The control of the C/SiCON-40 samples without stretching or with a less stretched ratio (SR4) during the wet-spinning had a large diameter of about 46 μm and a rough surface. At the same time, their tensile strength was only 713 ± 149 MPa, while Young's modulus was 56 ± 15 GPa (Fig. S17, ESI[†]). This is due to the Griffith principle, as the tensile strength increases exponentially with decreasing diameter for brittle fibers. This is because the probability of a defect per unit length decreases with fiber diameter.⁴² Our method is, therefore, an effective way to fine-tune fiber dimensions and produce well-aligned co-continuous nanostructures for improving mechanical properties. Meanwhile, to discover the mechanism of the improved oxidation resistance and thermomechanical properties, we also investigated the morphology and surface elemental composition of the C/SiCON-40 fibers after being exposed to air at a 1200 °C flame while being weighted down (Movie S1, ESI[†]), by SEM and SEM-EDS (energy-dispersive x-ray spectroscopy), respectively (Fig. 5 and Fig. S18, ESI[†]). While the carbon was burned off, the ceramic material emerged as the sole survivor after a mere 4 seconds of being burned at 1200 °C, leaving behind an aligned porous structure on the fiber surface. This aligned porous structure also supported the aligned co-continuous structure of carbon and ceramic in the C/SiCON hybrid fibers (Fig. 5a). Along with the burning time at about 30 seconds (Fig. 5b), the aligned porous ceramics with a melted statue were formed (Fig. 5c and Fig. S18, ESI[†]). The SEM-EDS analysis showed that the carbon content has decreased to 2 at%. Meanwhile, the contents of silicon and oxygen have increased to 34 at% and 64 at% (the molar ratio between Si and O is about 2), respectively. These investigations suggest that the fiber transformed to oxidized ceramic SiO₂ on its surface to protect the whole fiber against oxidation and thermomechanical loading. However, prolonged exposure for approximately 2 minutes leads to complete oxidation and fusion of the material, resulting in a cohesive solid fiber. Subsequent high-temperature exposure at 2 minutes and 18 seconds causes the ceramic matrix to melt, leading to a loss of mechanical stability within the fibers as observed in Movie S1, ESI[†]. Following complete oxidation and carbon depletion, these fibers no longer possess inherent mechanical stability. Based on our investigation, the study highlights the novelty of C/SiCON fibers due to their highly aligned co-continuous topological structure. These fibers exhibit enhanced mechanical properties and improved oxidation resistance under thermomechanical loading compared to pure carbon fibers with similar diameters. This innovation effectively reduces the disparity between cost-effective high-strength carbon fibers and expensive SiC fibers with exceptional oxidation resistance.

Conclusions

In summary, this work demonstrated the concept of simultaneously achieving high strength, oxidation resistance, and

mechanical degradation resistance under thermomechanical loading in carbon and ceramic hybrid fibers with aligned co-continuous structures by the synergetic engineering method including wet-spinning, stretching, and continuous stabilization and pyrolysis processing. The fabrication, like the commercial carbon fiber line process, is continuous and adjustable, making it cost-effective and industrially scalable. This work also provides guidance to narrow the gap between pure carbon fibers with high strength and SiC fibers with high oxidation resistance and mechanical degradation resistance under thermomechanical loading. The fibers will enable numerous applications wherever high-stress loading at high temperatures is important, such as aerospace and construction applications. Importantly, this concept can be expanded to other systems with an aligned co-continuous structure to achieve a combination of beneficial properties.

Author contributions

X. L., A. G., G. M., and S. A. proposed the idea and designed the experiments. J. D., and X. L. conducted preparation of fibers and characterization. M. D. and S. F. helped with the XRD experiments and results analysis. All authors contributed to the discussion of the data. S. S. helped in discussions. The manuscript is written by J. D. and X. L. with input from all authors under the lead of X. L., G. M., and S. A.

Data availability

The data supporting this article have been included as part of the ESI[†].

Conflicts of interest

There are no conflicts to declare.

Acknowledgements

We thank R. Siegel, B. Bojer, and J. Senker for the solid-state NMR measurement; L. Benker for the Raman measurements. We would like to thank R. Giesa for providing the middle-pressure syringe pump and associated equipment. The work was supported by the University of Bayreuth and the Deutsche Forschungsgemeinschaft (DFG). A. G. and G. M. would like to thank DFG (Deutsche Forschungsgemeinschaft; 455984818; GR 972/61-1 and MO 851/21-1) for the financial support.

Notes and references

- 1 N. P. Padture, *Nat. Mater.*, 2016, **15**, 804–809.
- 2 C. Liu, Y. Liao, W. Jiao, X. Zhang, N. Wang, J. Yu, Y. T. Liu and B. Ding, *Adv. Mater.*, 2023, **35**, e2304401.
- 3 J. H. Perepezko, *Science*, 2009, **326**, 1068–1069.
- 4 P. Wang, X. Dai, P. Xu, S. Hu, X. Xiong, K. Zou, S. Guo, J. Sun, C. Zhang, Y. Liu and T. Zho*, *eScience*, 2023, **1**, 100088.

- 5 N. P. Padture, M. Gell and E. H. Jordan, *Science*, 2002, **296**, 280–284.
- 6 X. Zhang, Y. Chen and J. Hu, *Prog. Aerosp. Sci.*, 2018, **97**, 22–34.
- 7 X. Xu, Q. Zhang, M. Hao, Y. Hu, Z. Lin, L. Peng, T. Wang, X. Ren, C. Wang and Z. Zhao, *Science*, 2019, **363**, 723–727.
- 8 S. Wu, H. Li, D. N. Futaba, G. Chen, C. Chen, K. Zhou, Q. Zhang, M. Li, Z. Ye and M. Xu, *Adv. Mater.*, 2022, **34**, e2201046.
- 9 M. Belmonte, *Adv. Eng. Mater.*, 2006, **8**, 693–703.
- 10 S. Zhao, G. Siqueira, S. Drdova, D. Norris, C. Ubert, A. Bonnin, S. Galmarini, M. Ganobjak, Z. Pan, S. Brunner, G. Nystrom, J. Wang, M. M. Koebel and W. J. Malfait, *Nature*, 2020, **584**, 387–392.
- 11 R. N. J. H. Khayyam, S. Nunna, G. Golkarnarenji, K. Badii, S. M. Fakhrhoseini, S. Kumar and M. Naebe, *Prog. Mater. Sci.*, 2020, **107**, 100575.
- 12 TORAYCA™ Technical Manual, Toray Composite Materials America, Inc., (<https://www.torayca.com/products/carbon-fiber/>).
- 13 J. Zhang, G. Lin, U. Vaidya and H. Wang, *Composites, Part B*, 2023, **250**, 110463.
- 14 D. Church, *Reinf. Plast.*, 2018, **62**, 35–37.
- 15 N. Gupta, V. I. Artyukhov, E. S. Penev and B. I. Yakobson, *Adv. Mater.*, 2016, **28**, 10317–10322.
- 16 M. M. Harussani, S. M. Sapuan, G. Nadeem, T. Rafin and W. Kirubaanand, *Def. Technol.*, 2022, **18**, 1281–1300.
- 17 L. A. Tkachenko, A. Y. Shaulov and A. A. Berlin, *Inorg. Mater.*, 2012, **48**, 213–221.
- 18 M. Minus and S. Kumar, *JOM*, 2005, **57**, 52–58.
- 19 Y. P. Zhang, Y. H. Shen, W. W. Chen, H. W. Cheng and L. Wang, *Mater. Sci. Forum*, 2017, **898**, 1575–1582.
- 20 T. Xiao, J. Kuang, P. Sun, X. Hou, Q. Wang, P. Jiang and W. Cao, *Ceram. Int.*, 2019, **45**, 2432–2438.
- 21 Z. Hua, Y. Liu, G. Yao, L. Wang, J. Ma and L. Liang, *J. Mater. Eng. Perform.*, 2011, **21**, 324–330.
- 22 K. L. Choy, *Prog. Mater. Sci.*, 2003, **2**, 57–170.
- 23 R. Naslain, *Compos. Sci. Technol.*, 2004, **64**, 155–170.
- 24 S. P. C. Hu, S. Tang, Z. Yang, S. Wang and H.-M. Cheng, *Corros. Sci.*, 2015, **94**, 452–458.
- 25 S. B. F. Lamouroux, R. Pailler, R. Naslain and M. Cataldi, *Compos. Sci. Technol.*, 1999, **59**, 1073–1085.
- 26 L. A. Tkachenko, A. Y. Shaulov and A. A. Berlin, *Inorg. Mater.*, 2012, **48**, 213–221.
- 27 J. E. Sheehan, *Carbon*, 1989, **27**, 709–715.
- 28 R. Weiss, Carbon Fibre Reinforced CMCs: Manufacture, Properties, Oxidation Protection, *High Temperature Ceramic Matrix Composites*, Wiley-VCH Verlag GmbH & Co. KGaA, Weinheim, 2006, DOI: [10.1002/3527605622.ch69](https://doi.org/10.1002/3527605622.ch69).
- 29 K. Xia, C. Lu and Y. Yang, *New Carbon Mater.*, 2015, **3**, 236–243.
- 30 A. R. Bunsell and A. Piant, *J. Mater. Sci.*, 2006, **41**, 823–839.
- 31 H. Ichikawa, *J. Ceram. Soc. Jpn.*, 2006, **114**, 455–460.
- 32 T. Ishikawa, *Adv. Polym. Sci.*, 2005, **178**, 109–144.
- 33 V. Murthy, *Bull. Mater. Sci.*, 1993, 87.
- 34 O. Flores, R. K. Bordia, D. Nestler, W. Krenkel and G. Motz, *Adv. Eng. Mater.*, 2014, **16**, 621–636.
- 35 O. Flores, T. Schmalz, W. Krenkel, L. Heymann and G. Motz, *J. Mater. Chem. A*, 2013, **1**, 15406–15415.
- 36 L. F. B. Ribeiro, O. Flores, P. Furtat, C. Gervais, R. Kempe, R. A. F. Machado and G. Motz, *J. Mater. Chem. A*, 2017, **5**, 720–729.
- 37 X. Liao, V. Jerome, S. Agarwal, R. Freitag and A. Greiner, *Macromol. Biosci.*, 2022, **22**, e2200291.
- 38 X. Liao, Y. Ding, L. Chen, W. Ye, J. Zhu, H. Fang and H. Hou, *Chem. Commun.*, 2015, **51**, 10127–10130.
- 39 X. Liao, J. Denk, T. Tran, N. Miyajima, L. Benker, S. Rosenfeldt, S. Schafföner, M. Retsch, A. Greiner and G. Motz, *Sci. Adv.*, 2023, **9**, eade6066.
- 40 D. S. S. Traßl, G. Motz, E. Rössler and G. Ziegler, *J. Eur. Ceram. Soc.*, 2000, **20**, 215–225.
- 41 Z. Xu, Y. Liu, X. Zhao, L. Peng, H. Sun, Y. Xu, X. Ren, C. Jin, P. Xu, M. Wang and C. Gao, *Adv. Mater.*, 2016, **28**, 6449–6456.
- 42 A. A. Griffith, VI. The phenomena of rupture and flow in solids, *Philos. Trans. R. Soc., A*, 1921, **221**, 163–198, DOI: [10.1098/rsta.1921.0006](https://doi.org/10.1098/rsta.1921.0006).

Supplementary Information (SI) for Materials Horizons.
This journal is © The Royal Society of Chemistry 2024

Supporting Information

Synergistic Enhancement of Thermomechanical Properties and Oxidation Resistance in Aligned Co-Continuous Carbon-Ceramic Hybrid Fibers

Jakob Denk,^a Xiaojian Liao,^{†bc} Martin Dulle,^d Stefan Schafföner,^a Stephan Förster,^d Andreas Greiner,^b Günter Motz,^{*a} Seema Agarwal,^{*b}*

E-mail: agarwal@uni-bayreuth.de (S. Agarwal); guenter.motz@uni-bayreuth.de (G. Motz); xj_liao24@tju.edu.cn (X. Liao)

EXPERIMENTAL SECTION

Materials: Polyacrylonitrile copolymer (PAN, copolymer with max. 8 % methyl acrylate and methallylsulfonate according to the datasheet from Dolan GmbH; number average molar mass (M_n) = 95,000; registration No. 26658-88-8) was obtained from Dolan GmbH (Germany). Oligosilazane Durazane 1800 (OSZ) was obtained from Merck (Germany). Dicumylperoxide (DCP) was obtained from Sigma-Aldrich (Germany). N, N'-dimethylformamide 99.99 % (DMF) from Fisher Scientific GmbH (Germany) and anhydrous toluene from Carl Roth (Germany), were obtained. All chemicals were used as received.

Wet-spinning of Polymer fibers: The spinning solution was prepared by dissolving PAN powder and Durazane1800 with 3 wt.% DCP in DMF overnight at room temperature (**Table S1**). Afterwards, the viscous solution was filled into a 10 mL metal syringe and stored for 8 h until all air bubbles had risen to the top of the syringe resulting in a bubble-free solution. A custom-made wet-spin setup, including a syringe pump, precipitation bath, and tube furnace, was assembled to spin continuous polymer fibers from the PAN/OSZ hybrid precursors solution. The syringe pump was used to control the flow rate of the spinning solution, while the precipitation bath facilitated the formation of gel fibers, and the furnace oven allowed for controlled heating for stretching and consolidating the fibers. For the spinning process, 30 G needles with a flat tip (inner diameter: 190 μm) and a middle-pressure syringe pump (NEMESYS cetoni, Germany) were used. The pump was programmed to the required flow rate (0.0006-0.001 ml s^{-1}) in the associated software and the polymer solutions were spun into the precipitation bath at room temperature. For the PAN/OSZ-40 fibers, 30 vol% DMF, for PAN/OSZ-20 fiber, 20 vol% DMF and for pure PAN fibers, dist. water with 20 vol% DMF was used as the precipitation bath (**Table S1**).

The single continuous polymer fiber obtained was collected and stretched by a custom-made stretching instrument consisting of three parts: a tubular furnace with one heat zone (Heraeus, D6450 Hanau, Typ: RE 1.1, 400 mm length, Germany), two rollers controlled by electronic motors and a laptop with "LV2016" software, which was used to precisely control the velocities of the motors. The fibers could be stretched continuously by adjusting the velocities of the two rollers in the LV2016 software. The SR was calculated by the equation: $SR = V_f / V_s$, where V_f and V_s represent the velocities of the fast roller and slow roller, respectively, similar to previously published literature from our group.¹ To obtain a high SR (5-

9), the fibers were repeatedly stretched while heated to 130 °C and dried for four days in a vacuum drying furnace (Heraeus, VT 6060 M) at 70 °C.

Stabilization and pyrolysis to non-continuous C/SiCNO fibers: For non-continuous stabilization and pyrolysis of the fibers, the fibers were bundled in rovings of 25 fibers and attached to graphite pieces using a high-temperature mullite adhesive (Porrathin 30, Rath, Austria). This method of attachment allowed the fibers to shrink and contract without tearing apart. Stabilization was performed using a stepwise temperature program from RT to 250 °C (Figure S1) in an oxide-lined furnace under atmospheric pressure (Nabertherm N41/H, Germany). Pyrolysis proceeded in a tube furnace (Thermal Technology, High-Temperature TA 106320, USA) at 1000, 1200, 1350, 1500 °C (heating rate 3 K min⁻¹, 1 h hold time at maximum) under atmospheric pressure and N₂ atmosphere (flow rate 15 L/h).

Stabilization and pyrolysis to continuous C/SiCNO fibers: For continuous production, eight fibers were combined into a bundle. The bundles were stabilized continuously under tension, atmospheric pressure, and air atmosphere in a custom-made tubular furnace with three heating zones (380 mm in one heating zone length). A carefully designed three-step heating program was implemented during the stabilization process to gradually increase the temperature. In the first step (I), temperatures were set at 130-150-170 °C; in the second step (II), temperatures were raised to 190-210-230 °C; and finally, in the third step (III), temperatures reached 230-250-250 °C. The fiber collecting rate was about 380 mm/h. Subsequently, pyrolysis also took place continuously under tension, atmospheric pressure, and N₂ atmosphere at 1200 °C (Nabertherm RHTC 80-710/15, Germany). The gas flow rate was set to 250 ml/min. After pyrolysis, the fiber was cut into smaller pieces for the analytical measurements.

Scanning electron microscopy: The SEM images of the nanofibers were acquired with a Zeiss Sigma 300 VP (Gemini 2, Germany) scanning electron microscope equipped with a field emission cathode, a secondary electron (SE2), and an inlens detector. An acceleration voltage of 3 kV and a working distance of about 5 mm was used. Before the measurement small fiber samples were cut under liquid nitrogen. The pieces were attached to a sample

holder with conductive double-sided carbon tape. The samples were subsequently sputter-coated with an 8 nm gold layer by a Cressington 108 auto sputter coater.

Determination of the diameter for the tensile tests: The fibers were cut into pieces about 5 cm in length for the tensile test. On both sides of the fiber, 3-5 fiber pieces (with a length of approx. 2 mm) were cut for SEM specimens and a cross-section image was taken for each fiber as described before. The cross-sectional images were used to determine the surface area A with the software ImageJ. From the area, the diameter d was calculated using the formula for a circle diameter ($A = d^2 \pi/4$). Afterward, the mean value was calculated from the obtained 5-10 diameter values and used for the tensile tests.

Single fiber tensile strength: Tensile tests were performed using a tensile tester (zwickiLine Z0.5, BT1-FR0.5TN.D14, Zwick/Roell, Germany) with a clamping length of 10 mm, a crosshead rate of 5 mm/min at 25°C and a pre-tension of 0.001 N. The load cell was a Zwick/Roell KAF TC with a nominal load of 20 N. The single fibers were glued to a paper frame according to standard DIN1007 for single fibers tensile strength measurements (test length 25 mm). The fiber tensile tests were performed by a fiber test program and the input parameter was the average diameter which was determined by SEM for each fiber individually. After the tensile test measurement, quantitative analysis of the tensile strength and Young's modulus was carried out by Origin 2022 software.

Thermogravimetric analysis: Thermogravimetric measurements were performed by a simultaneous TGA/DSC device (STA449 F5 Jupiter system, Netzsch, Germany). Therefore 5-20 mg samples were measured in an Al₂O₃ crucible. The heating curve was set to 5 K min⁻¹ in air respectively nitrogen and the samples were heated to the required temperature.

Attenuated total reflectance fourier transform infrared spectroscopy: ATR FT-IR studies were performed on a Tensor 27 system (Bruker, Germany) equipped with an ATR unit with a diamond crystal. After a background measurement, the samples were ground to a fine powder with a mortar and pressed against the measuring diamond to receive a sufficient signal. The measurements took place in a wavenumber range of 4000-400 cm⁻¹ at a resolution of 5 cm⁻¹. The mean of 32 measurements per sample was calculated to obtain

higher signal-to-noise ratios. After the measurement, a baseline correction by the ATR FT-IR software (OPUS) was performed, and the measured data were saved as a .CSV file and plotted graphically using the Origin software.

Raman: A combined Raman-imaging / scanning force microscope system (WITTEC ALPHA 300 RA+, Germany) with WiTec Control FIVE 5.3 software was used for Raman measurements. The laser was equipped with a UHTS 300 spectrometer combined with a back-illuminated Andor Newton 970 EMCCD camera (Resolution: ca. 300 - 400 nm (lateral) and 900 nm (z) with 100x objective).

The measurements were carried out at an excitation wavelength of $\lambda = 532$ nm and a laser power of 1 mW with 50 accumulations with an integration time of 0.5 s pixel⁻¹. The samples were stacked on a glass slide. After adjusting the focus on the fibers at 100x magnification, the Raman spectrum was recorded. A cosmic ray removal and a baseline correction were performed on all spectra.

Nuclear magnetic resonance: NMR experiments were performed with a Bruker Avance II 300 (magnetic field 7.05 T) spectrometer in a 4 mm triple resonance sample head (also from Bruker) at a rotation speed of 10 kHz.

The ²⁹Si MAS NMR measurements were performed using a single-pulse quantitative experiment with a 90° pulse length of 3.5 μ s, a recycle delay of 60 s, and no proton decoupling during acquisition. The spectra were indirectly referenced with *N*(SiMe₃)₃ / σ (iso) = 2.4 ppm, with respect to tetramethylsilanes (TMS) (σ (iso) = 0.0 ppm).

Small angle X-ray scattering (SAXS): Scattering patterns were recorded with the SAXS system "Ganesha-Air" from (SAXSLAB, Xenocs). The X-ray source of this laboratory-based system was a D2-MetalJet (Excillum) with a liquid-metal anode operating at 70 kV and 3.57 mA with Ga-K α radiation ($\lambda = 0.1341$ nm) providing a very brilliant and a very small beam (<100 μ m). The beam was focused with a focal length of 55cm using a specially made X-ray optic (Xenocs) to provide a very small and intense beam at the sample position. The different fibers were placed in small bundles to give enough scattering volume in the vertical direction with respect to the X-ray beam. We used an EIGER2-4M (Dectris) at a distance of 16cm as the detector. The circularly averaged data were normalized to the incident beam, counts per

solid angle, and measurement time before subtraction of the background measurement (air). From these curves, the appropriate q range for the azimuthal plots was deduced for the azimuthal averaging ($15\text{-}20\text{ nm}^{-1}$). Also for the azimuthally averaged data air was used as the background. The azimuthal peaks from the graphite crystals were fit in Origin with a simple Gauss function to get the FWHM and calculate the order parameter as was done previously.⁴³ To get the crystallite sizes the peaks from the radially averaged data were fit also with a Gaussian and the Scherrer equation was used to receive an approximate crystal size and compare the different fibers in this aspect. The individual values from the fits can be found in **Table S2** and **Figure S1**.

Transmission electron microscopy (TEM): TEM measurements were performed by a JEM-2200FS TEM (JEOL Corporation, Japan) at an acceleration voltage of 200 kV. For the sample preparation, the fibers were ground into particles and dispersed in ethanol (99.8 %, Sigma-Aldrich Co.) in an ultrasonic bath. A small droplet of the suspension was put onto the copper grid and the sample was dried on a paper filter for one day.

Elemental analysis: Measurements were carried out at Mikroanalytisches Labor Pascher (www.mikrolabor.com, Germany). According to the company, the following methods were used:

Carbon in the polymer, oxidized, and ceramic state

The samples were burned with a combustion additive at about $1200\text{ }^{\circ}\text{C}$ in a stream of oxygen; the contained carbon burned to CO_2 . The CO_2 was dissolved in a sodium hydroxide solution and the carbon content in the sample was calculated from the change in electrical conductivity (conductometry).

Hydrogen in the polymer, oxidized, and ceramic state

The samples were burned at $1050\text{ }^{\circ}\text{C}$ in an oxygen stream. The combustion water formed was determined by IR spectroscopy.

Nitrogen in the polymer and oxidized state

The sample was melted at a temperature of $900\text{ }^{\circ}\text{C}$ in the oxygen stream with a catalyst. Ammonia, N_2 , or NO_x formed was passed over copper oxide and reduced to N_2 after switching the carrier gas to CO_2 , excess oxygen was bound. The nitrogen formed was purged into an

azotometer. Acidic reaction gases and the carrier gas CO₂ were bound by potassium hydroxide solution. The nitrogen gas was measured volumetrically.

Nitrogen in the ceramic state

The sample was degassed in a heated graphite crucible. The released nitrogen was measured with helium as the carrier gas with thermal conductivity detection.

Oxygen in the polymer and oxidized state

Samples were pyrolyzed at 1500°C in a glass carbon tube with carbon contact. Oxygen was detected as CO and measured by thermal conductivity detection.

Oxygen in the ceramic state

The sample was degassed in a hot graphite crucible. The CO/CO₂ produced by the reaction of the released oxygen with the graphite was pumped off and detected by IR spectroscopy.

Silicon in the polymer and oxidized state

After pressure digestion with nitric acid, the silicon dioxide formed was digested with sodium hydroxide solution under pressure. Detection was carried out by ICP-AES (Inductively Coupled Plasma-Atomic Emission Spectroscopy).

Silicon in the ceramic state

The sample was digested under melting (with a soda-borax mixture in a Pt crucible) and then dissolved with water. The silicon analysis was carried out by ICP-AES.

Burning experiments: For the burning experiments, 40 carbon and C/SiCON-40 fibers were combined into a bundle. The fibers were attached to a self-constructed metal frame using aluminum tape. On the opposite side, a piece of paper was applied using superglue and loaded with two magnets weighing 30 g in total. The fibers were then burned in the center using a gas flame and the time taken for the fibers to break was measured. A temperature sensor was used to ensure that the fibers were always in the 1200 °C range of the flame. The whole burning process was recorded on video.

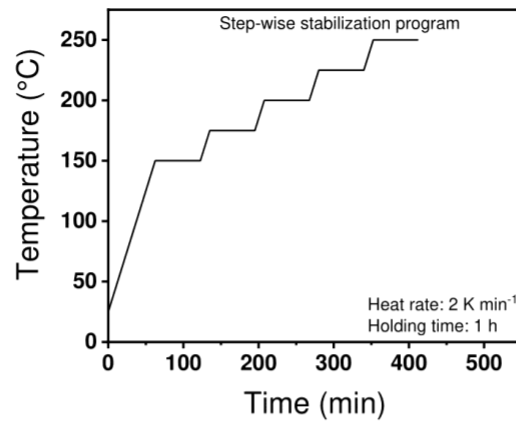


Figure S1. Step-wise stabilization program in air. With heating a heating rate of 2 K min⁻¹ and holding times of 1 h every 20 °C, starting at 130 °C.

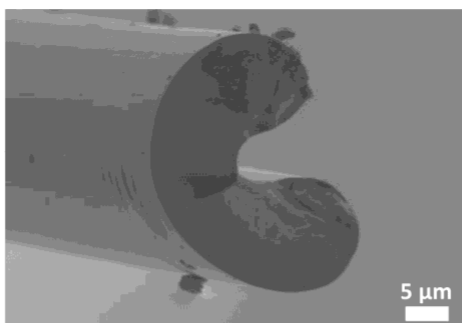


Figure S2. SEM image of the cross-section of C/SiCNO-40 fiber derived from the PAN/OSZ-40 precursor fiber produced in pure toluene.

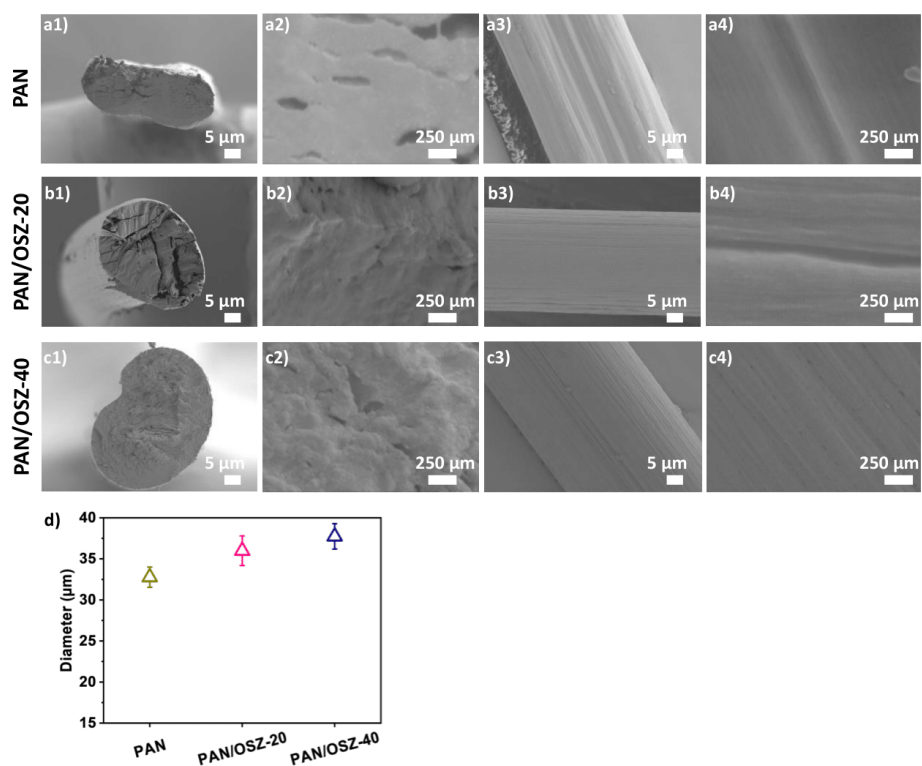


Figure S3. (a-c) SEM images in the cross-section and the longitudinal direction of PAN (a), PAN/OSZ-20 (b), and PAN/OSZ-40 (c) fibers. (d) Diameter of fibers with different amounts of OSZ.

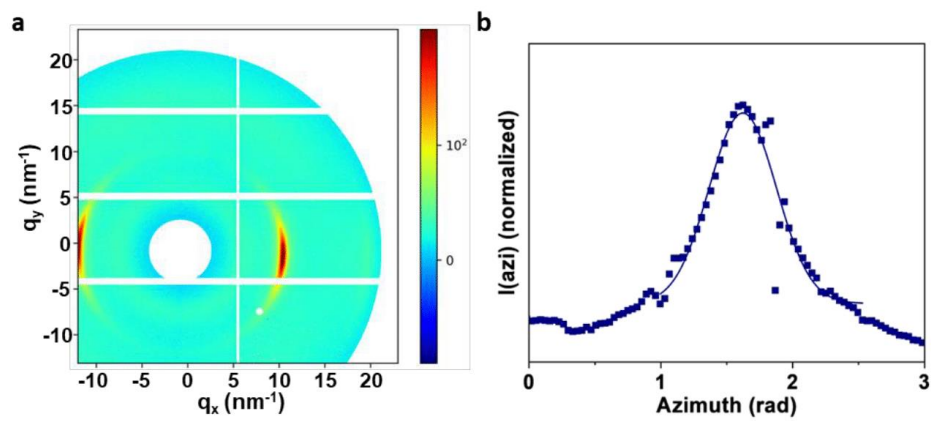


Figure S4. (a) 2D WAXS patterns of PAN/OSZ-40 composite fibers. (b) The azimuthal scan profiles of 2D WAXS patterns in panel (a).

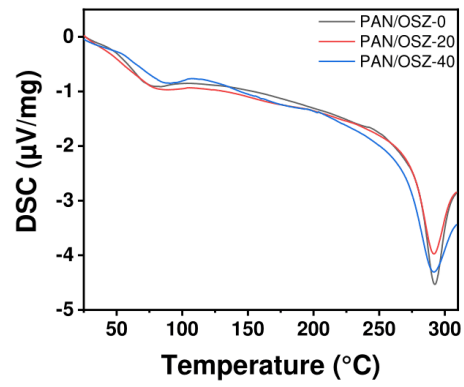


Figure S5. Differential scanning calorimetry of 0, 20, 40 wt.% PAN/OSZ fibers during the stabilization process (heating rate 5 K min⁻¹, atmosphere: air).

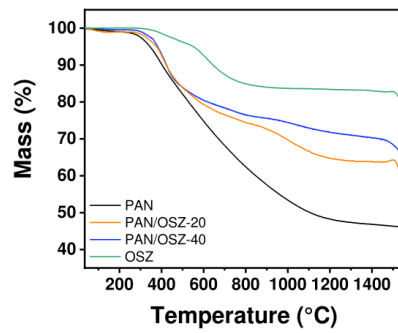


Figure S6. Thermogravimetric analysis of stabilized PAN fibers, PAN/OSZ fibers with different contents of OSZ, and pure OSZ (heating rate 5 K min^{-1} , atmosphere: N_2).

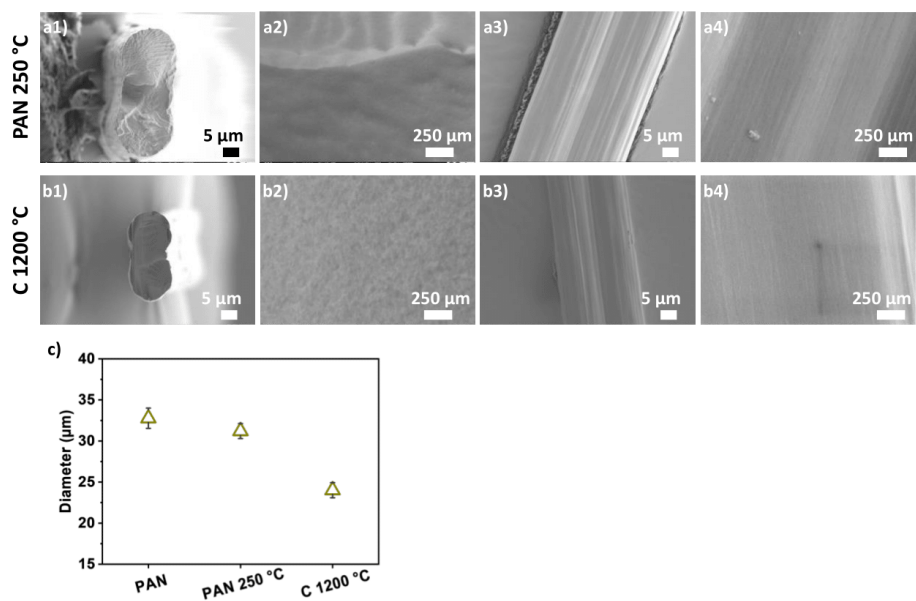


Figure S7. (a and b) SEM images in the cross-section and the longitudinal direction of stabilized PAN fibers at 250 °C (a) and the pyrolyzed carbon fibers at 1200 °C (b). (c) Diameter of fibers during polymer, stabilized, and pyrolyzed statuses.

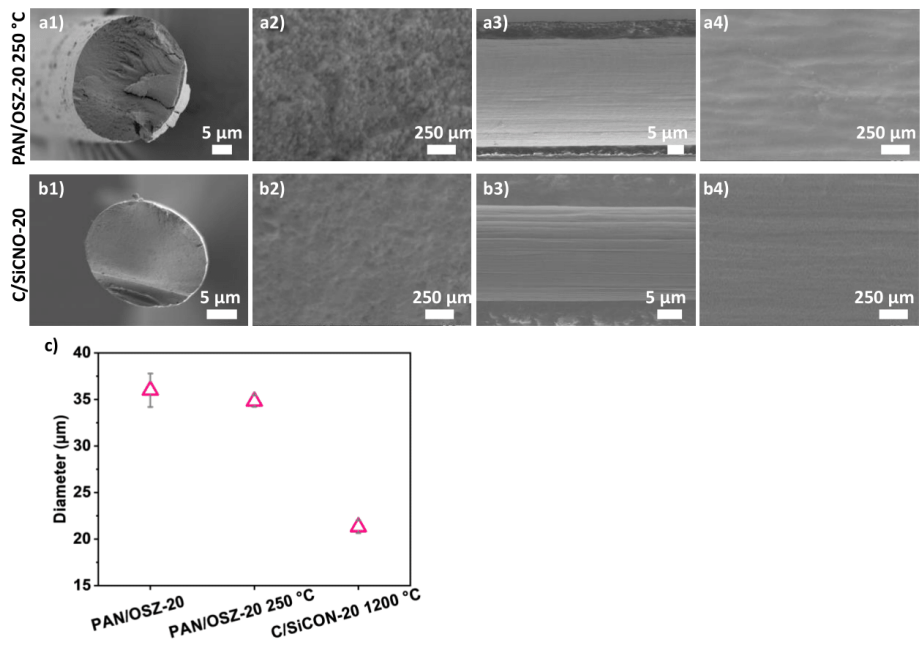


Figure S8. (a and b) SEM images in the cross-section and the longitudinal direction of stabilized PAN/OSZ-20 fibers at 250 °C (a) and the pyrolyzed C/SiCON-20 fibers at 1200 °C (b). (c) Diameter of fibers during polymer, stabilized, and pyrolyzed statuses.

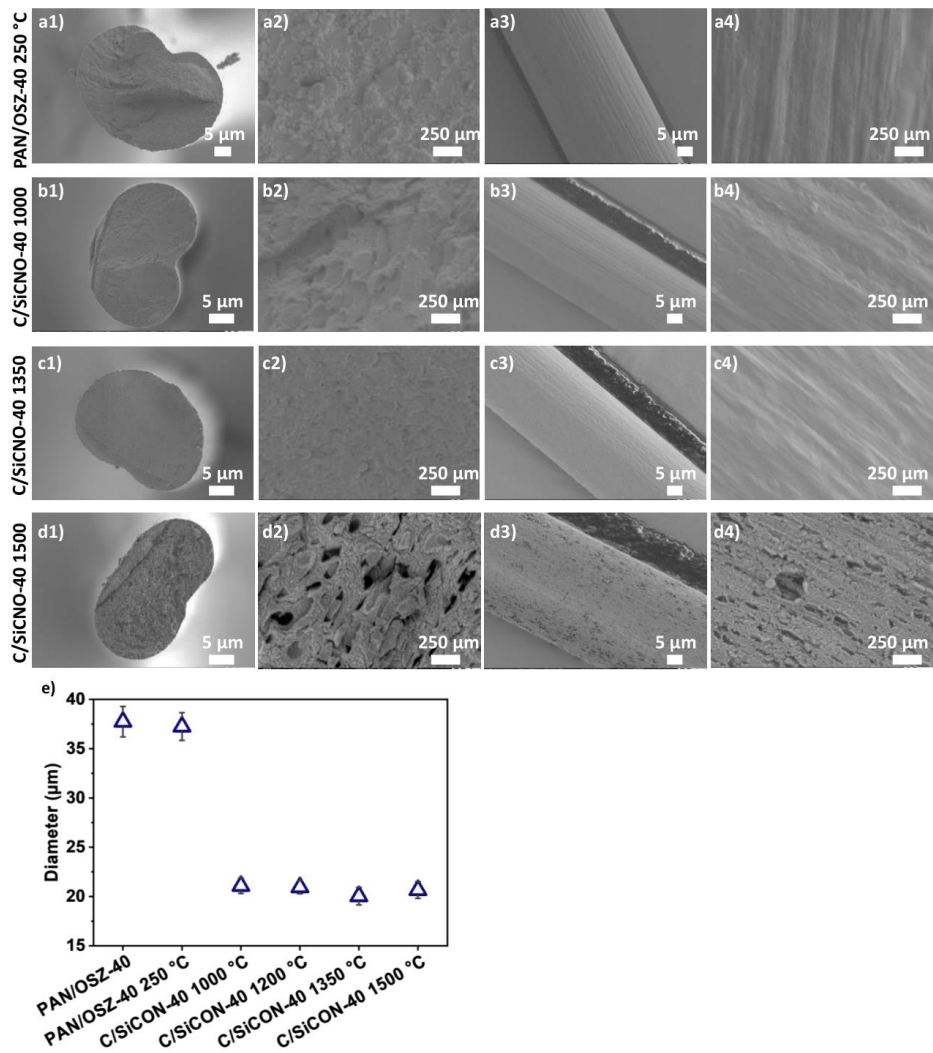


Figure S9. (a-d) SEM images in the cross-section and the longitudinal direction of stabilized PAN/OSZ-20 fibers at 250 °C (a) and the pyrolyzed C/SiCON-20 fibers at 1000 °C (b), 1350 °C (c), 1500 °C (d), respectively. (e) Diameter of fibers during polymer, stabilized, and pyrolyzed statuses.



Figure S10. Setup and attaching of fiber rovings with a length of 5-8 cm with mullite glue on carbon pieces inside quartz glass crucibles. Left: oxidize PAN/OSZ-40 fibers before pyrolysis; right: pyrolyzed C/SiCON-40 fibers.

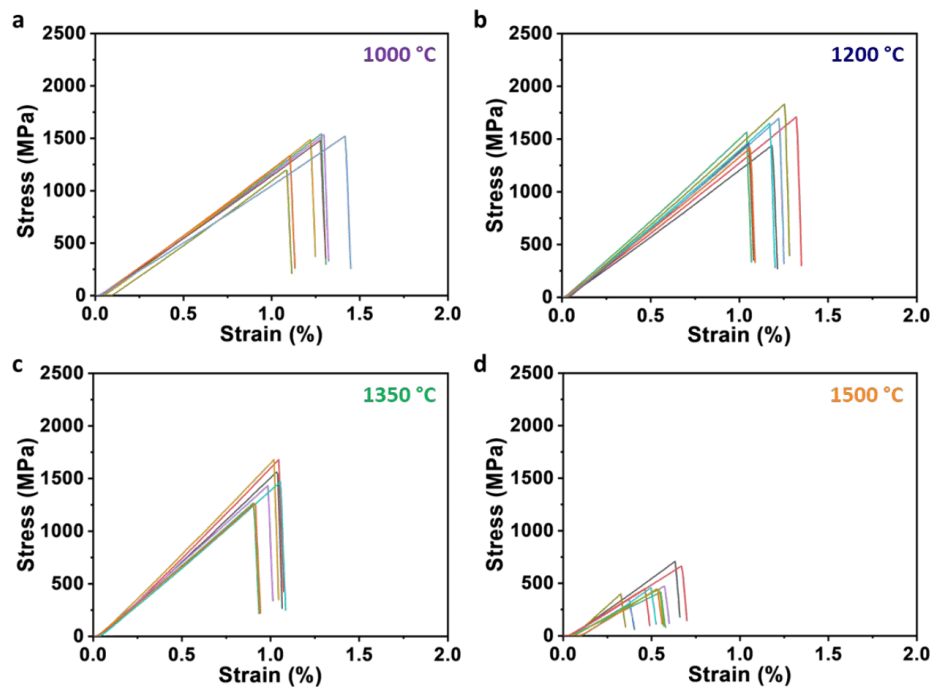


Figure S11. Stress-strain curves of noncontinuous C/SiCON-40 composite fibers pyrolyzed at different temperatures: (a) 1000 °C, (b) 1200 °C; (c) 1350 °C; (d) 1500 °C.

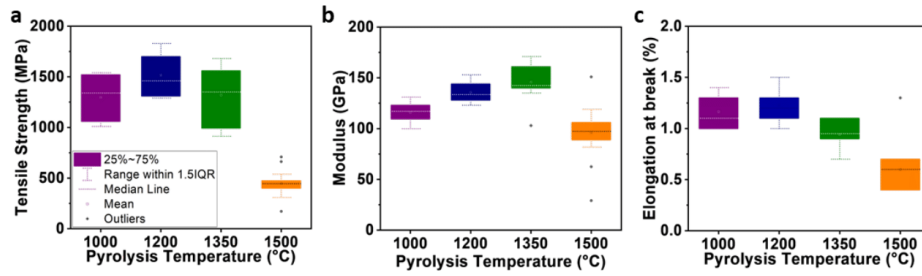


Figure S12. Comparisons of the mechanical properties of noncontinuous C/SiCON-40 composite fibers pyrolyzed at different pyrolysis temperatures: (a) tensile strength; (b) Young's modulus; (c) elongation at break.

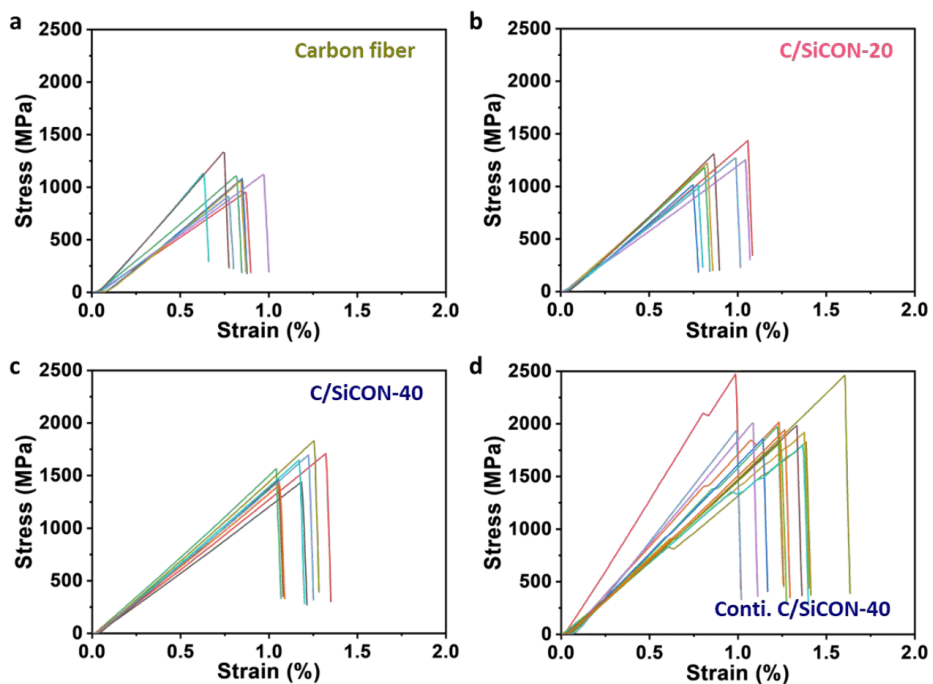


Figure S13. Stress-stain curves of fibers pyrolyzed at 1200 °C: (a) noncontinuous carbon fibers; (b) noncontinuous C/SiCON-20 fibers; (c) noncontinuous C/SiCON-40 fibers; (d) continuous C/SiCON-40 fibers.

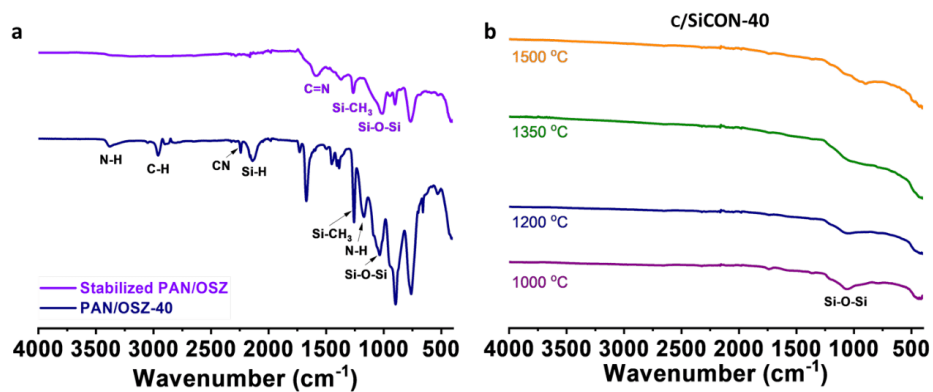


Figure S14. (a) ATR-FTIR spectra of the polymer (dark blue line), stabilized (purple line). (b) ATR-FTIR spectra of the carbonized/ceramide fibers from PAN with 40 wt.% OSZ.

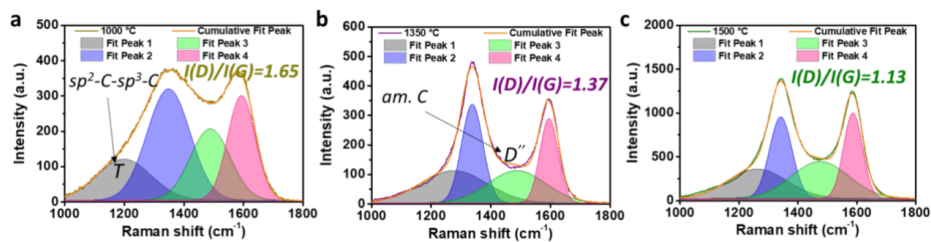


Figure S15. Curves fitted in Raman spectra of C/SiCON-40 composite fibers pyrolysis at different temperatures with a Gaussian function: (a) 1000 °C; (b) 1350 °C; (c) 1500 °C. The ratio of *I(D)* to *I(G)* exhibits a negative correlation with temperature, with decreasing values observed at higher temperatures.

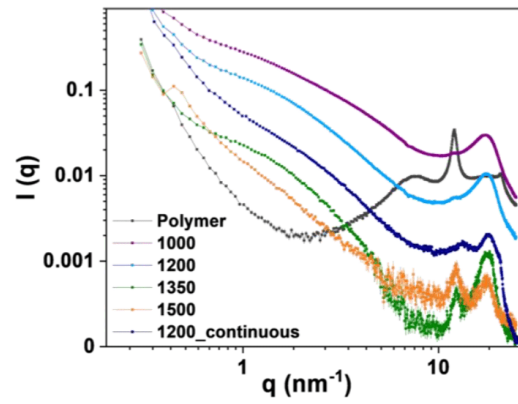


Figure S16. Small-angle X-ray scattering (SAXS) profiles of PAN/OSZ-40 precursor fiber, noncontinuous C/SiCON-40 fibers pyrolyzed at different temperatures, and continuous C/SiCON-40 fibers pyrolyzed at 1200 °C.

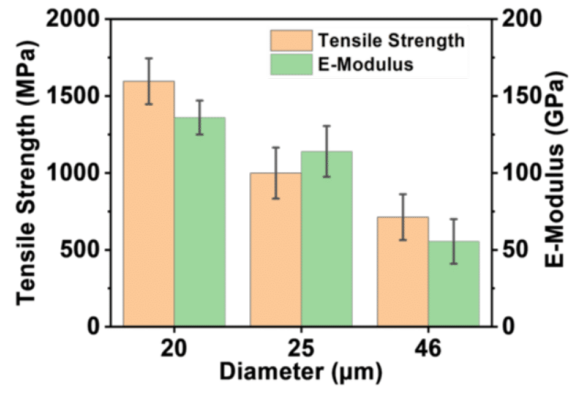


Figure S17. Changes in mechanical properties of C/SiCON-40 fiber with different diameters of fiber.

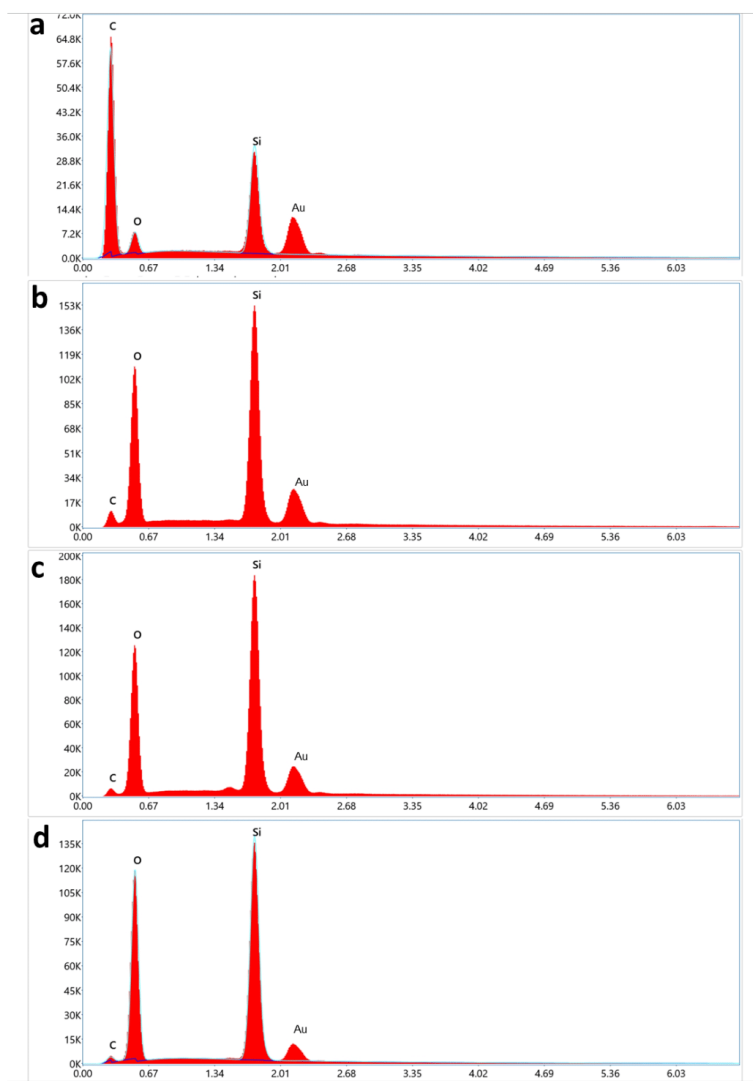


Figure S18. Changes in the elemental composition of C/SiCON-40 hybrid fibers in SEM-EDS analysis under thermomechanical loading at 1200 °C in air. (a) for 0 seconds (before treatment); (b) for 4 seconds; (c) for 30 seconds; (d) for 2 minutes.

Table S1: Compositions and parameters of wet spinning solutions of PAN/OSZ-0 to 40 fibers.
3 wt.% DCP was added to OSZ.

Content (wt.%)	PAN (g)	OSZ (g)	DMF (g)	DMF in bath (vol%)	SR
0	3	-	15.0	20	9
20	3	0.75	15.0	20	6
40	3	2.0	16,7	30	5

Table S2: Crystal orientation factor and crystallite size of the PAN/OSZ-40 precursor fiber, noncontinuous C/SiCON-40 fibers pyrolyzed at different temperatures, and continuous C/SiCON-40 fibers pyrolyzed at 1200 °C.

Sample	Crystal orientation factor	Crystalite size [nm]
PAN/OSZ-40 ^a	0.80	6.6
C/SiCON-40 1000	0.73	0.97
C/SiCON-40 1200	0.75	1.58
C/SiCON-40 1350	0.75	1.9
C/SiCON-40 1500	0.72	2.46
Cont. C/SiCON-40 1200	0.76	2.51

^a For PAN the peak at $q=12.1 \text{ nm}^{-1}$ was used

Table S3: Elemental composition calculated and measured for the polymer, stabilized state and measured after pyrolysis at 1200 °C (measurements done by Pascher www.mikrolabor.com).

Sample	Composition (at.%)					Empirical formula normalized on silicon
	C	H	O	N	Si	
Polymer	31.7	47.5	6.6	10.2	3.9	SiC _{9.06} H _{12.06} N _{2.59} O _{1.68}
Stabilized	31.9	43.6	11.0	9.1	4.5	SiC _{7.07} H _{0.23} N _{2.02} O _{2.43}
1200 °C	62.9	2.4	16.9	7.6	10.2	SiC _{6.14} H _{0.23} N _{0.75} O _{1.64}

Table S4: Comparisons of mechanical properties and diameter of our fibers with commercial fibers.

Fibers	Tensile Strength [GPa]	Young's modulus [MPa]	Diameter [μm]	Reference
C-fiber	1.1	140	20.0	This work
C/SiCON-20	1.2	140	21.3	This work
C/SiCON-40	1.5	136	20.9	This work
Conti-C/SiCON-40	2.0	175	20.0	This work
T300 (carbon)	3.5	230	7	2
T1100 (carbon)	7.0	320	5	2
M60J (carbon)	3.8	588	5	2
Nicalon 200N (SiC 1 st gen.)	3.0	210	14	3
Hi-Nicalon (SiC 2 nd gen.)	2.8	270	12	3
Sylramic (SiC 3 rd gen.)	3.2	~400	10	3

Notes and references

1. X. Liao, M. Dulle, J. M. de Souza e Silva, R. B. Wehrspohn, S. Agarwal, S. Förster, H. Hou, P. Smith and A. Greiner, *Science*, 2019, **366**, 1376-1379.
2. TORAYCA™ Technical Manual, Toray Composite Materials America, Inc., <https://www.toraycma.com/products/carbon-fiber/>.
3. O. Flores, R. K. Bordia, D. Nestler, W. Krenkel and G. Motz, *Adv. Eng. Mater.*, 2014, **16**, 621-636.

6 ACKNOWLEDGEMENTS

First of all, I would like to thank the entire Chair of Ceramic Materials at the University of Bayreuth, where I carried out this work.

In particular, I would like to thank Prof. Dr. Günter Motz for the excellent supervision, support, and guidance of my thesis.

I would also like to thank Prof. Dr. Stefan Schafföner for the opportunity to carry out my work at the chair and for the good cooperation.

Special thanks go to my former colleagues Jan-Felix Wendel, Dr.-Ing. Alexander Horcher, Jonas Kral, Mohamad Zahedtalaban, Dr. Awin Eranezhuth Wasan, Dr. Dmitrii Titov, Michael Knauer, Dr. Mateus Lenz Leite, Sven Scheler, Walter Müller, Bernd Martin and my former student Jan Tschernoster. All of them have supported me in my work and have always been there for me with help, advice, and most importantly fun.

Thanks also to my colleagues in Macromolecular Chemistry II at the University of Bayreuth, especially Dr. Xiaojian Liao, Prof. Dr. Andreas Greiner and Prof. Dr. Seema Agarwal, for their excellent cooperation and support.

Without the support of the chairs of Professors Breu, Breuning, Kempe, Retsch, Schmidt, and Senker this work would not have been possible. I would also like to thank the BCG Dean's Office for their organizational support.

I would like to thank the German Research Foundation (DFG) for their financial support of this project (455984818 (MO 851/21-1)), without it, this successful project would not have been possible.

Lastly, I thank my wife Susanne and my family for their unwavering support, words of encouragement, and patience during frustrating phases.

7 (EIDESSTATTLICHE) VERSICHERUNGEN UND ERKLÄRUNGEN

(§ 9 Satz 2 Nr. 3 PromO BayNAT)

Hiermit versichere ich eidesstattlich, dass ich die Arbeit selbständig verfasst und keine anderen als die von mir angegebenen Quellen und Hilfsmittel benutzt habe (vgl. Art. 97 Abs. 1 Satz 8 BayHIG).

(§ 9 Satz 2 Nr. 3 PromO BayNAT)

Hiermit erkläre ich, dass ich die Dissertation nicht bereits zur Erlangung eines akademischen Grades eingereicht habe und dass ich nicht bereits diese oder eine gleichartige Doktorprüfung endgültig nicht bestanden habe.

(§ 9 Satz 2 Nr. 4 PromO BayNAT)

Hiermit erkläre ich, dass ich Hilfe von gewerblichen Promotionsberatern bzw. –vermittlern oder ähnlichen Dienstleistern weder bisher in Anspruch genommen habe noch künftig in Anspruch nehmen werde.

(§ 9 Satz 2 Nr. 7 PromO BayNAT)

Hiermit erkläre ich mein Einverständnis, dass die elektronische Fassung der Dissertation unter Wahrung meiner Urheberrechte und des Datenschutzes einer gesonderten Überprüfung unterzogen werden kann.

(§ 9 Satz 2 Nr. 8 PromO BayNAT)

Hiermit erkläre ich mein Einverständnis, dass bei Verdacht wissenschaftlichen Fehlverhaltens Ermittlungen durch universitätsinterne Organe der wissenschaftlichen Selbstkontrolle stattfinden können.

Ort, Datum, Unterschrift